Simulation of Degradation and Failure of Suspension Bridge Main Cables due to Natural and Anthropogenic Hazards

FINAL REPORT
October 2022

Submitted by:

Adrian Brügger, Ph.D.
Associate Research Scientist

Raimondo Betti, Ph.D.
Professor

Columbia University
500 West 120th St., MC4709
New York, NY 10027

External Project Manager
Dyab Khazem, Sr. Project Manager
Parsons Transportation Group
100 Broadway Avenue
New York/NY/10002

In cooperation with

Rutgers, The State University of New Jersey
And
U.S. Department of Transportation
Federal Highway Administration

Disclaimer Statement

The contents of this report reflect the views of the authors, who are responsible for the facts and the accuracy of the information presented herein. This document is disseminated under the sponsorship of the Department of Transportation, University Transportation Centers Program, in the interest of information exchange. The U.S. Government assumes no liability for the contents or use thereof.

The Center for Advanced Infrastructure and Transportation (CAIT) is a Regional UTC Consortium led by Rutgers, The State University. Members of the consortium are Atlantic Cape Community College, Columbia University, Cornell University, New Jersey Institute of Technology, Polytechnic University of Puerto Rico, Princeton University, Rowan University, SUNY - Farmingdale State College, and SUNY - University at Buffalo. The Center is funded by the U.S. Department of Transportation.

TECHNICAL REPORT STANDARD TITLE PAGE

1. Report No.	2. Government Accession No.	3. Recipient's Catalog No.
CAIT-UTC-REG22		

4. Title and Subtitle	5. Report Date
Simulation of Degradation and Failure of Suspension Bridge Main Cables due to Natural and Anthropogenic Hazards	October, 2022
	6. Performing Organization Code CAIT/Columbia University

7. Author(s)	8. Performing Organization Report No.
Adrian Brügger http://orcid.org/0000-0001-9164-0385 Raimondo Betti https://orcid.org/0000-0002-6119-190X	CAIT-UTC-REG22

9. Performing Organization Name and Address	10. Work Unit No.
Columbia University 500 West 120th St., MC4709 New York, NY 10027	11. Contract or Grant No. 69A3551847102

12. Sponsoring Agency Name and Address	13. Type of Report and Period Covered
Center for Advanced Infrastructure and Transportation Rutgers, The State University of New Jersey 100 Brett Road Piscataway, NJ 08854	Final Report Sept. 1, 2019 – August 31, 2022
	14. Sponsoring Agency Code

15. Supplementary Notes
U.S. Department of Transportation/OST-R
1200 New Jersey Avenue, SE
Washington, DC 20590-0001

16. Abstract
This project focused on the creation of a numerical model able to emulate the static and dynamic behavior of the mechanical components (wires embedded in the cable) which are subjected to high temperature fields. Fire incidents on suspension bridges have become an increasing risk to safety. The vehicles that catch fire contain flammables having potential to affect a suspension bridge's structural members. In many cases, these are hydrocarbon fires, which are known to burn at higher temperatures. Case studies have shown fires do occur mid-span or near the anchorage. The duration of these fires easily reaches an hour, which can lead to damage in the main cables. When not in close proximity to the main cables, fires can present danger to the suspenders, deck, and other structural components that will require repair or accelerated maintenance. Moreover, the economic impacts of suspension bridge fires must be considered. Not only is productivity of the community hindered, but also the toll revenue loss creates concern for bridge owners.

17. Key Words	18. Distribution Statement
suspension bridge, cable, fire, safety, hazard, finite element analysis, neutron diffraction, friction, load transfer, safety factor	

19. Security Classification (of this report)	20. Security Classification (of this page)	21. No. of Pages	22. Price
Unclassified	Unclassified	Total #110	

FINAL REPORT

Simulation of Degradation and Failure of Suspension Bridge Main Cables due to Natural and Anthropogenic Hazards

Adrian Brügger, Raimondo Betti, et al.

EXECUTIVE SUMMARY

Work has been completed on the main thrust of the project, namely the identification of the internal mechanics of suspension bridge cable strands through Genetic Algorithms (GA) using a computational mechanics model with surrogate contact elements. Currently, the GA algorithm has been fully developed and debugged. Its implementation on the full model is has been completed with the experimental data gathered previously using neutron diffraction. The GA has successfully identified a set of stiffness parameters between the wires of a bridge cable bundle that provides an optimal solution for the contact mechanics between all wires in the bundle. This is the first such solution for a multibody system of this complexity.

Additional work has been conducted on various fronts by a group of summer research students, specifically the modeling of friction and interactions of bridge wires to wire fracture. The work in this area will inform the collapse models that are currently in draft for publication in peer-reviewed journals. This is the first work of its kind that includes direct internal force measurements inside a bridge cable, to the knowledge of the authors.

The cooling behavior of a bridge cable subsequent to a fire incident has also been simulated in three dimensions. Thermodynamic cooling rates were investigated using finite element simulations to understand the potential of damage caused by long annealing times caused by the slow cooling behavior of the cable cross section; both active water cooling and air cooling are considered. The abovementioned results are provided here and relevant recommendations made to the engineering community and first responders.

Table of Contents

CHAPTER I: ESTIMATION OF STRUCTURAL PARAMETERS OF A BRIDGE CABLE THROUGH GENETIC ALGORITHM

Adrian Brügger, Marcello Morgantini, Raimondo Betti

Problem Statement

The current research efforts are focused on the creation of a numerical model able to emulate the static and dynamic behavior of the mechanical components (wires embedded in the cable) which are subjected to high temperature fields. Usually, numerical models are developed under the assumption that they are given an acceptable estimation of the material and geometrical properties of a real physical system. For complex geometries, this assumption does not always hold true, leading to potentially unrealistic hypotheses (geometry perfectly defined, homogeneous materials, etc.) produced by the numerical model. As those hypotheses become weak, the mismatch between the model and the real system leads to bias in the results of simulations. This research aims to improve and optimize the approximation of the real system provided by the numerical model. The main idea is to set up a Genetic Algorithm (GA) in order to evaluate the most likely values of the parameters defining the numerical model so that the mismatch with the real system is minimized. The numerical model has been implemented in Abaqus, a software relying on the Finite Element Method (FEM). The model is defined by a section of a main cable strand consisting of 61 wires. These wires are constrained by two clamps introducing a certain stress level (configuration) in the wires that are also subjected to a temperature field. Abaqus is chosen here to accommodate the relative geometric complexity of the model in addition to non-stationary stress and thermal fields.

Despite these challenges, Abaqus is able to provide reliable and detailed results. A Genetic Algorithm represents an iterative optimization method that relies on the pre-post processing of data, which, in this context, is generated by Abaqus. The work at the base of this study relies on the combination of two software packages: Matlab and Abaqus. Whereas Abaqus allows us to perform numerical simulations, Matlab is used to perform the optimization algorithm (GA) extracting the simulation results provided by Abaqus and using them to define the parameters to feed Abaqus for the next numerical simulation.

A physical specimen consisting of 61 wires (Figure 1) has been analyzed experimentally as it is subjected to a stress field generated by a compaction clamp. The resulting stress inside of the strand has been measured using both conventional strain gauges and state-of-the-art neuron diffraction

techniques [1]. The stress in a specific wire depends on the forces generated by the contact between the wires or between the clamps with the wire itself. The wire-to-wire contact is a function of the system geometry and material properties and can be modeled through spring elements connecting the cables with a certain stiffness. Those springs (connectors shown in Figure 2) are set through a GA that minimizes the mismatch (error) between the experimental stress data in the physical specimen and the stress estimated through the numerical model (Abaqus).

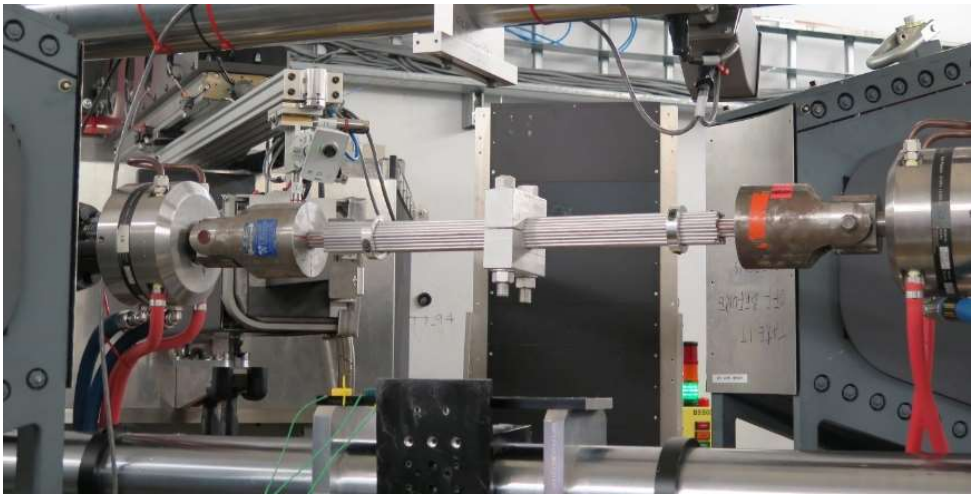

Figure 1: 61-wire strand with Al clamp attached to the midpoint of the strand loaded in the VULCAN diffractometer. Neuron strains are scanned in the cross section under the clamp [1].

The methodology for the estimation of the von Mises stress inside of the wires is exhaustively discussed in [1].

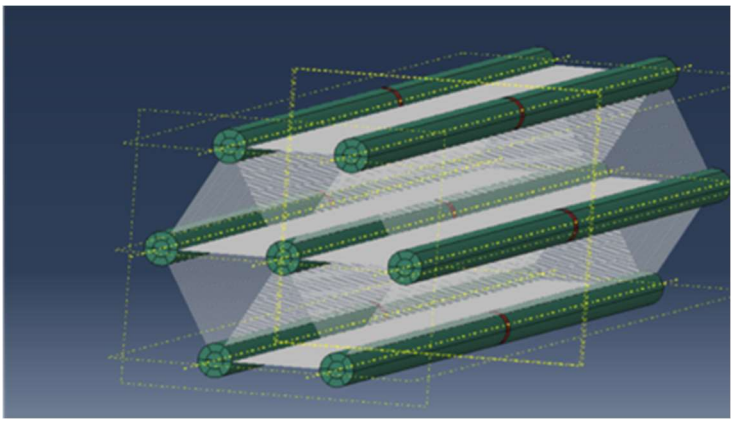

Figure 2: 3D illustration of the spring elements (connectors) for seven adjacent wires that are part of the 61-wire strand.

The flowchart of the entire procedure is illustrated in 3. The FEM model is developed in Abaqus to provide an estimate of the von Mises stress inside of the cable. The FEM model can be converted

into a script and, through the software Abaqus2matlab, into an input file (.inp). This input file can be used in Matlab to run Abaqus simulations and extract the structural information about the model (information at each node of the FEM model). Structural information such as nodal coordinates and von Mises stresses are extracted and compared with those coming from the experimental data. The von Mises stress configuration obtained from the Abaqus model is given as a function of the stiffness values of the spring elements (connectors). The objective of the Genetic Algorithm is to tune the stiffness values of these spring elements, thereby converging to a solution that minimizes the mismatch between the von Mises stresses of the Abaqus model and those experimentally obtained. For this purpose, the original input file, obtained by Abaqus2matlab, is modified by tuning the stiffness of the spring elements (connectors). The mean square error (MSE) between the numerical and the experimental von Mises stresses is computed until convergence to an optimal solution is achieved. In order to statistically validate the solution (estimation of the stiffness of the spring elements), additional runs of the algorithm are advisable.

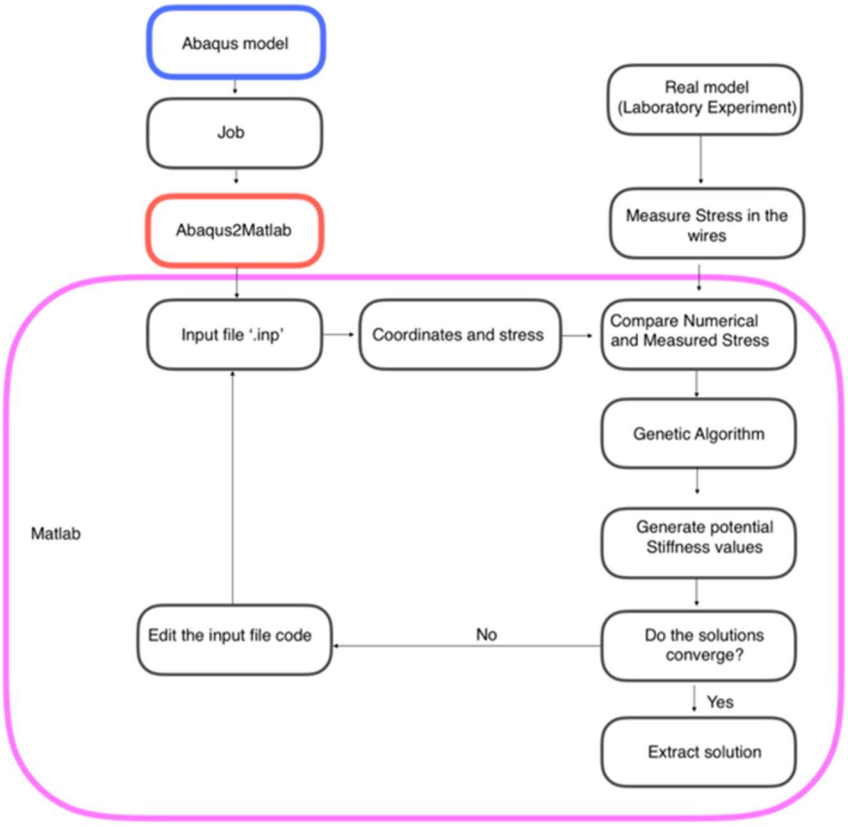

Figure 3: Flow-chart of the parameter optimization procedure.

ABAQUS Model

The Abaqus model consists of 61 wires that are subjected to compression through the application of an external load on a two-part clamp. The case analyzed in this paper is the one referred to as 'High Clamping' in Table 1. For such a case, the force applied by the screws on the clamps is converted into an equivalent stress and used as a boundary condition of the Abaqus model.

Table 1: Clamping load cases used in the neutron diffraction experiment.

Load Case Name	***Bolt Torque (Nm)***	***Measured Bolt Stress (MPa)***	***Bulk Bolt Tension (kN)***
Unclamped	0	0 (*d_0 case*)	0
Low Clamping	50	79±3	31.2±1.2
High Clamping	100	180±6	71.2±2.4

The 61 wires interact with each other and with the clamp through elements defined by Abaqus as 'connectors'. The stiffness of the spring elements is initialized according to the theoretical value, i.e. 6.35×10^9 N/m. The von Mises stress configuration for this particular case is provided in Figure 4. As shown, the von Mises stresses inside the wires are in the range of 2.02 to 285.00 MPa.

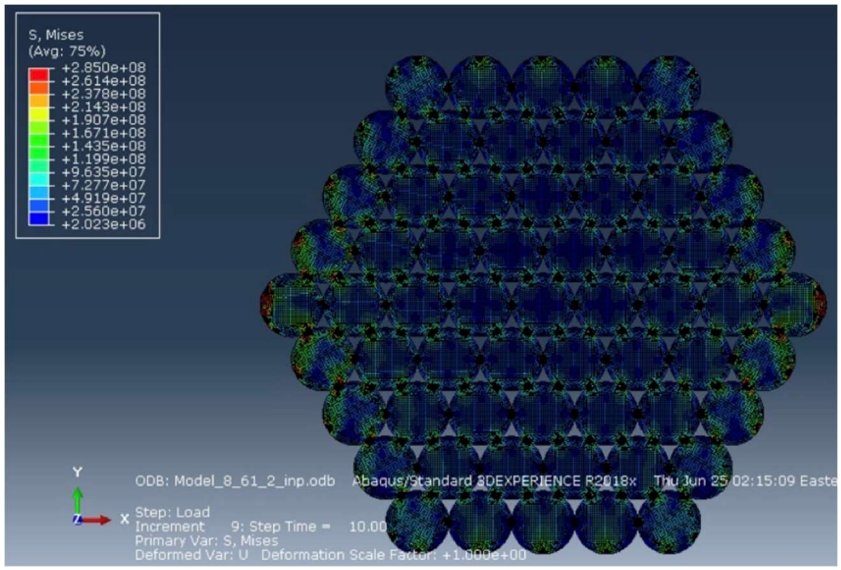

Figure 4: Abaqus FEM model: von Mises stress configuration.

The von Mises stress configuration of the wires shown in Figure 4 can be obtained and analyzed in Matlab as shown in Figure 5. In Figure 5 it is also possible to visualize the von Mises stress configuration inside of the clamps. Considering Figure 4 and Figure 5, it is clear that the gradient of the von Mises stress inside each of the wires is significant. Furthermore, for each of the wires' sections,

an average von Mises stress can be computed and compared with the results obtained in the same gauge volume as the neutron diffraction experiment.

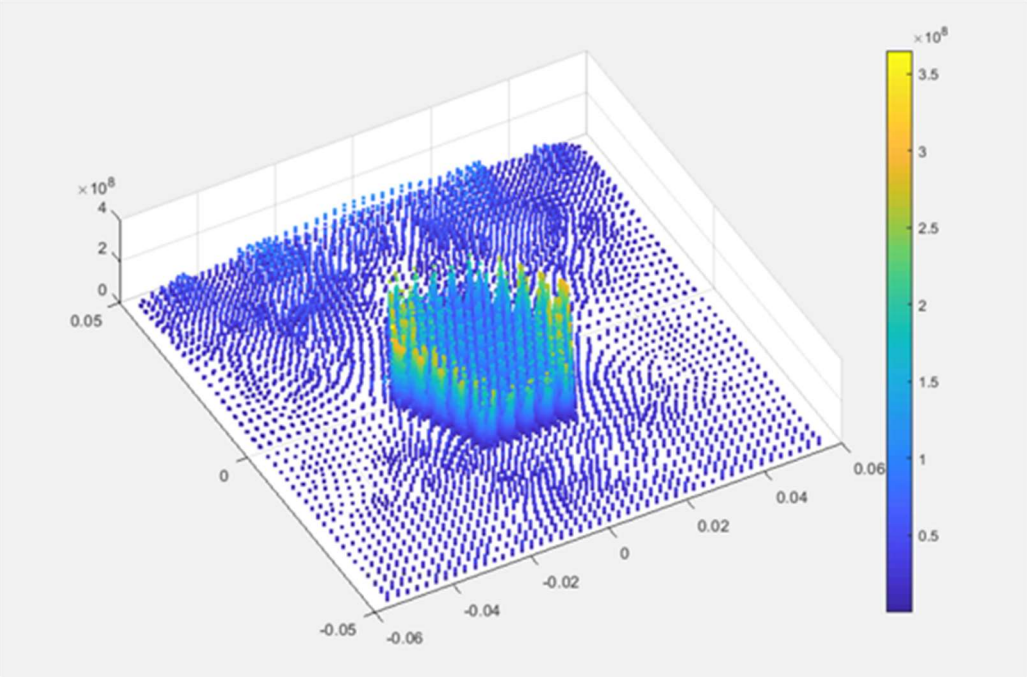

Figure 5: Nodal von Mises stress configuration, Matlab plot.

In Figure 6, the methodology proposed for the computation of the average von Mises stress for each wire is shown. For each wire, the nodes inside of a square of dimensions 2x2 mm^2 concentric with the wire itself are considered and the average of their von Mises stress is computed. Figure 6 shows the transversal section of the 61 wires, and the 61 2x2 mm^2 squares (orange).

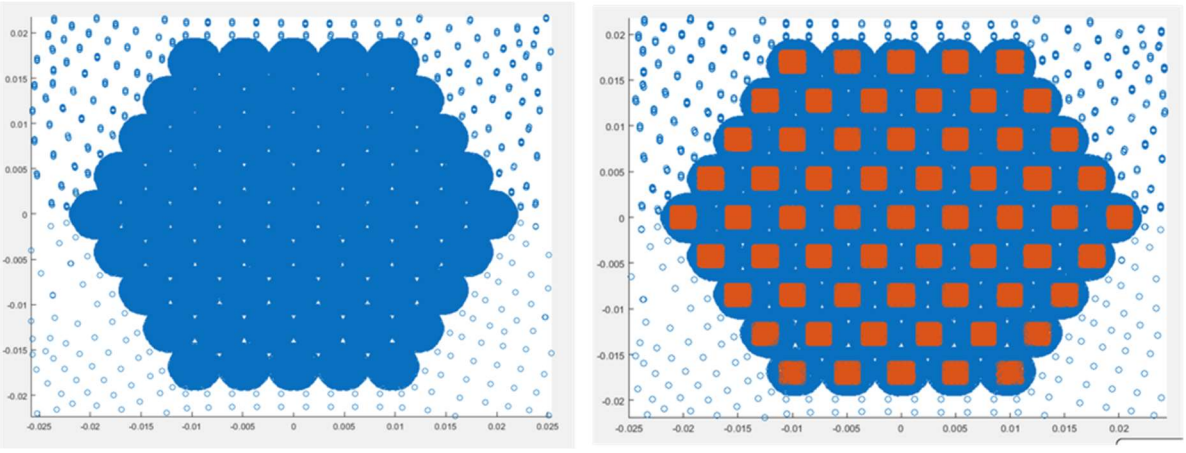

Figure 6: Nodal Von Mises stress configuration and 2x2 mm squares.

Physical System

The experiments have been performed at both the Los Alamos National Laboratory's (LANL) LANSCE SMARTS as well as Oak Ridge National Laboratory's (ORNL) SNS VULCAN engineering materials diffractometers [1]. The von Mises stress configuration of the relevant experiment is shown in Figure 7.

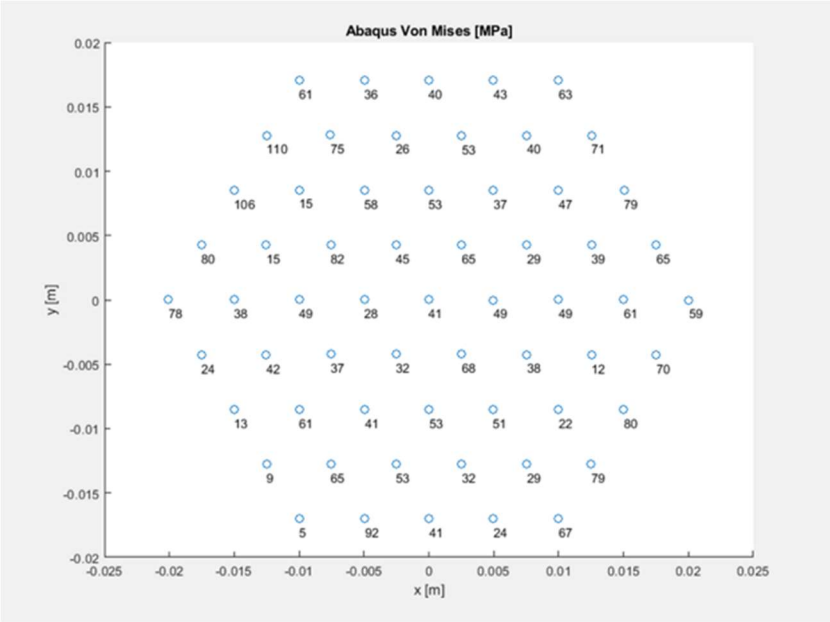

Figure 7: von Mises stresses measured in the centric 2mm*2mm gauge volume of each wire using neutron diffraction.

Genetic Algorithm

Genetic Algorithms are a fundamental part of the Matlab toolbox, capable of handling complex mathematical functions. For this study, the mathematical function to be analyzed is represented by a relatively complicated FEM model, requiring the integration of a third party software package into the optimization algorithm. For this reason, the GA has been fully re-designed. The implemented recursive GA relies on:

1. Ranking
2. Selection
3. Crossover
4. Mutation

The first validation of the GA has been obtained by employing it to estimate the stiffness values of the spring elements within the 61 wire bridge cable model. This is done by purposefully setting a

unique value for the stiffness of the spring elements themselves. The effectiveness of the newly designed GA has been validated by considering a reference model whose connectors' stiffness value has been set at 6.35×10^9 N/m. The objective of the GA is to identify the correct value of such a reference model. The first step of the GA consists in the generation of some models whose parameters are iteratively modified to converge to the correct solution. Figure 8 shows how the GA identifies the correct value of the connector stiffness after 30 iterations. Figure 8 (a) shows the initialization of the stiffness value of 10 different models and the best fit. In order to provide a good 2D visual representation, the two dimensions of the plots represent the same quantity. Figure 8 (b) shows the 10 potential solutions (overlapping points) after 30 iterations and the solution providing the best fit of the reference model.

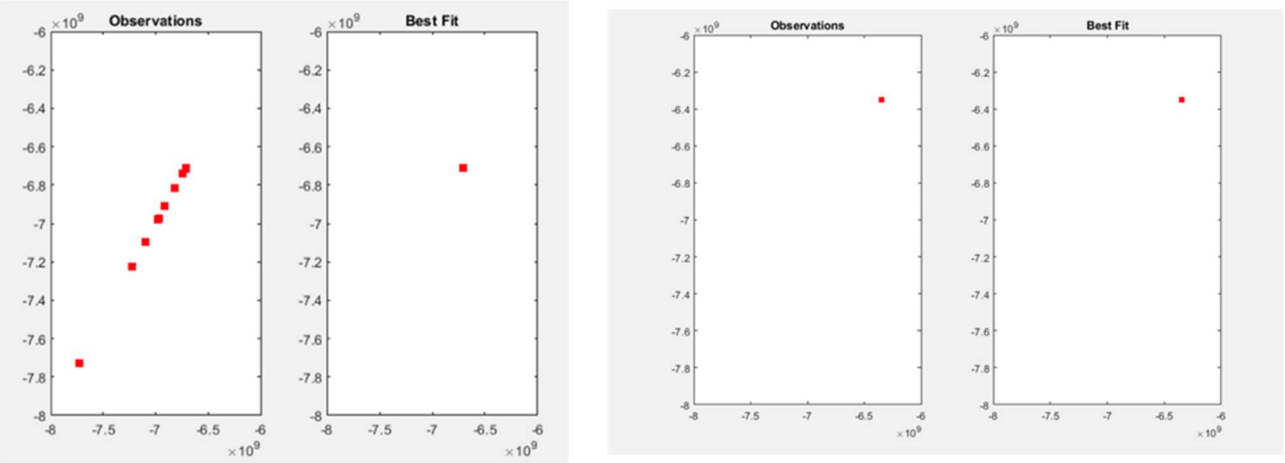

(a) (b)

Figure 8: GA validation test, showing (a) initial sample population and (b) convergence to the correct solution after 30 iterations.

Results

In order to reduce and optimize the computational effort required to run the genetic algorithm, investigations about a single iteration of the GA have been conducted. The computational time required for one iteration of the method (consisting of 156 models) is 4.44 hours on a Pentium-core standalone calculation workstation. For this validation, the stiffness value of the connectors has been initialized in the range 6×10^9 N/m to 8×10^9N/m. Obviously, this range is unable to lead to a correct stiffness configuration since the spring elements connecting wires that are not in contact with each other have theoretical stiffnesses equal to 0 N/m. In any case, this stiffness range represents a reasonable choice to test the GA functionality while maintaining a tight boundary on the optimization

domain. The Mean Squared Error (MSE) is used to identify the model providing the best fit of the von Mises stress experimentally obtained in [1] and shown in Figure 7.

As mentioned, 156 models are tested in the first iteration of the GA. In order to identify the models fitting the real model better, the MSE has been computed and reported in Figure 9. The MSEs of the 156 models are very similar to each other, and the connectors have very similar stiffnesses.

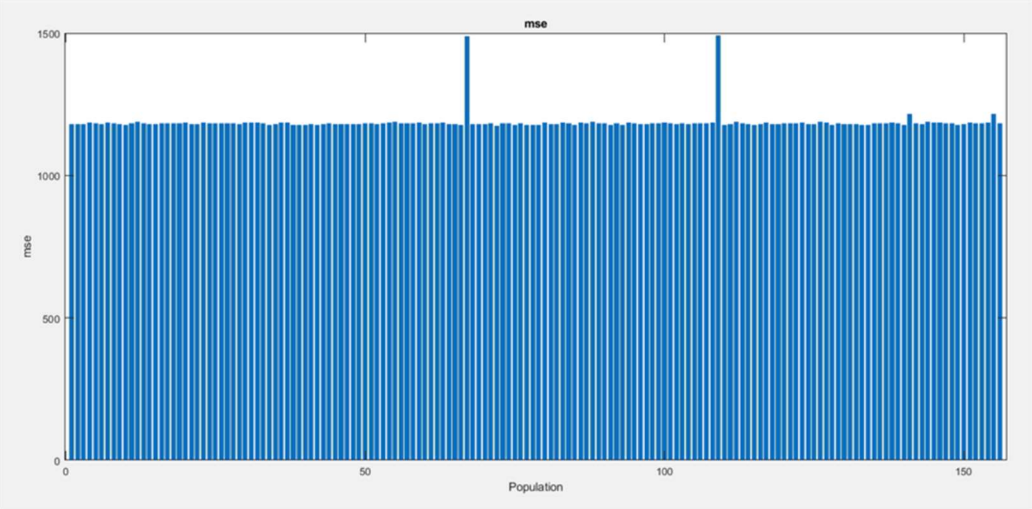

Figure 9: MSE for each of the 156 models.

The stress configuration related to two of the 156 models randomly picked is shown in Figure 10. The solutions provided by these models are also very similar to each other.

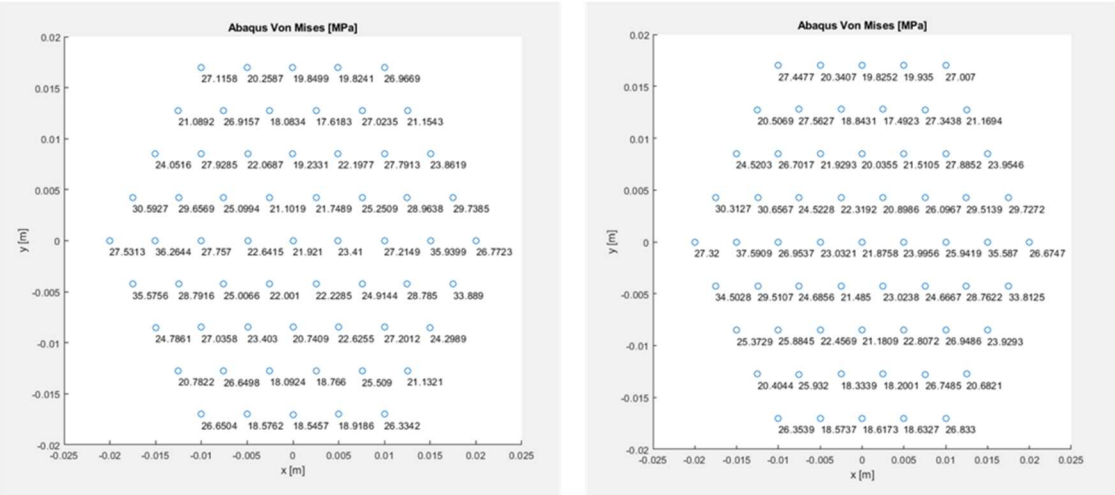

Figure 10: Comparison of the von Mises stress configuration related to two models chosen at random.

Future Work

Until today the following objectives have been achieved:

1. Design and development of a 2D FEM Abaqus model to generate data about the Von Mises stress configuration
2. Modification and usage of the Abaqus2matlab software for the extraction and manipulation of data in the Matlab environment
3. Creation of the Matlab codes (main, scripts and functions) of a GA algorithm, development of codes for the manipulation of .inp and .txt files
4. Test and configuration of the final GA code.

The results provided through the application of the GA need to be statistically validated. In order to do so, a larger number of workstations will be used to run the algorithm simultaneously and provide multiple solutions for comparison and validation. The next steps consist of:

1. Run the GA on more workstations simultaneously
2. Extract, analyze and comment the final results.

As mentioned, one iteration of the developed GA takes 4.44 hours on a standalone workstation. According to recent publications, it is best practice to use 10 times as many models as the number of variables to be estimated [3-4]. Thus, each iteration of the GA will take 44.4 hours and, for a total of 30 iterations, more than 50 days. For this reason, we are currently investigating various avenues to increase the workstation pool to scale the calculations accordingly. As of now, we can count on 8 Abaqus licenses and so only 8 Abaqus simulations can be performed at once.

Ultimately, this simulation will allow us to generate a surrogate finite element model that is independent of the traditional contact model domain, known to be both numerically expensive and prone to divergence. The model will allow both researchers and practitioners to model the contact mechanics inside bridge cables as a function of confinement force. This will allow us to perform more accurate collapse modeling of a bridge cable undergoing deleterious external forcing caused by overload, corrosion, and fire.

References

[1] Brügger A, Lee SY, Robinson J, Betti R, Noyan IC (2020) Internal Contact Mechanics of 61-Wire Cable Strands.

[2] Papazafeiropoulos R, Muniz-Calvente M, Martinez-Paneda E (2017) Abaqus2matlab: a suitable

tool for Advances in Engineering Software.

[3] Haupt RL (2000) Optimum population size and mutation rate for a simple real genetic algorithm that optimizes array factors.

[4] Rylander SGB, Gotshall B (2002) Optimal population size and the genetic algorithm.

CHAPTER II: CABLE CONTACT FINITE ELEMENT MODELING

Kuangguidong Wang

Abstract

Based on the configuration of the previous 7-wire model, new connector behaviors, such as friction, failure and nonlinear elasticity are added into the model. Those connector behaviors are tuned based on the analytical solution of wire interaction and the pull out experiment. Later, a pullout test modeling is conducted, and the result is compared with the experimental data.

Introduction

The main cable of a suspension bridge is comprised of thousands of wires which are subjected to friction contact and mechanical interference due to the compaction provided by the cable band and wrapping wires. Modeling those interactions between the wires within the bridge cable can usually cause convergence problems using traditional finite element methods [1]. FEM software package Abaqus allows users to set up connectors which can substitute modelling full contact. This method alleviates the convergence issue and therefore is adapted in this model. Previous model has the elementary setup which includes the geometry, constraints, load and connectors that establish the contact behavior of each element [2]. Those connectors are the Cartesian type whose behaviors in three orthogonal directions: U1, U2 and U3 can be set up independently (Figure 11). But all the connector behaviors in the previous model are set to be elastic and the coefficients are undetermined. This time, new connector behaviors are added into the model and their coefficients are tuned based on the analytical solution as well as the experimental data so that the modeling result would be closer to reality. The behaviors of all three components of the connector, are refined using friction, failure and nonlinear elasticity definition in Abaqus. Meanwhile, convergence behavior and computing efficiency are also addressed in this model. The method of determining those connectors behaviors will be discussed in detail in following sections.

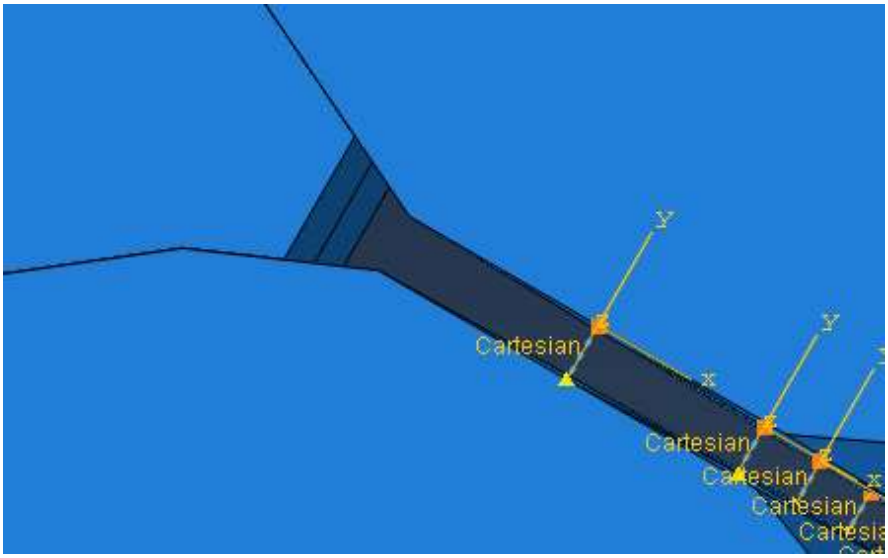

Figure 11: The connectors placed between the interaction surfaces of the wires and their local coordinates. The x, y, z axis of the local coordinates is referred as U1, U2, and U3 directions in this report.

ABAQUS Model

Connector behavior in U2 direction

In this model, the contact forces within the cross section when clamping is applied are controlled by the connector behavior in U2 direction. A nonlinear elasticity behavior is adapted in this direction to model the Hertzian contact between two wires and the parameters for this nonlinear elasticity behavior is obtained from the analytical solution [3]. The equation for this contact force is given by the following equation:

$$\delta_n = \frac{c^2 P}{2E}\left[\frac{2}{3} + 2ln\left(\frac{2r}{b}\right)\right]$$

where $P = \frac{2}{\sqrt{3}}\left(\frac{d}{D}\right)T$, $b = c\sqrt{\frac{Pr}{E}}$ and $c^2 = \frac{4(1-v^2)}{\pi}$. T is referring to tension per unit axial length in the wrapping in the original literature. Here the clamping force per unit contact length is used to approximate the result.

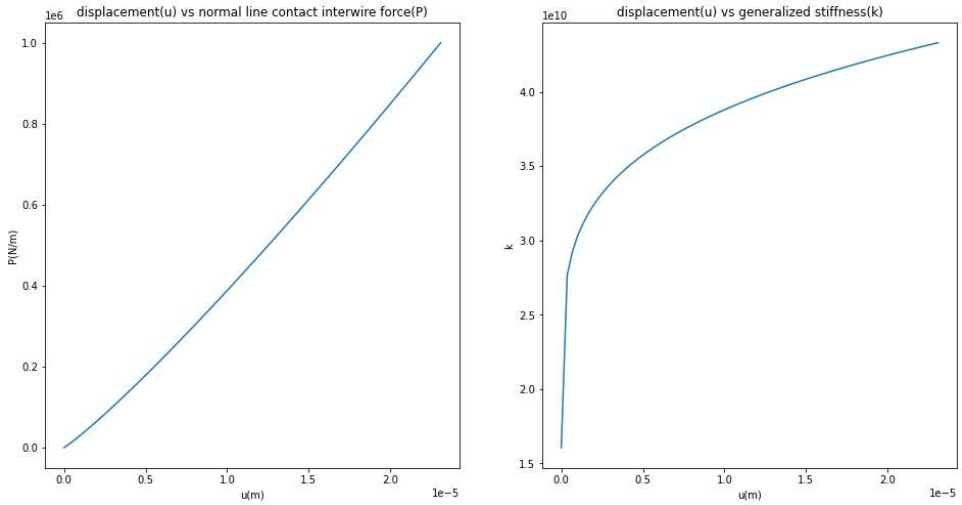

Figure 12: Force-displacement curve and the slope change based on the analytical solution. The latter is referred as the generalized stiffness in this figure, and it describes the nonlinearity of this elasticity behavior.

Interpolate the solution in evenly spaced discrete points, one can get the parameters for the nonlinear elasticity behavior in Abaqus. The stiffness for this nonlinear elasticity will be trivial as the contact starts and gradually increase to a constant value as the deformation propagates. This resembles the Hertzian contact between wires when a confining pressure, in this case, the clamping force is applied.

Besides the nonlinear elastic behavior, a failure behavior is also assigned to the connector in this direction. This ensure the connector will be deactivated and all the contact forces will cease if the wires are moving away from each other.

Connector Behavior in U3 direction

The longitudinal force, which is result from the friction between wires, is controlled by the connector behavior in U3 direction. In this case, the friction behavior is adapted in Abaqus and the parameters are determined by the pullout test [4].

Figure 13: Specimen Description:

•24-inch (600 mm) Specimen with 10-inch (250 mm) Center wire protrusion

•Two Rosettes of strain sensors on the six outer wires on either side of the Steel clamp

•Two strain sensors on the center wire

•Steel Clamp bolts torqued at 100 ft-lbs

In this pull-out test, the load is applied in two phases: the UTM was set to load control when the slipping rate of the center wire was insignificant and switched to displacement control when the center wire exhibited constant slipping. This demonstrated the 'stick-slip' behavior when it comes to the slippage of the center wire. Therefore, in the current model, there should also be two phases when there is longitudinal relative displacement between wires: One is the 'stick' phase in which the friction force is increasing but no significate slipping is occurring. The other is the 'slip' phase in which the wire shows consistent slipping and the friction force is a constant. In this case determining the elastic slip is crucial to obtain convergence solution. If the elastic slip is small, the wires will start slipping even when the pulling force is trivial, which can lead to an unstable model. Using the load data (Figure 14) from the experiment, the elastic slip can be calculated. The friction coefficient adapts a theoretical value of 0.4 and the normal force contributes to this friction force is the force in U2 direction.

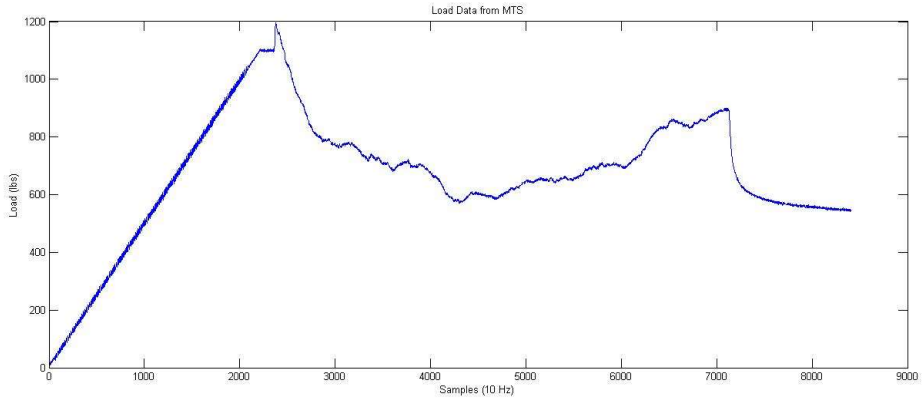

Figure 14: Tensile load time history from the pull-out test. The curve can be divided into two parts. The first part takes about 4 minutes (0 to 2400 samples) when there is no significate slip on the center wire. The second part takes about 7 minutes (2400 to 7000 samples). The total slip of part one and part two in this pull-out test is 10cm. Combine with the 1cm/min displacement control in part two, the slip in part one is calculated to be 2.3cm. In Abaqus, this number is taken as the elastic slip to determine the stick stiffness.

Connector behavior in U1 direction

If the physical principle of wire to wire interaction is strictly obeyed, one should have friction behavior in U1 direction as well. At first, the friction behavior in U1 direction is adapted. But further research shows that since the force in U1 direction is trivial, switching that behavior to linear elastic would not significantly alter the result (Figure 15, Figure 16). Furthermore, the computing speed is approximately one third faster if one adapts a linear elastic behavior in U1 direction (1048s compared to 711s). So, when modeling large problems, a linear elastic behavior in U1 direction is recommended. For clarification, all the results showed in the pull-out test modeling are based on the settings of nonlinear elastic and failure behavior in U2 direction, friction behavior in U3 direction and linear elastic behavior in U1 direction.

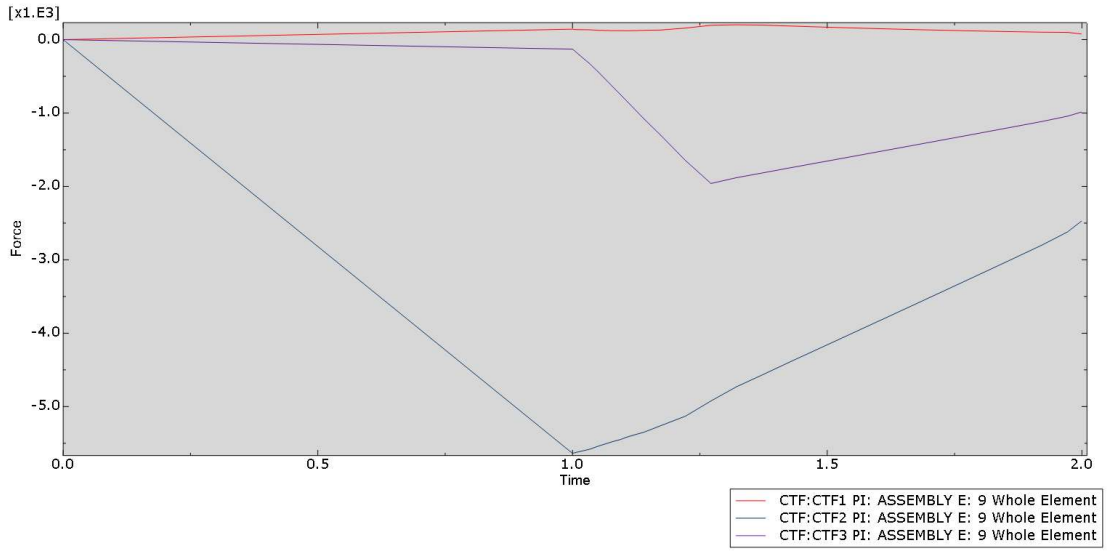

Figure 15: Force time history of one connector located at the center wire. CTF shows the connector total force in U1, U2 and U3 direction. Friction behaviors are adapted in both U1 and U3 directions. The specimen is loaded in two steps. In step one, only the bolt torque is applied on the clamp therefore the specimen only experiences the confinement from the clamping force and there is no longitudinal force. In step two, the clamping force remains, and a tensile load is applied at the center of the wire. It can be observed that the friction force in U3 direction, is gradually cumulating before it reaches 0.4 times the normal contact force.

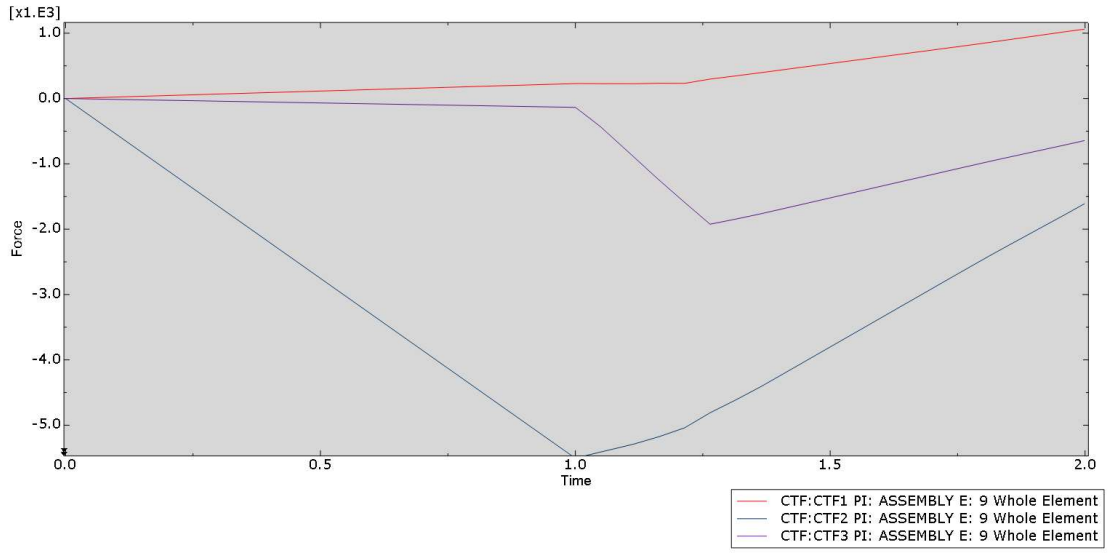

Figure 16: Force time history of one connector located at the center wire. CTF shows the connector total force in U1, U2 and U3 direction. Friction behaviors are adapted in only U3 direction and U1 is modeled with a linear elasticity behavior with a low stiffness. CTF2 and CTF3 are not affected by this change.

Pullout Test Modeling

With all the parameters for connector behaviors are determined, a pull-out test modelling is done in Abaqus and the results are compared to the experimental results. Based on the current model, some

boundary conditions and loads are adjusted to better resemble the experimental configuration. All previous constrains to ensure symmetric behavior are removed. For the outer six wires, one end is completely released, and the other end is fixed. A tensile load is applied on the center wire to produce the slipping of the wire. The clamping force is adjusted, but since the clamp geometries are different, the discrepancy in the results is expected.

By postprocess the data from Abaqus, the total friction force can be obtained. For a 10 cm displacement in the center wire, the total friction force is 22000N (Figure 17), which is five times larger than the result in the experiment. This could result from the bulker clamp used in the Abaqus model. Using the same bolt torque, the clamp in the model can produce larger clamping force and therefore the friction force is higher in the model. Another possible reason is the overestimation of the friction coefficient. The outer layer of the wire was tearing out during the experiment, which can result a smaller value. To further validate the result, acquiring the calibrated clamping force in the pull-out test is recommended.

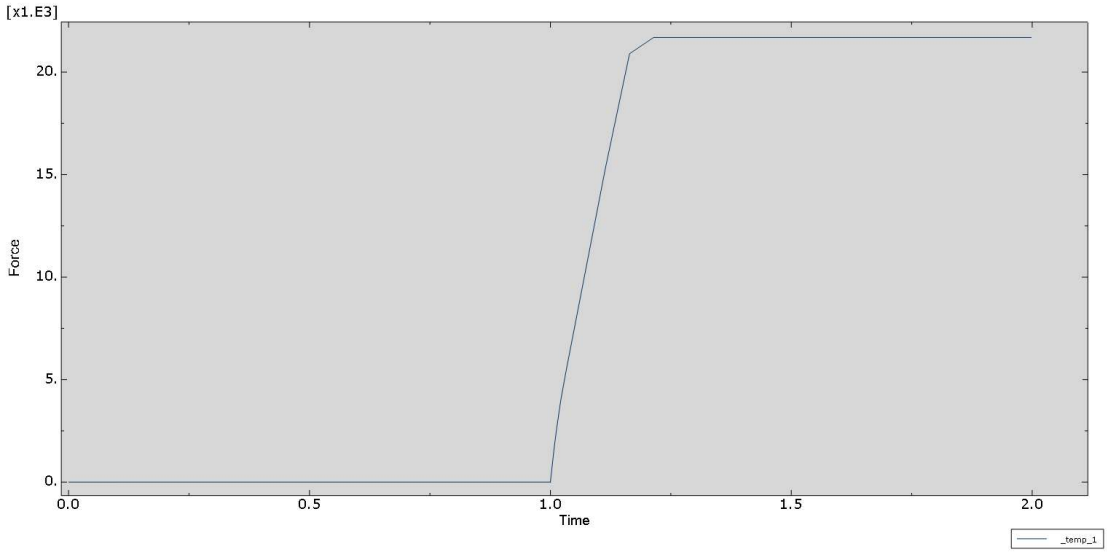

Figure 17: Time history of the total friction force on the center wire. This is done by summing all the connector forces in U3 direction for connector located at the center wire. The load is also applied in two steps as discussed before.

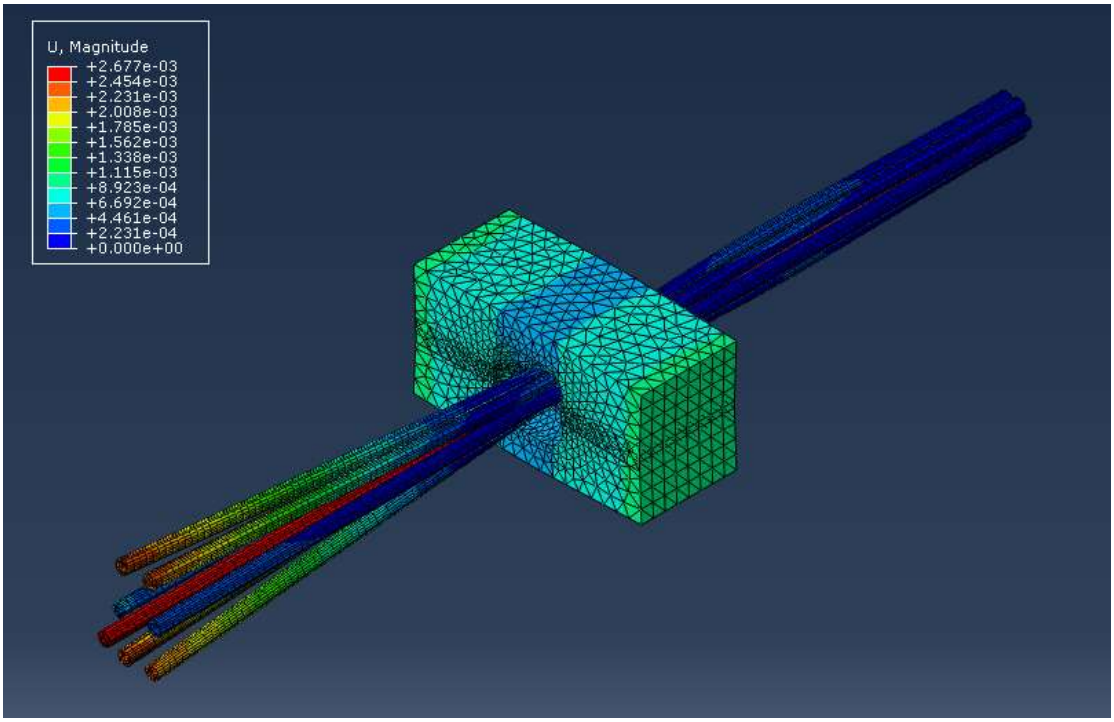

Figure 18: Deformed shape of the pull-out test with a scale factor of 5. The p-delta effect on the fixed side can be observed from this figure.

Results and Discussion

The model has been updated mainly on the connector behaviors. New behaviors have been added into the model and the parameters are set. The current model can model friction and achieve convergence with good computing efficiency. The results can simulate the deformed shape in experiment such as the p-delta effect on the restrained end and the spreading of the outer wires on the free end (Figure 18). However, the accuracy is still undetermined. More experimental data is favored to further validate the result.

References

[1] Wriggers, P. (2006). Computational contact mechanics, 2nd Ed., Springer, New York.

[2] Wang, K. (2020). Cable Contact Finite Element Modeling.

[3] Raoof, M. and Huang, P. (1991). Wire recovery length in suspension bridge cable. Journal of Structural Engineering. Volume 118 Issue 12

[4] Goel, S. (2014). Neutron diffraction strain testing of suspension bridge cable. Bachelor thesis Columbia University

CHAPTER III: 3D MODELING OF EXPERIMENTAL COOLING PROCESS IN SUSPENSION BRIDGE MAIN CABLE

Tairan Li

Introduction

Based on the previous work done in two-dimensional modeling of the cooling process in suspension bridge main cable [1], a three-dimensional model is required to take the radiative and longitudinal conductive heat transfer into account. To simulate the experimental cooling process in three dimension, new material properties, parameters of heat transfer and initial condition need to be determined. Thus, our research process is clearly divided into two parts: (1) three-dimensional modeling of experimental cable cooling and (2) comparing the cooling model with experimental data.

This report briefly introduces some basic information about the suspension bridge main cable and the cooling experiment conducted in Carleton Laboratory in 2019 [2], then the process of establishing a three-dimensional cooling model of the cable is presented. By using ABAQUS finite element software, the model would be able to simulate the temperatures through the whole cable under experimental cooling condition. After comparing the simulation result with the experimental data, this model would be verified to be feasible or not.

To clearly present this work, this report is organized into the following four major sections: (1) problem statement, (2) modeling of three-dimensional cable cooling, (3) analysis of simulation results and (4) conclusions.

Problem Statement

Main Cable Construction

For this work, the cooling model is based on the main cable experimental mock-up in the Carleton Laboratory at Columbia University. The cable mock-up at Columbia is meant to replicate a typical panel (the length of main cable between adjacent vertical suspenders) of a medium-sized suspension bridge main cable. In this main cable, there are a total of 9,085 ASTM A586 high-strength steel wires (Figure 19(a)) each with a diameter of 5mm. The cable is made up of 61 hexagonal strands, and each of them is composed of a total of 127 high-strength steel wires (Figure 19(b)). Additional individual wires were used to fill any gaps and complete a circular cross-section. Outside of these wires, there

are external wrapping layers and protective shields. Ultimately, the full cable was set to measure 6.096m in length and 0.508m in diameter. At room temperature (20°C), the wires have an elastic modulus of 206GPa, a yield stress of approximately 1400MPa and an ultimate stress of approximately 1700MPa [3]. The main cable construction is shown in Figure 21.

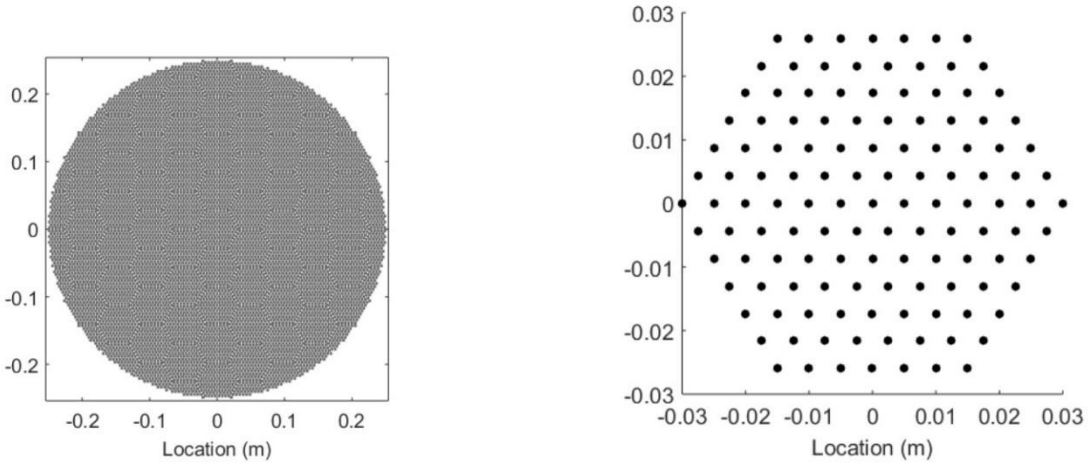

(a) 9085-wire Cable

(b) 127-wire Strand

Figure 19: Centroids of the total 9085-wire cable and the constituent 127-wire strand [3]

Experimental Data of Cable Cooling

In total, the cable was tested and monitored for 108 hours continuously. The entire procedure consists of heating the cable for 36 hours continuously and allowing the cable to cool down in natural ambient conditions (no forced cooling), so the sensor temperature within the cable at thirty-sixth hour is the initial condition of this modeling. Figure 20 shows the general sensor layout on a single cross-section for the main cable. This instrumented cross-section exists at four different locations along the length of the cable (Figure 21): the center, 51 cm (20 in.) to the right of the center, 102 cm (40 in.) to the right of the center, and 203 cm (80 in.) to the right of the center.

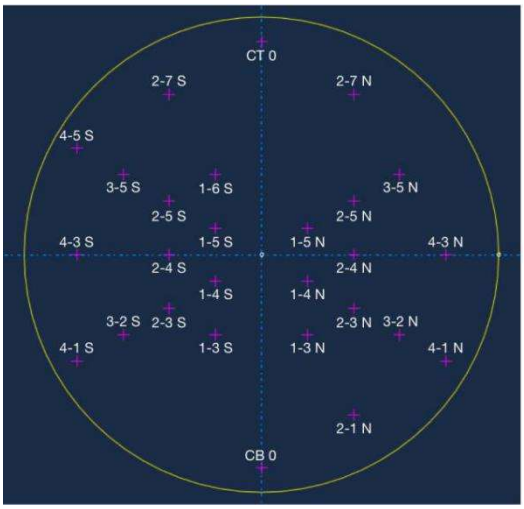

Figure 20: Location of sensors in bridge main cable experiment

Due to the symmetry of the cable construction and heat transfer condition in the longitudinal direction, we consider that there are seven instrumented cross-sections in total. Besides the first four described above, the other three are 51 cm (20 in.) to the left of the center, 102 cm (40 in.) to the left of the center, and 203 cm (80 in.) to the left of the center.

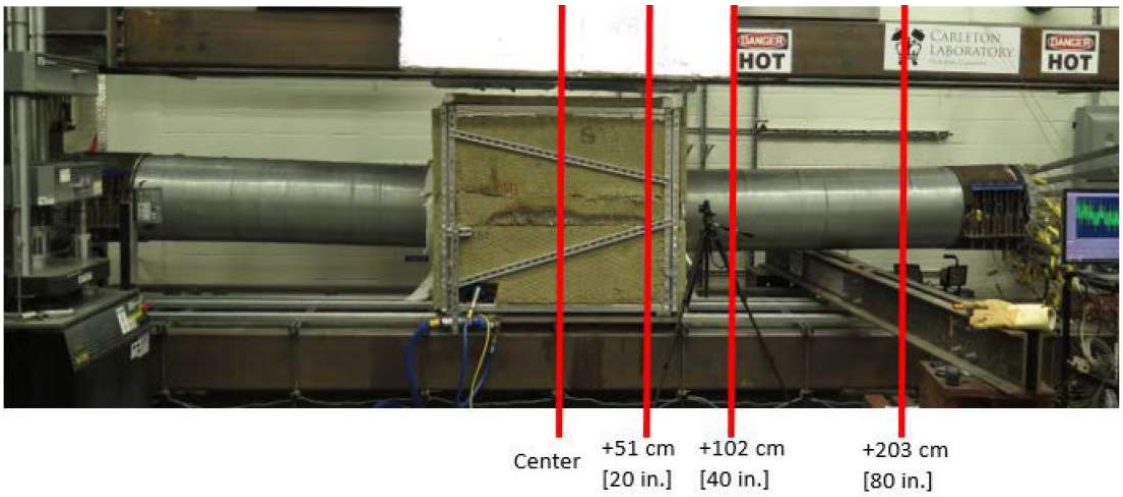

Figure 21: Locations of instrumented cross-sections [2]

As a reminder, the sensor data during the second and third hours of cooling is missing due to data acquisition equipment issues. For later temperature comparison and error analysis, we will only present the results after the cable has been cooled for one, four and five hours.

Modeling of Three-Dimensional Cable Cooling

For experimental cooling condition, the modeling consists of four important parts: (1) geometry, (2) material properties, (3) parameters of heat transfer and (4) initial condition.

Geometry

The main cable is composed of thousands of 5 mm diameter high-strength steel wires. Outside of these wires, there are external wrapping layers and, for some bridges, protective shields. Obviously, these elements create a completely heterogeneous environment. Defined by the dimension of the cable mock-up in experiment, we consider the cable to be a cylinder with a diameter of 0.508 meters and a length of 6.096 meters. In this work, we concentrate on the temperature variation through the whole main cable, so it cannot be simply modeled as a homogeneous and isotropic solid domain any more.

Material Properties

Due to the fact that the cable has distinct material properties in cross-sectional and longitudinal direction, we consider the whole cable as a heterogeneous but orthotropic cylinder with effective material properties in two different directions. This means we cannot use the mechanical and thermal properties of single wires directly to define the material of cable in ABAQUS. In other words, we have to treat the cable as two different parts, and both of them is respectively made from a new single material with homogeneous (and in some cases, temperature-dependent) properties.

Based on above assumption, the material properties of the full-scale cable would be determined in the following two directions.

Material Properties in Cross-Sectional Direction

In the cross-sectional direction, the material properties remain the same with what we used in the two-dimensional modeling of the cable cooling, which are defined from a combination of a recent experimental results performed by J. Robinson [2] and previous work done by M.J.D. Sloane in 2016 [3]. At room temperature, the cross-section of the cable will be defined by a thermal conductivity, K_C, of approximately 1.55W/m/°C, a specific heat at constant pressure, C_p, of 503.2J/kg/K, a Young's modulus, E, of 205GPa, a Poisson's ratio, γ, of 0.3, and a mass density, ϱ, of 7101kg/m^3.

Material Properties in Longitudinal Direction

Along the longitudinal direction of the bridge main cable, there are three main components conducting heat in this direction. They are steel wires, external wrapping layers and air in the gaps among wires. The wires are ASTM A586 high-strength steel, which has a much higher thermal conductivity compared with the other two components. In this condition, the steel wires have the dominance of conducting heat in the longitudinal direction. Imagining the heat transferred in the longitudinal direction of the cable as water delivered by tube, the thermal conductivity in longitudinal direction is determined by the total cross-sectional area of all the steel wires in the cable.

$$a = \frac{n\pi r^2}{\pi R^2} = \frac{9{,}085\times\pi\times 0.0025^2}{\pi\times 0.254^2} = 88\% \qquad (1)$$

As we mentioned before, there are a total of 9,085 steel wires in the cable, and each of them has a diameter of 5mm. The diameter of the whole cable is 0.508 meters. Eq.(1) shows the area ratio of steel wires on the whole cable cross-section, where *a* is the area ratio, *n* is the number of steel wires in the cable, *r* is the radius of a single steel wire, and *R* is the radius of the whole cable. Therefore, the thermal conductivity along the longitudinal direction should be 88% of the thermal conductivity of a single steel wire. Let the thermal conductivity of single steel wire have the value applied previously in the model done by M.J.D. Sloane in 2016 [3], which is 45.5104W/m/°C at room temperature, so the longitudinal thermal conductivity of the cable , K_L, is defined as 40.05W/m/°C at room temperature.

Other material properties could also be determined by this area ratio of steel wires on the whole cable. The specific heat is defined as the amount of heat per unit mass required to raise the temperature by one degree Celsius. Based on this concept, the specific heat along the longitudinal direction should be 12% more than that of a single steel wire. This value is very similar to the specific heat in the cross-sectional direction, so we consider these two parameters to be the same for the sake of simplicity.

For the mechanical properties, such as the Young's modulus and Poisson's ratio, their values in cross-sectional direction are very similar compared to the values of a single steel wire, which means these parameters are not affected much by the construction of the cable, so we consider these mechanical properties on the two different directions to be the same. Apparently, the density should also be the same on the two different directions. Finally, all the material properties required in the modeling are defined.

The previous research [2] has proved that the thermal conductivity in the cross-sectional direction and the density would not change much with the variation of temperature, so all material properties except these two parameters will be treated as temperature-dependent in the modeling. All the material properties that would be used in the three-dimensional modeling of cable cooling are listed in Appendix A.1.

Parameters of Heat Transfer

By analyzing the flaws and limits of the two-dimensional model, now it could be confirmed that the three-dimensional model must include both the natural convection and radiation between the cable and its ambient environment. For each form of heat transfer, there are corresponding parameters to be determined to define the process of heat transfer.

Natural Convective Heat Transfer

For a natural air-cooling process, based on previous modeling done in the two-dimensional cross-section of the cable [1], we know it is ruled by Newton's law of cooling [4]. The natural convective heat transfer coefficient is the parameter we must determine to define the process of heat transfer.

The natural convection of heat transfer between the cable and its ambient environment would be defined on two different types of surface on the cable. Considering the bridge main cable as a cylinder, the first type is the natural convection on the curved surface on the side of the cylinder (Figure 22), and the second one is on the flat surfaces at two ends of the cylinder (Figure 23).

Natural Convection on Curved Surface of Cable

We opt to apply Churchill and Chu's method [5] to estimate the convective heat transfer coefficient in this cable cooling condition. This method is applicable for natural convection from a long horizontal cylinder. By applying this method, we obtain one uniform heat transfer coefficient on the curved surface of cable.

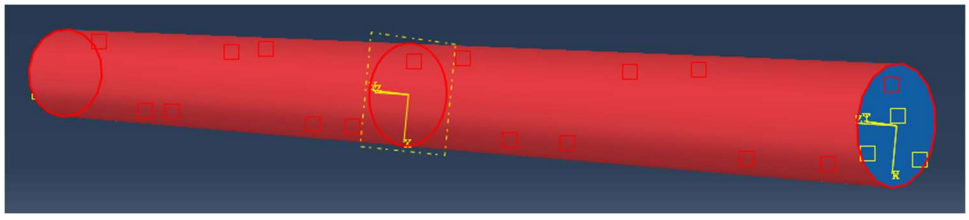

Figure 22: The curved surface on the side of the cylinder (in red)

The detailed calculation process of this coefficient in natural air-cooling condition on curved surface is shown in Appendix 2. Finally, a natural convective heat transfer coefficient of 7.48W/m^2/K results from the calculations.

Natural Convection on Flat Surfaces of Cable

On the flat surface, another method from Churchill and Chu [6] is applied to estimate the heat transfer coefficient. This method is applicable for natural convection from a vertical surface. By applying this method, another uniform heat transfer coefficient is obtained on the flat surfaces of cable.

For this method, the process of calculation is very similar to that one utilized on the curved surface. The only difference lies in the correlation among Nusselt, Grashof and Rayleigh number, which is shown in Appendix A.3. Other parameters used in the computational process remain the same. In the end, a natural convective heat transfer coefficient of 6.14W/m^2/K comes from the calculations.

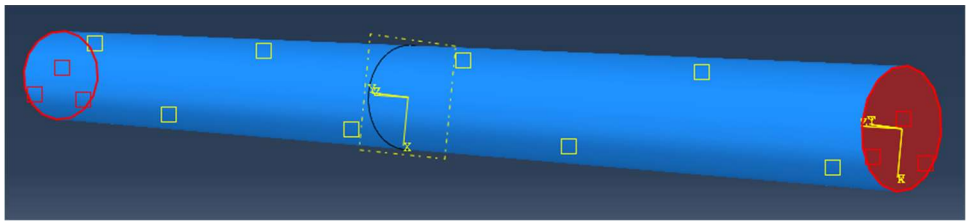

Figure 23: The flat surface at two ends of the cylinder (in red)

Radiative Heat Transfer

Heat transfer by thermal radiation is the transfer of heat by electromagnetic waves. It is different from conduction and convection as it requires no matter to be present for transmission. In the experiment, after the furnace is deactivated, the heated cable radiates energy in the form of photons moving in a random direction with random phase. When radiated photons reach another surface, they may either be absorbed, reflected or transmitted. During this process, heat is transferred between cable and another surface (possibly the reaction frame in which the cable is mounted).

In the quantitative aspect, radiation is described by Stefan-Boltzmann law. Ruled by this law, we consider the cable as a hot gray body radiating energy to its cooler surroundings, and the net radiation heat loss rate can be expressed by eq.(2).

$$q = \varepsilon\sigma(T_h^4 - T_c^4)A_h \qquad (2)$$

where q is heat transfer per unit time, ε is emissivity coefficient of the object, σ is the Stefan-Boltzmann constant which is defined as $5.6703\times10^{-8}\mathrm{W/m^2/K}$, T_h is hot body absolute temperature, T_c is cold surroundings absolute temperature, and A_h is the area of the hot object.

In ABAQUS, we only need to determine the emissivity coefficient to define a surface radiation. For general unpolished steel, the emissivity coefficient is about 0.7 to 0.9, so we determine 0.8 as the value of emissivity coefficient of the cable surface.

Initial Conditions

To simulate the cooling process in the experiment, the initial condition of model must be based on temperature sensor data, instead of uncalibrated heating models in previous research. Experimental data consists of temperature measured at discrete points, but we need to define the temperature distribution through the whole body of the full-scale cable functionally for interpolation to nodal values within the ABAQUS model.

Applying mapped field to define the initial condition has been verified to be not feasible. It cannot simulate a reasonable initial temperature distribution on central cross-section of the cable, and its results also produce unacceptable errors. In this condition, we have to define the initial condition by applying expression field.

Strategy for Definition of Initial Condition by Expression Field

Compared to the two-dimensional problem, the problem in definition of initial condition is more complicated in current modeling. To define the initial temperature of every nodes within the cable, we could determine the expressions of temperature from cross-sections to the whole body. This strategy is firstly to determine the initial temperature distribution on the four cross-sections instrumented with temperature sensors, and then by assuming the longitudinal temperature gradient between each cross-sections to be linear, the initial temperature distribution of the whole cable could be defined.

On Instrumented Cross-Sections

This work is performed by Jumari Robinson in Python, where the nodal temperatures from each sensors are interpolated to fit the expression in polar coordinate system. The detailed process is presented in Appendix A.4, and four initial temperature expressions are determined corresponding to

each instrumented cross-sections. In ABAQUS, the initial condition on four instrumented cross-sections is presented by Figure 24.

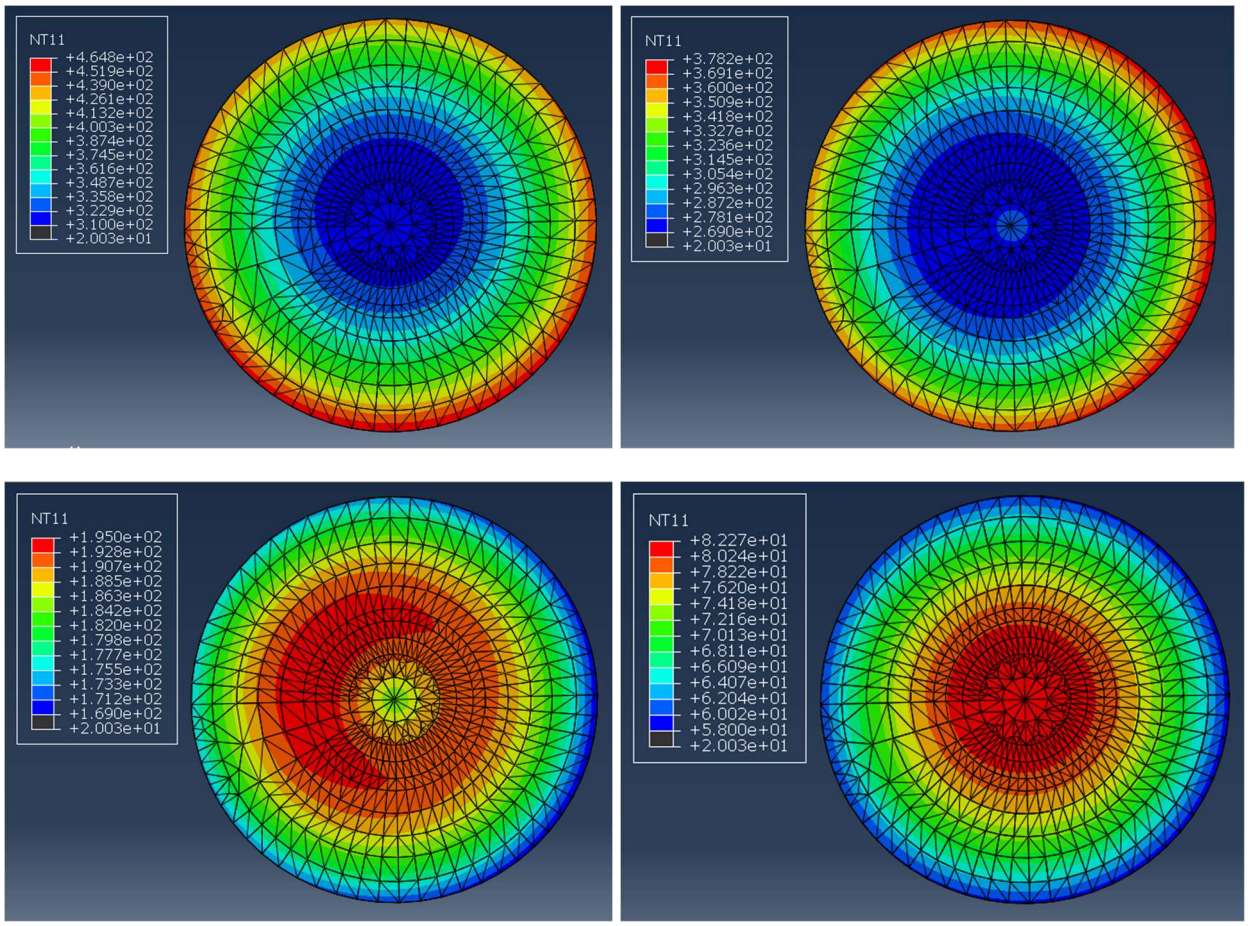

Figure 24: Top left: The initial condition on the central cross-section. Top right: The initial condition on the cross-section at 20 in. away from center. Bottom left: The initial condition on the cross-section at 40 in. away from center. Bottom right: The initial condition on the cross-section at 80 in. away from center.

Through the Whole Cable

As shown in Figure 25, from the center to the end of the cable, the expressions of initial temperature distribution on each instrumented cross-sections are denoted to T_0, T_1, T_2 and T_3 respectively. For the sections between each instrumented cross-sections, the longitudinal temperature gradient is assumed to be linear.

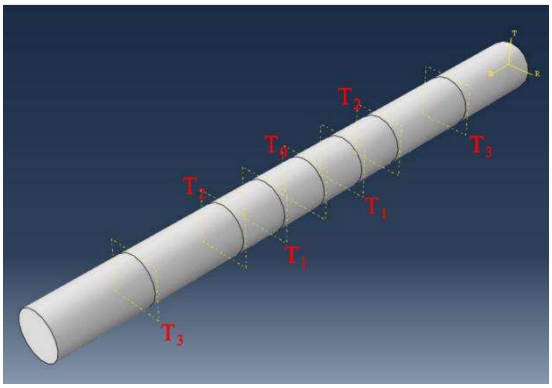

Figure 25: The denotation of expressions on each instrumented cross-sections

The initial temperature of every nodes within a section could be defined by the temperature distribution on the cross-sections at two ends of that section. Take the section between T_1 and T_2 as an example. The initial temperature within this section is expressed by eq.(3).

$$T_{20-40} = T_1 - \frac{T_1 - T_2}{L_2 - L_1} \times (Z - L_1) \qquad (3)$$

where L_2 is 1.016m, the distance between the center and the cross-section corresponding to T_2; L_1 is 0.508m, the distance between the center and the cross-section corresponding to T_1; and Z is the longitudinal distance between a specific node and the center of the cable.

For the sections at two ends of the cable, the cross-sections are not instrumented with temperature sensors, so we miss the initial temperature distribution on them, and similar equation as eq.(3) could not be applied in this condition. However, by the observation during the experiment, we assume the initial temperature at the ends of the cable to be uniform 20°C, and the initial temperature distribution within the end sections is expressed by eq.(4).

$$T_{80-En} = T_3 - \frac{T_3 - T_{end}}{\frac{1}{2}L - L_3} \times (Z - L_3) \qquad (4)$$

where T_{end} is 20°C, the uniform initial temperature at cable ends; L is 6.096m, the length of the whole cable; and L_3 is 2.032m, the distance between the center and the cross-section corresponding to T_3. In ABAQUS, the initial condition through the whole cable is presented by Figure 26.

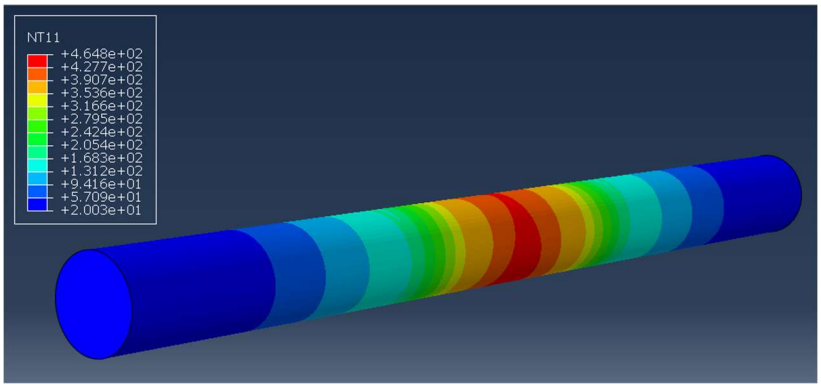

Figure 26: The initial condition through the whole cable

Results and Discussion

Based on the recent experimental results from work done by J. Robinson in 2019 [2], we could model the cooling conditions in the full-scale main cable heat transfer experiment and compare the simulation results with the sensor data to see if this cooling model is reasonable and applicable. After this three-dimensional model is established, we could calculate the error between experimental data and simulation results and then conduct the further optimization of this model to accurately represent the physical system.

Figure 27 shows the simulated temperature distribution on the center cross-section of the cable during the first five-hours cooling process in the experiment. The variation of the temperature conforms the general rule of heat transfer, which could also be verified from the aspect of the whole cable. Figure 28 shows the simulated temperature distribution through the whole cable during the first five-hours cooling process in the experiment.

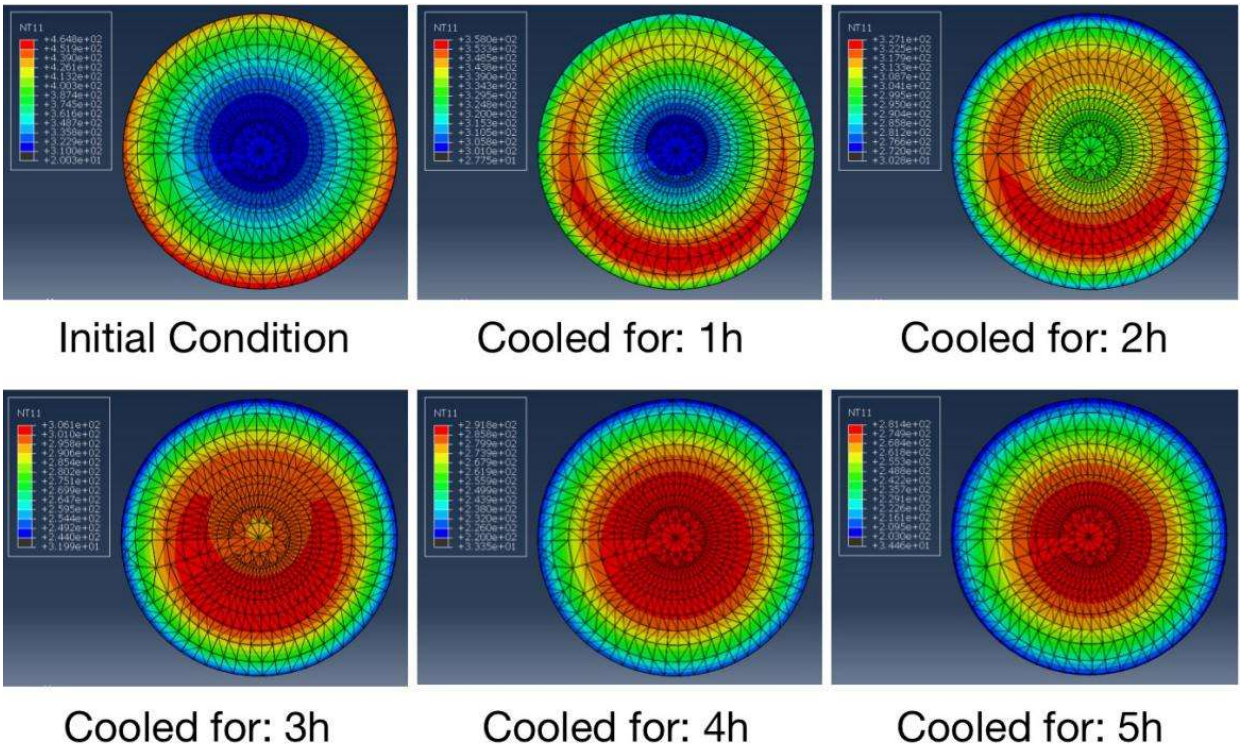

Figure 27: Simulated temperature distribution on the central cross-section of the cable during the first five-hours cooling process in the experiment

The percentage error of the simulation results at each sensor location for each time was calculated as:

$$e = \frac{(T_{simulation} - T_{sensor})}{T_{sensor}} \times 100 \qquad (5)$$

On the central cross-section of the cable, the following four figures show the absolute errors between sensor data and simulation results at different cooling time. Each error is marked near the location of corresponding sensor. The detailed data is offered in Appendix A.5. If we consider the errors less then 10% to be acceptable, it is obvious that the simulation results are reasonable at most location of sensor especially after the first hour of experimental cooling. The errors exceed 10% only at the following eight senors: CT 0, CB 0, 2-1 N, 2-7 S, 4-1 N, 4-1 S, 4-3 S, 4-5 S, and they are all located in the area near the surface of the cable.

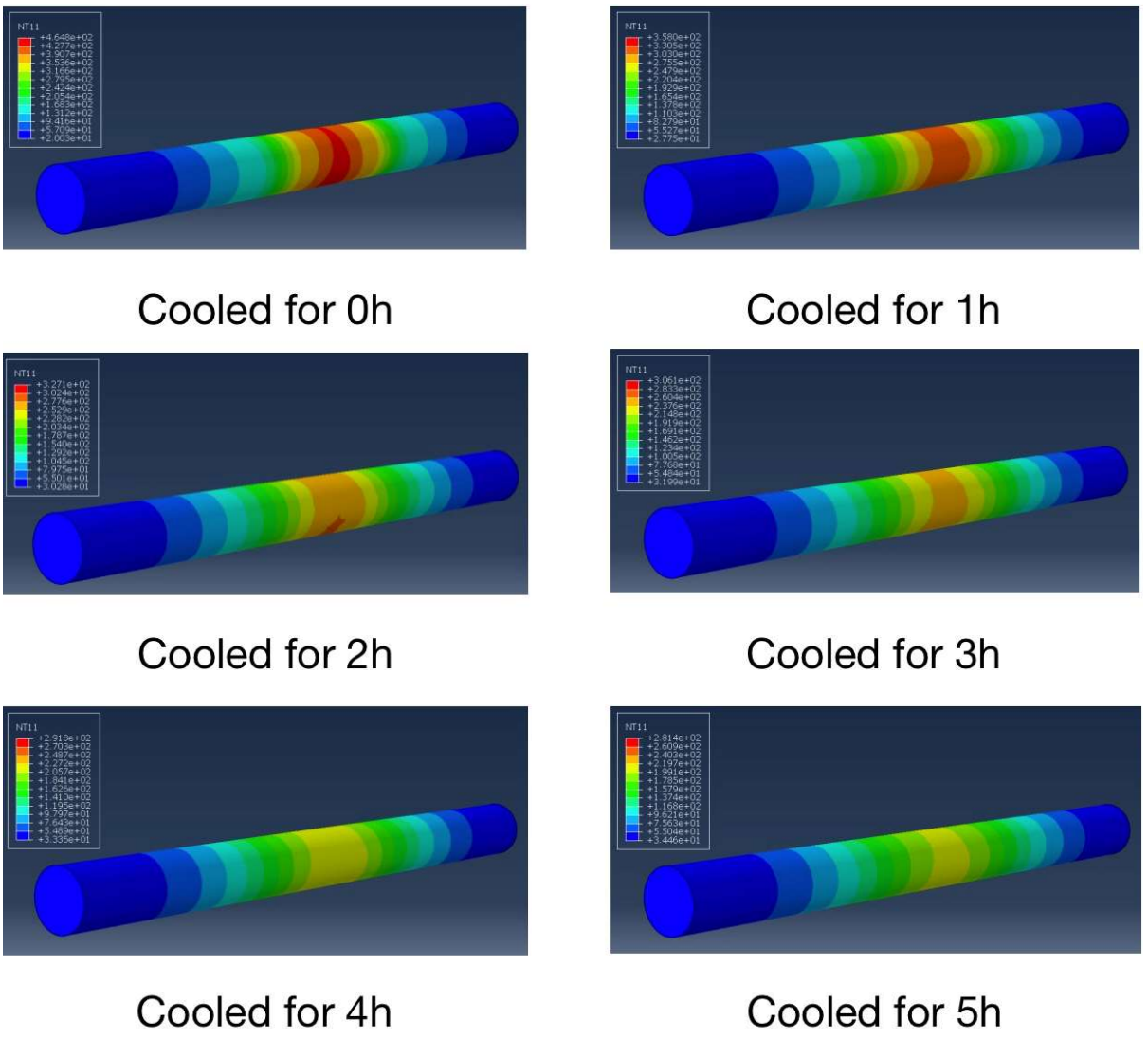

Figure 28: Simulated temperature distribution through the whole cable during the first five-hours cooling process in the experiment for in 1-hour intervals for the first five hours.

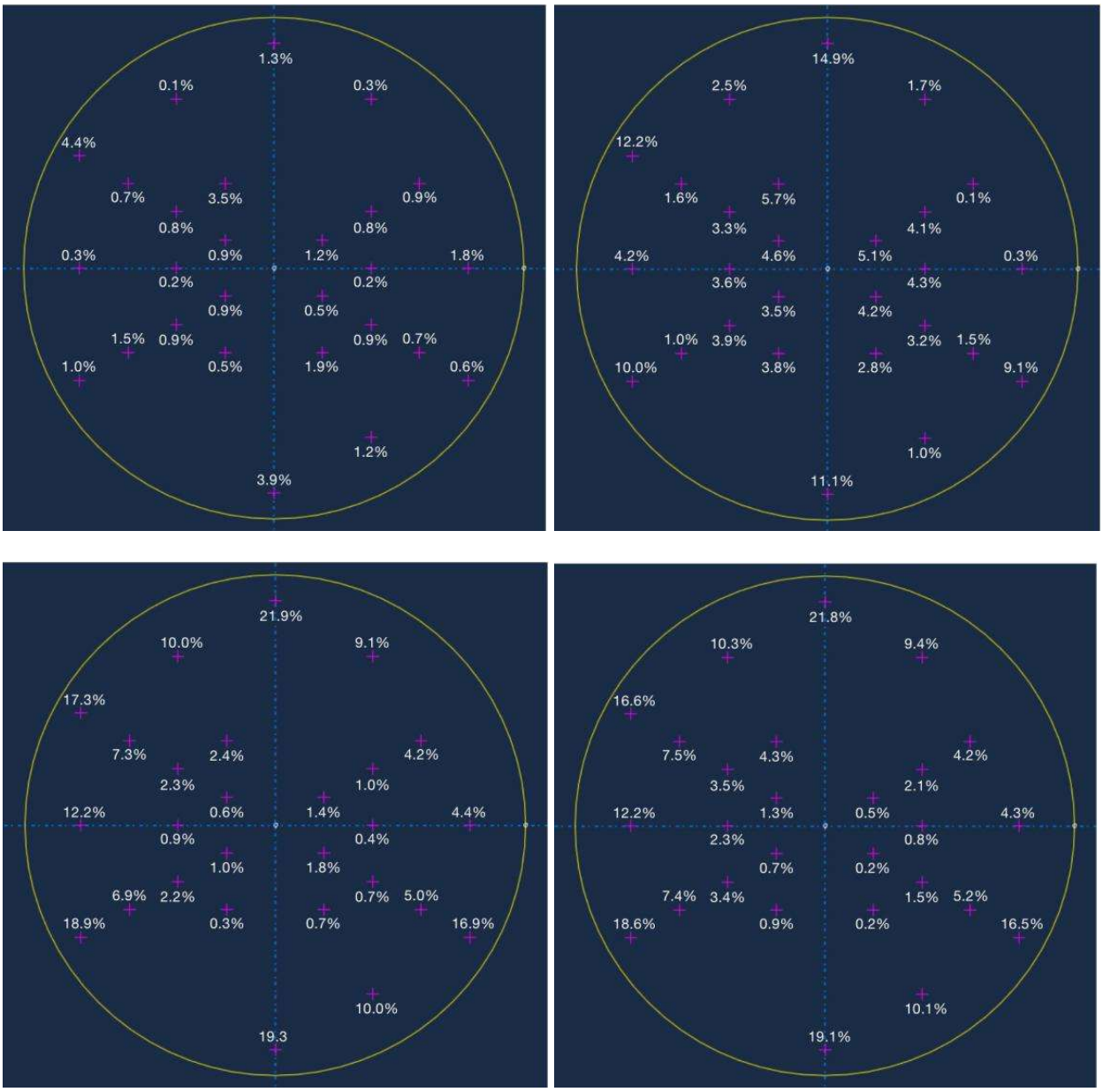

Figure 29: The errors between sensor data and simulation results on center cross-section in initial condition of experimental cooling condition (top left), 1h from IC (top right), 4h from IC (bottom left), and 5h (bottom right).

For the area near the surface of the cable, the heat transfer within this area would be affected by many factors from the ambient environment. Most of these factors could not be recognized due to the complication of the external environment, so it could not be modeled by the finite element software. Now that it is very hard to predict the specific temperature within this area, in this condition, we could neglect this area when we evaluate the feasibility and reliability of the cable cooling model. For the current model established in this report, it could produce reasonable results everywhere on the central

cross-section except for the area near the surface of the cable, so it could be considered to be feasible and reasonable.

Conclusions

In this work, we have developed ABAQUS finite element models for the experimental cooling process of suspension bridge main cable in three dimensions. The model simulates the cooling condition during the experiment conducted by J. Robinson in 2019 [2]. Including natural convective and radiative heat transfer between the cable and its ambient environment, the model is defined as an orthotropic cylinder with different thermal conductivity at cross-sectional and longitudinal direction. The initial condition of this model is defined by expression field in ABAQUS. It is expressed firstly on the cross-sections instrumented with sensors and then interpolated though the whole body of main cable by assuming a linear longitudinal temperature gradient.

To check the feasibility and reliability of this cooling model, we compare the simulation results produced by the three-dimensional model with the sensor data recorded during the experiment. By calculating the errors between simulation results and experimental data at every sensor in different cooling time, it is verified that this model could simulate the temperature variation during the experimental cooling accurately within most area on the central cross-section except for the area near the surface of the cable. Considering the complication of the factors affecting heat transfer in this area, the unacceptable errors produced near the surface of the cable could be neglected. All the rest errors between simulation results and experimental data on the central cross-section of cable is less than 10%, which is considered to be acceptable. Therefore, this three-dimensional model established in this report is evaluated to be a feasible and reasonable model to simulate a suspension bridge main cable in the experimental cooling condition.

References

[1] T. Li. (2020) Active Cooling Modeling of Bridge Main Cable. Columbia University.

[2] J. Robinson. (2019) Fire Effects on Main Cables of Suspension Bridges: Working Draft of Final Report. Columbia University.

[3] M.J.D. Sloane. (2016) Fire effects on suspension bridge main cables: methods for determining both temperature and strain distributions within an exposed cable. Columbia University.

[4] R.H.S. Winterton. (1997) Heat Transfer. Oxford University Press: Oxford, New York, 24–29.

[5] S.W. Churchill, H.H.S. Chu. (1975) Correlating equations for laminar and turbulent free convection from a horizontal cylinder. Int. J. Heat Mass Transfer, 18:1049- 1053.

[6] S.W. Churchill, H.H.S. Chu. (1975) Correlating equations for laminar and turbulent free convection from a vertical plate, Int. J. Heat Mass Transfer, 18:1323-1329.

[7] H. H. Bengtson. Convection Heat Transfer Coefficient Estimation, an online article at www.s3.amazonaws.com.

CHAPTER IV: ELASTO-PLASTIC DEFORMATION OF BRIDGE CABLES

Jackson Burdett

Abstract

A MATLAB algorithm was created to simulate the elastic-plastic effects of bridge cable wires under a radial transient temperature field. An initial single wire model was formulated using a Newton-Raphson iteration method and the Ramberg-Osgood power relationship. The wire was given an incremental displacement for which we seek the stress response given temperature-dependent elastic and plastic properties. The resulting elastic and plastic strains (and thus incremental stress) within wires is determined using temperature-dependent elastic modulus, work hardening coefficient and exponent in the Ramberg-Osgood power-law strain hardening relationship. The algorithm can apply Ramberg-Osgood isotropic hardening, Ramberg-Osgood isotropic & kinematic hardening, and elastic-perfectly plastic conditions. Consequently, a model was developed to perform the same analysis on an arbitrarily large group of parallel wires, all tied in displacement at their ends, with varying temperatures. Due to the decoupled mechanics of the system of wires, the algorithm was able to manage all the wires using the same base code from the single-wire model. The algorithm was used to compare the hardening models of a 61-wire cable in a specific temperature domain. A model was then derived to analyzed a 61-wire cable in an axially expanded domain.

Introduction

There was previous work done by Jumari Robinson that modeled the temperature-dependent stress-strain curves of a single wire and a 61-wire cable under elastic-perfectly plastic conditions in MATLAB. The wires are made of ASTM A586 steel. Figure 30 is a simplified representation of his work as a 3-wire model with different stiffness and nodal origins.

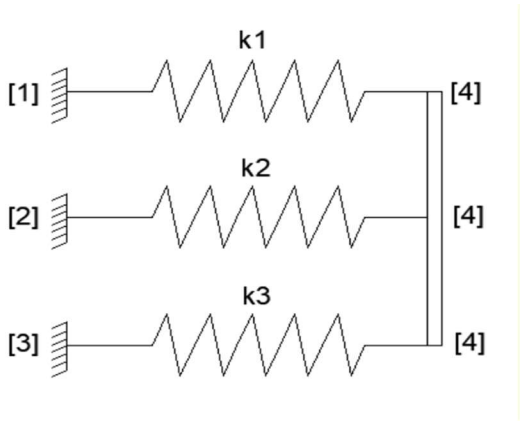

Figure 30: A basic schematic representation of a multiple-wire cable system illustrated with fixed springs (Robinson)

Jumari Robinson's simulation is based on previous experimental data from single wire and cable thermomechanical testing. The elastic-perfectly plastic model imparts temperature-dependent elastic loading until temperature-dependent yield stress (from experimental data) is attained and held until temperature dependent ultimate strain (from experimental data) is reached, producing fracture (

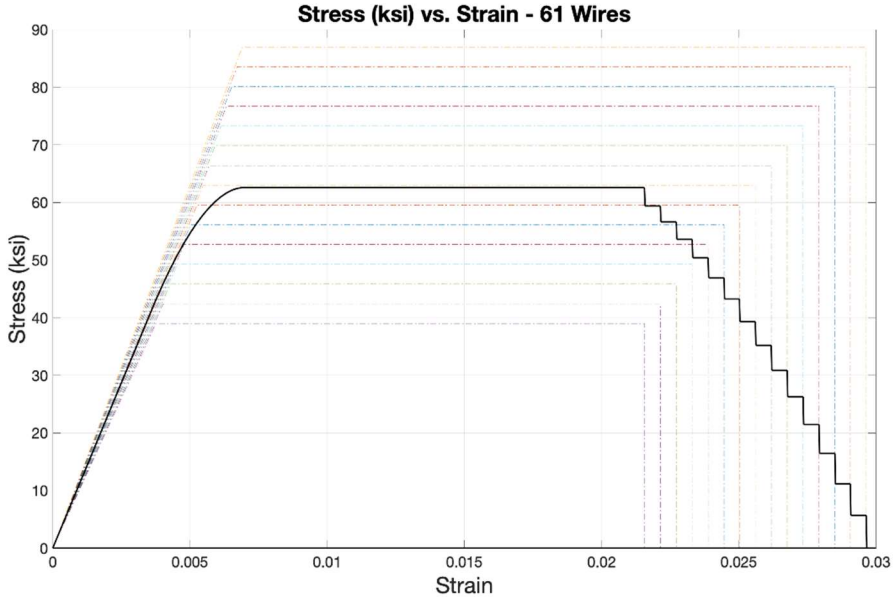

Figure 31).

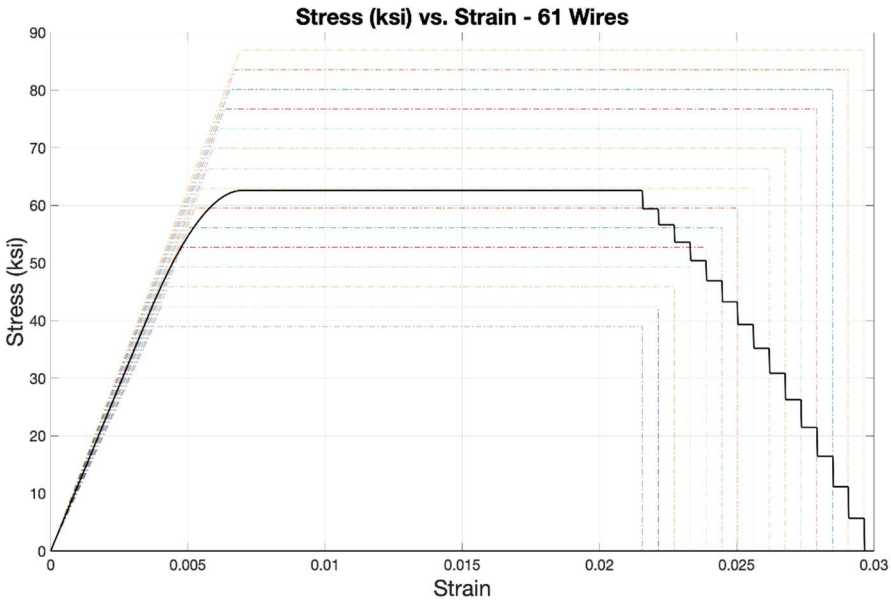

Figure 31: Represents the results from Jumari Robinson's 61-wire model without temperature dependence (Robinson)

Elastic-Plastic Deformation Theory

Elastic-plastic deformation includes a nonlinear increase in stress, with respect to strain, after the material has begun yielding. The strain includes both elastic and plastic components. To determine the emanating stress given an increase in strain, a Newton-Raphson iterative method is employed. This procedure uses a trial stress from the temperature-dependent Young's Modulus and a given incremental strain to compute the consistency parameter, γ. The consistency parameter determines the plastic strain development to conclusively obtain the subsequent stress, shown in *Figure 32*.

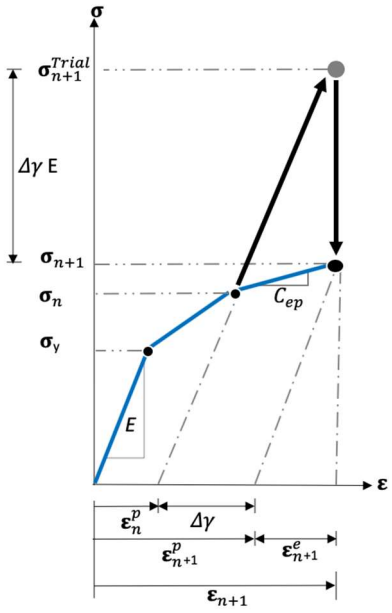

Figure 32: The Newton-Raphson iteration method used to determine the stress from an increment of strain. The algorithm finds a trial stress from the previous plastic strain ε_n^p and the Young's Modulus E, then downward maps to the subsequent stress σ_{n+1} from the formulation of the consistency parameter γ and elastic-plastic modulus C_{ep}. Additionally, it computes in the subsequent plastic strain ε_{n+1}^p and subsequent elastic strain ε_{n+1}^e which formulate the subsequent strain ε_{n+1} from the initial strain increment.

Once the temperature-dependent yield stress (obtained from experimental data) is reached, the algorithm commences the elastic-plastic Newton-Raphson method to find the subsequent stress. To find the elastic-plastic modulus C_{ep}, the Young's Modulus and the consistency parameter are utilized to map downward to the subsequent stress. The subsequent plastic strain, ε_{n+1}^p continues its development from each iteration's modification in the consistency parameter. However, the succeeding elastic strain ε_{n+1}^e is determined by the recently obtained stress and the Young's Modulus. The consistency parameter is ascertained from the iteration method's initialization of a counter, a max iteration, and a tolerance of a function *R*. The Jacobian of the function *R* (representing the residual

error between the trial stress and iteration stress) is used to acquire the value of the consistency parameter. The iterations continue until the function *R* is determined to be less than the tolerance or until the maximum iteration is established, shown in

1. Set $\Delta\gamma = 0$
2. Calculate R, where $R = f_{n+1}^{trial} - \Delta\gamma E - G(a_n + \Delta\gamma) + G(a_n)$ and $G(a) = \sigma_n + Ca^m$
3. Initialize variables:

   Set $maxiter = 10$

   Set $k = 0$ (the iteration counter)

   Set $tol = 10^{-5}$

   Set $d_g = 0$
4. WHILE $|R| > tol$ and $k < maxiter$:

   $$\frac{dR}{d\Delta\gamma} = -E - mC(a_n + \Delta\gamma)^{m-1}$$

   $$d_g = -\left[\frac{dR}{d\Delta\gamma}\right]^{-1} R$$

   Update $\Delta\gamma = \Delta\gamma + d_g$

   Recalculate $R = f_{n+1}^{trial} - \Delta\gamma E - G(a_n + \Delta\gamma) + G(a_n)$

   Update $k = k + 1$

   END WHILE
5. End Newton-Raphson iterations

Figure 35 & *Figure 37*. The iterations continue until *R* is less than the defined tolerance used to determine subsequent stress.

The wire can be represented as a yield surface on a plane of stresses, shown in Figure 33.

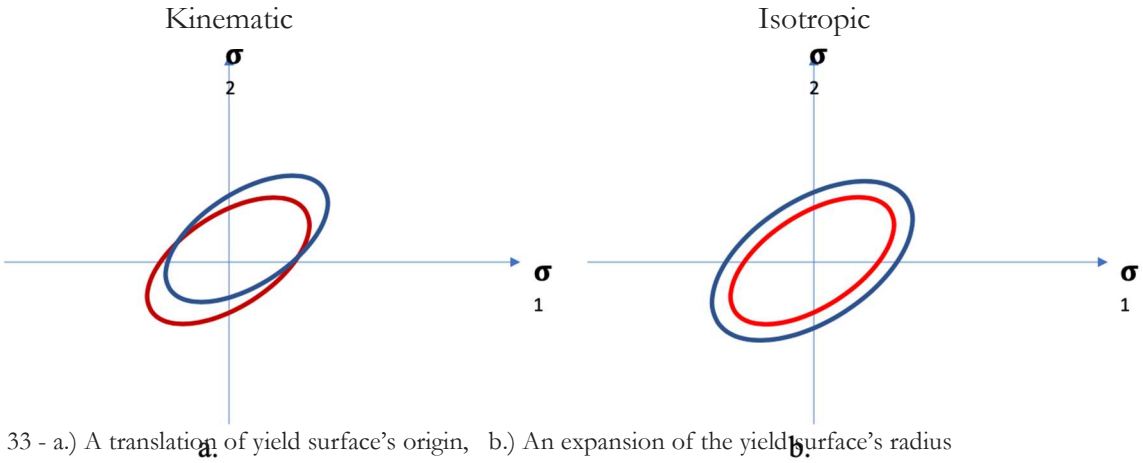

Figure 33 - a.) A translation of yield surface's origin, b.) An expansion of the yield surface's radius

We apply two models of strain hardening for this material: Isotropic and Kinematic. The Isotropic model demonstrates an increase in the yield surface's radius. However, the Kinematic hardening represents a translation of the surface's origin. Adding a variable q known as the backstress allows the algorithm to track the wire on the yield surface, thus expanding the hardening method to incorporate Kinematic hardening, as shown in Figure 36.

Ramberg–Osgood Isotropic Plastic Hardening

The Ramberg-Osgood hardening method uses the power law $K(\varepsilon_p)^n$ to describe the hardening. A method derived from the work of Louie L. Yaw (2012) is employed to determine the subsequent stress depending on the plastic and elastic strain accumulated from an incremental displacement, shown in

1. Start with stored known variables $\{\epsilon_n, \epsilon_n^p, a_n\}$
2. An increment of strain gives $\epsilon_{n+1} = \epsilon_n + \Delta\epsilon_n$.
3. Calculate the elastic trial stress, the trial value for the yield function and check for yielding.

$$\sigma_{n+1}^{trial} = E(\epsilon_{n+1} - \epsilon_n^p)$$
$$\epsilon_{n+1}^{p\,trial} = \epsilon_n^p$$
$$a_{n+1}^{trial} = a_n$$
$$f_{n+1}^{trial} = |\sigma_{n+1}^{trial}| - (\sigma_y + Ca_n^m)$$

If $f_{n+1}^{trial} \leq 0$ then the load step is elastic:

Set $\sigma_{n+1} = \sigma_{n+1}^{trial}$

Set $C_{ep} = E$

EXIT the algorithm

Else $f_{n+1}^{trial} \geq 0$ and hence the load step is elasto-plastic continue to step 4

4. Elasto-plastic step using:

$$f_{n+1}^{trial} - \Delta\gamma E - G(a_{n+1}) + G(a_n) = 0$$

Solve for $\Delta\gamma$ by using Newton-Raphson iterations:

$$\epsilon_{n+1}^p = \epsilon_n^p + \Delta\gamma sign(\sigma_{n+1}^{trial})$$
$$a_{n+1} = a_n + \Delta\gamma$$
$$C_{ep} = \frac{EmCa_{n+1}^{m-1}}{E + mCa_{n+1}^{m-1}}$$
$$\sigma_{n+1} = \sigma_n + (\Delta\epsilon_n C_{ep})$$

EXIT the algorithm

Figure 34 &

6. Set $\Delta\gamma = 0$
7. Calculate R, where $R = f_{n+1}^{trial} - \Delta\gamma E - G(a_n + \Delta\gamma) + G(a_n)$ and $G(a) = \sigma_n + Ca^m$
8. Initialize variables:

$$\text{Set } maxiter = 10$$
$$\text{Set } k = 0 \text{ (the iteration counter)}$$
$$\text{Set } tol = 10^{-5}$$
$$\text{Set } d_g = 0$$

9. WHILE $|R| > tol$ and $k < maxiter$:

$$\frac{dR}{d\Delta\gamma} = -E - mC(a_n + \Delta\gamma)^{m-1}$$
$$d_g = -\left[\frac{dR}{d\Delta\gamma}\right]^{-1} R$$
$$\text{Update } \Delta\gamma = \Delta\gamma + d_g$$
$$\text{Recalculate } R = f_{n+1}^{trial} - \Delta\gamma E - G(a_n + \Delta\gamma) + G(a_n)$$
$$\text{Update } k = k + 1$$

   END WHILE
10. End Newton-Raphson iterations

Figure 35 (Yaw). Each wire segment will have a distinct temperature based on its radial location in the strand, known from previous experimental work. Due to the both temporal and spatial non-stationarity of the temperature field, each wire will have different stiffness, work hardening coefficient (typically known as *K,* is represented as *C*) and exponent (typically known as *n,* is represented as *m*), and yield and ultimate strains at varying temperatures.

5. Start with stored known variables $\{\epsilon_n, \epsilon_n^p, a_n\}$
6. An increment of strain gives $\epsilon_{n+1} = \epsilon_n + \Delta\epsilon_n$.
7. Calculate the elastic trial stress, the trial value for the yield function and check for yielding.

$$\sigma_{n+1}^{trial} = E\left(\epsilon_{n+1} - \epsilon_n^p\right)$$
$$\epsilon_{n+1}^{p\,trial} = \epsilon_n^p$$
$$a_{n+1}^{trial} = a_n$$
$$f_{n+1}^{trial} = \left|\sigma_{n+1}^{trial}\right| - \left(\sigma_y + C a_n^m\right)$$

If $f_{n+1}^{trial} \leq 0$ then the load step is elastic:

Set $\sigma_{n+1} = \sigma_{n+1}^{trial}$

Set $C_{ep} = E$

EXIT the algorithm

Else $f_{n+1}^{trial} \geq 0$ and hence the load step is elasto-plastic continue to step 4

8. Elasto-plastic step using:

$$f_{n+1}^{trial} - \Delta\gamma E - G(a_{n+1}) + G(a_n) = 0$$

Solve for $\Delta\gamma$ by using Newton-Raphson iterations:

$$\epsilon_{n+1}^p = \epsilon_n^p + \Delta\gamma sign\left(\sigma_{n+1}^{trial}\right)$$
$$a_{n+1} = a_n + \Delta\gamma$$
$$C_{ep} = \frac{EmCa_{n+1}^{m-1}}{E + mCa_{n+1}^{m-1}}$$
$$\sigma_{n+1} = \sigma_n + \left(\Delta\epsilon_n C_{ep}\right)$$

EXIT the algorithm

Figure 34: The Isotropic Hardening framework and iteration method to find the elastic-plastic modulus C_{ep} from the Youngs Modulus E, current strain ε_n, plastic strain ε_n^p, equivalent plastic strain α (Yaw)

To determine the location of the yield surface a function *f* is defined from the trial stress and a hardening function $G(\alpha)$. The plastic hardening function $G(\alpha)$ is formulated from the previous stress, the work hardening coefficient & exponent, and the equivalent plastic stress $\alpha(\gamma)$.

11. Set $\Delta\gamma = 0$
12. Calculate R, where $R = f_{n+1}^{trial} - \Delta\gamma E - G(a_n + \Delta\gamma) + G(a_n)$ and $G(a) = \sigma_n + Ca^m$
13. Initialize variables:

Set $maxiter = 10$

Set $k = 0$ (the iteration counter)

Set $tol = 10^{-5}$

Set $d_g = 0$

14. WHILE $|R| > tol$ and $k < maxiter$:

$$\frac{dR}{d\Delta\gamma} = -E - mC(a_n + \Delta\gamma)^{m-1}$$

$$d_g = -\left[\frac{dR}{d\Delta\gamma}\right]^{-1} R$$

Update $\Delta\gamma = \Delta\gamma + d_g$

Recalculate $R = f_{n+1}^{trial} - \Delta\gamma E - G(a_n + \Delta\gamma) + G(a_n)$

Update $k = k + 1$

END WHILE

15. End Newton-Raphson iterations

Figure 35: The Isotropic framework and Newton-Raphson Method to find the consistency parameter $\Delta\gamma$ that accounts for plastic adjustment derived from the yield surface function f, Youngs Modulus E, equivalent plastic strain α, current stress σ_n, work hardening coefficient and exponent C & m (Yaw)

Ramberg–Osgood Isotropic & Kinematic Plastic Hardening

Adding the variable *q* (known as the backstress) allows the algorithm to track the wire on the yield surface, thus expanding the hardening method to incorporate kinematic hardening, shown in

1. Start with stored known variables $\{\epsilon_n, \epsilon_n^p, a_n, q_n\}$
2. An increment of strain gives $\epsilon_{n+1} = \epsilon_n + \Delta\epsilon_n$.
3. Calculate the elastic trial stress, the trial value for the yield function and check for yielding.

$$\sigma_{n+1}^{trial} = E\left(\epsilon_{n+1} - \epsilon_n^p\right)$$
$$\epsilon_{n+1}^{p\,trial} = \epsilon_n^p$$
$$a_{n+1}^{trial} = a_n$$
$$\xi_{n+1}^{trial} = \sigma_{n+1}^{trial} - q_n$$
$$f_{n+1}^{trial} = \left|\xi_{n+1}^{trial}\right| - \left(\sigma_y + C a_n^m\right)$$

If $f_{n+1}^{trial} \leq 0$ then the load step is elastic:

Set $\sigma_{n+1} = \sigma_{n+1}^{trial}$

Set $C_{ep} = E$

EXIT the algorithm

Else $f_{n+1}^{trial} \geq 0$ and hence the load step is elasto-plastic continue to step 4

4. Elasto-plastic step using:

$$f_{n+1}^{trial} - \Delta\gamma(E + H) - G(a_{n+1}) + G(a_n) = 0$$

Solve for $\Delta\gamma$ by using Newton-Raphson iterations:

$$\epsilon_{n+1}^p = \epsilon_n^p + \Delta\gamma sign\left(\xi_{n+1}^{trial}\right)$$
$$q_{n+1} = q_n + \Delta\gamma H sign\left(\xi_{n+1}^{trial}\right)$$
$$a_{n+1} = a_n + \Delta\gamma$$

$$C_{ep} = \frac{E(H + mCa_{n+1}^{m-1})}{E + H + mCa_{n+1}^{m-1}}$$
$$\sigma_{n+1} = \sigma_n + \left(\Delta\epsilon_n C_{ep}\right)$$

EXIT the algorithm

Figure 36 *& Figure 37* (Yaw). The backstress is derived from the consistency parameter and the Plastic Moduli, *H*. The Plastic Modulus is related to the work hardening coefficient and the Young's Modulus of a material shown in (Kelly).

$$\frac{1}{K} = \frac{1}{E} + \frac{1}{H} \qquad (1)$$

5. Start with stored known variables $\{\epsilon_n, \epsilon_n^p, a_n, q_n\}$
6. An increment of strain gives $\epsilon_{n+1} = \epsilon_n + \Delta\epsilon_n$.
7. Calculate the elastic trial stress, the trial value for the yield function and check for yielding.

$$\sigma_{n+1}^{trial} = E\left(\epsilon_{n+1} - \epsilon_n^p\right)$$
$$\epsilon_{n+1}^{p\,trial} = \epsilon_n^p$$
$$a_{n+1}^{trial} = a_n$$
$$\xi_{n+1}^{trial} = \sigma_{n+1}^{trial} - q_n$$
$$f_{n+1}^{trial} = \left|\xi_{n+1}^{trial}\right| - \left(\sigma_y + Ca_n^m\right)$$

If $f_{n+1}^{trial} \leq 0$ then the load step is elastic:

Set $\sigma_{n+1} = \sigma_{n+1}^{trial}$

Set $C_{ep} = E$

EXIT the algorithm

Else $f_{n+1}^{trial} \geq 0$ and hence the load step is elasto-plastic continue to step 4

8. Elasto-plastic step using:

$$f_{n+1}^{trial} - \Delta\gamma(E + H) - G(a_{n+1}) + G(a_n) = 0$$

Solve for $\Delta\gamma$ by using Newton-Raphson iterations:

$$\epsilon_{n+1}^p = \epsilon_n^p + \Delta\gamma sign\left(\xi_{n+1}^{trial}\right)$$
$$q_{n+1} = q_n + \Delta\gamma H sign\left(\xi_{n+1}^{trial}\right)$$
$$a_{n+1} = a_n + \Delta\gamma$$

$$C_{ep} = \frac{E(H + mCa_{n+1}^{m-1})}{E + H + mCa_{n+1}^{m-1}}$$
$$\sigma_{n+1} = \sigma_n + \left(\Delta\epsilon_n C_{ep}\right)$$

EXIT the algorithm

Figure 36: The Isotropic & Kinematic framework and iteration method to find the elastic-plastic modulus C_{ep} from the Youngs Modulus E, current strain ε_n, plastic strain ε_n^p, equivalent plastic strain α, backstress q, Plastic Modulus H (Yaw)

The Elastic-Plastic Modulus, C_{ep} is computed similarly to the method of isotropic hardening, shown in

9. Start with stored known variables $\{\epsilon_n, \epsilon_n^p, a_n\}$
10. An increment of strain gives $\epsilon_{n+1} = \epsilon_n + \Delta\epsilon_n$.
11. Calculate the elastic trial stress, the trial value for the yield function and check for yielding.

$$\sigma_{n+1}^{trial} = E\left(\epsilon_{n+1} - \epsilon_n^p\right)$$
$$\epsilon_{n+1}^{p\,trial} = \epsilon_n^p$$
$$a_{n+1}^{trial} = a_n$$
$$f_{n+1}^{trial} = \left|\sigma_{n+1}^{trial}\right| - \left(\sigma_y + C a_n^m\right)$$

If $f_{n+1}^{trial} \leq 0$ then the load step is elastic:

Set $\sigma_{n+1} = \sigma_{n+1}^{trial}$

Set $C_{ep} = E$

EXIT the algorithm

Else $f_{n+1}^{trial} \geq 0$ and hence the load step is elasto-plastic continue to step 4

12. Elasto-plastic step using:

$$f_{n+1}^{trial} - \Delta\gamma E - G(a_{n+1}) + G(a_n) = 0$$

Solve for $\Delta\gamma$ by using Newton-Raphson iterations:

$$\epsilon_{n+1}^p = \epsilon_n^p + \Delta\gamma sign\left(\sigma_{n+1}^{trial}\right)$$
$$a_{n+1} = a_n + \Delta\gamma$$
$$C_{ep} = \frac{EmCa_{n+1}^{m-1}}{E + mCa_{n+1}^{m-1}}$$
$$\sigma_{n+1} = \sigma_n + \left(\Delta\epsilon_n C_{ep}\right)$$

EXIT the algorithm

Figure 34, with the incorporation of *H*. The algorithm uses the Elastic-Plastic Modulus and the strain

increment to determine the subsequent stress, as shown in

9. Start with stored known variables $\{\epsilon_n, \epsilon_n^p, a_n, q_n\}$
10. An increment of strain gives $\epsilon_{n+1} = \epsilon_n + \Delta\epsilon_n$.
11. Calculate the elastic trial stress, the trial value for the yield function and check for yielding.

$$\sigma_{n+1}^{trial} = E\left(\epsilon_{n+1} - \epsilon_n^p\right)$$
$$\epsilon_{n+1}^{p\,trial} = \epsilon_n^p$$
$$a_{n+1}^{trial} = a_n$$
$$\xi_{n+1}^{trial} = \sigma_{n+1}^{trial} - q_n$$
$$f_{n+1}^{trial} = \left|\xi_{n+1}^{trial}\right| - \left(\sigma_y + C a_n^m\right)$$

If $f_{n+1}^{trial} \leq 0$ then the load step is elastic:

Set $\sigma_{n+1} = \sigma_{n+1}^{trial}$

Set $C_{ep} = E$

EXIT the algorithm

Else $f_{n+1}^{trial} \geq 0$ and hence the load step is elasto-plastic continue to step 4

12. Elasto-plastic step using:

$$f_{n+1}^{trial} - \Delta\gamma(E + H) - G(a_{n+1}) + G(a_n) = 0$$

Solve for $\Delta\gamma$ by using Newton-Raphson iterations:

$$\epsilon_{n+1}^p = \epsilon_n^p + \Delta\gamma sign\left(\xi_{n+1}^{trial}\right)$$
$$q_{n+1} = q_n + \Delta\gamma H sign\left(\xi_{n+1}^{trial}\right)$$
$$a_{n+1} = a_n + \Delta\gamma$$

$$C_{ep} = \frac{E(H + mCa_{n+1}^{m-1})}{E + H + mCa_{n+1}^{m-1}}$$
$$\sigma_{n+1} = \sigma_n + \left(\Delta\epsilon_n C_{ep}\right)$$

EXIT the algorithm

Figure 36.

1. Set $\Delta\gamma = 0$
2. Calculate R, where $R = f_{n+1}^{trial} - \Delta\gamma(E + H) - G(a_n + \Delta\gamma) + G(a_n)$ and $G(a) = \sigma_n + Ca^m$
3. Initialize variables:

Set $maxiter = 10$

Set $k = 0$ (the iteration counter)

Set $tol = 10^{-5}$

Set $d_g = 0$

4. WHILE $|R| > tol$ and $k < maxiter$:

$$\frac{dR}{d\Delta\gamma} = -(E + H) - mC(a_n + \Delta\gamma)^{m-1}$$

$$d_g = -\left[\frac{dR}{d\Delta\gamma}\right]^{-1} R$$

Update $\Delta\gamma = \Delta\gamma + d_g$

Recalculate $R = f_{n+1}^{trial} - \Delta\gamma(E + H) - G(a_n + \Delta\gamma) + G(a_n)$

Update $k = k + 1$

END WHILE

5. End Newton-Raphson iterations

Figure 37: The Isotropic & Kinematic framework and Newton-Raphson Method to find the consistency parameter $\Delta\gamma$ that accounts for plastic adjustment derived from the yield surface function f, Youngs Modulus E, Plastic Modulus H, equivalent plastic strain α, current stress σ_n, work hardening coefficient and exponent C & m (Yaw)

Single-Wire Deformation

Code Structure

The code structure of the single-wire model is shown in

Figure 38. With a single wire, the algorithm is given a length *L*, temperature *T*, an incremental length *dL*, the maximum length L_{max} (the inputted final desired length of the specimen), and the cross-sectional area A. The initial stress, strain, backstress, and equivalent plastic stress are set to zero. The incremental change in strain $\Delta\varepsilon$ is calculated from the incremental and original lengths. The ultimate strain, yield strain, work hardening coefficient and exponent are determined in a separate function file Temp dependent Vari derived from Jumari Robinson's previous work. A *while loop* is set to run as long as the current strain is less than the ultimate strain or maximum strain $\left(\frac{L_{max} - L}{L}\right)$. A trial point is set as shown in *Figure 32* and the function *f* is defined to determine the location on the yield surface.

If $f_{TR} \leq 0$ then the wire is still in the elastic region and is incremented at the rate of the Young's Modulus. However, if $f_{TR} > 0$ then the wire is in the elastic-plastic region and strain hardening can occur. Depending on whether the user wants to run an Isotropic hardening or Isotropic & Kinematic hardening model, the Elastic-Plastic Modulus C_{ep} is calculated by the procedures shown in

13. Start with stored known variables $\{\epsilon_n, \epsilon_n^p, a_n\}$
14. An increment of strain gives $\epsilon_{n+1} = \epsilon_n + \Delta\epsilon_n$.
15. Calculate the elastic trial stress, the trial value for the yield function and check for yielding.

$$\sigma_{n+1}^{trial} = E\left(\epsilon_{n+1} - \epsilon_n^p\right)$$
$$\epsilon_{n+1}^{p\,trial} = \epsilon_n^p$$
$$a_{n+1}^{trial} = a_n$$
$$f_{n+1}^{trial} = \left|\sigma_{n+1}^{trial}\right| - \left(\sigma_y + C a_n^m\right)$$

If $f_{n+1}^{trial} \leq 0$ then the load step is elastic:

Set $\sigma_{n+1} = \sigma_{n+1}^{trial}$

Set $C_{ep} = E$

EXIT the algorithm

Else $f_{n+1}^{trial} \geq 0$ and hence the load step is elasto-plastic continue to step 4

16. Elasto-plastic step using:

$$f_{n+1}^{trial} - \Delta\gamma E - G(a_{n+1}) + G(a_n) = 0$$

Solve for $\Delta\gamma$ by using Newton-Raphson iterations:

$$\epsilon_{n+1}^p = \epsilon_n^p + \Delta\gamma sign\left(\sigma_{n+1}^{trial}\right)$$
$$a_{n+1} = a_n + \Delta\gamma$$
$$C_{ep} = \frac{EmCa_{n+1}^{m-1}}{E + mCa_{n+1}^{m-1}}$$
$$\sigma_{n+1} = \sigma_n + \left(\Delta\epsilon_n C_{ep}\right)$$

EXIT the algorithm

13. Start with stored known variables $\{\epsilon_n, \epsilon_n^p, a_n, q_n\}$
14. An increment of strain gives $\epsilon_{n+1} = \epsilon_n + \Delta\epsilon_n$.
15. Calculate the elastic trial stress, the trial value for the yield function and check for yielding.

$$\sigma_{n+1}^{trial} = E\left(\epsilon_{n+1} - \epsilon_n^p\right)$$
$$\epsilon_{n+1}^{p\,trial} = \epsilon_n^p$$
$$a_{n+1}^{trial} = a_n$$
$$\xi_{n+1}^{trial} = \sigma_{n+1}^{trial} - q_n$$
$$f_{n+1}^{trial} = \left|\xi_{n+1}^{trial}\right| - \left(\sigma_y + C a_n^m\right)$$

If $f_{n+1}^{trial} \leq 0$ then the load step is elastic:

Set $\sigma_{n+1} = \sigma_{n+1}^{trial}$

Set $C_{ep} = E$

EXIT the algorithm

Else $f_{n+1}^{trial} \geq 0$ and hence the load step is elasto-plastic continue to step 4

16. Elasto-plastic step using:

$$f_{n+1}^{trial} - \Delta\gamma(E + H) - G(a_{n+1}) + G(a_n) = 0$$

Solve for $\Delta\gamma$ by using Newton-Raphson iterations:

$$\epsilon_{n+1}^p = \epsilon_n^p + \Delta\gamma sign\left(\xi_{n+1}^{trial}\right)$$
$$q_{n+1} = q_n + \Delta\gamma H sign\left(\xi_{n+1}^{trial}\right)$$
$$a_{n+1} = a_n + \Delta\gamma$$

$$C_{ep} = \frac{E(H + mCa_{n+1}^{m-1})}{E + H + mCa_{n+1}^{m-1}}$$
$$\sigma_{n+1} = \sigma_n + \left(\Delta\epsilon_n C_{ep}\right)$$

EXIT the algorithm

Figure 36. The subsequent stress is obtained using C_{ep} and the current stress.

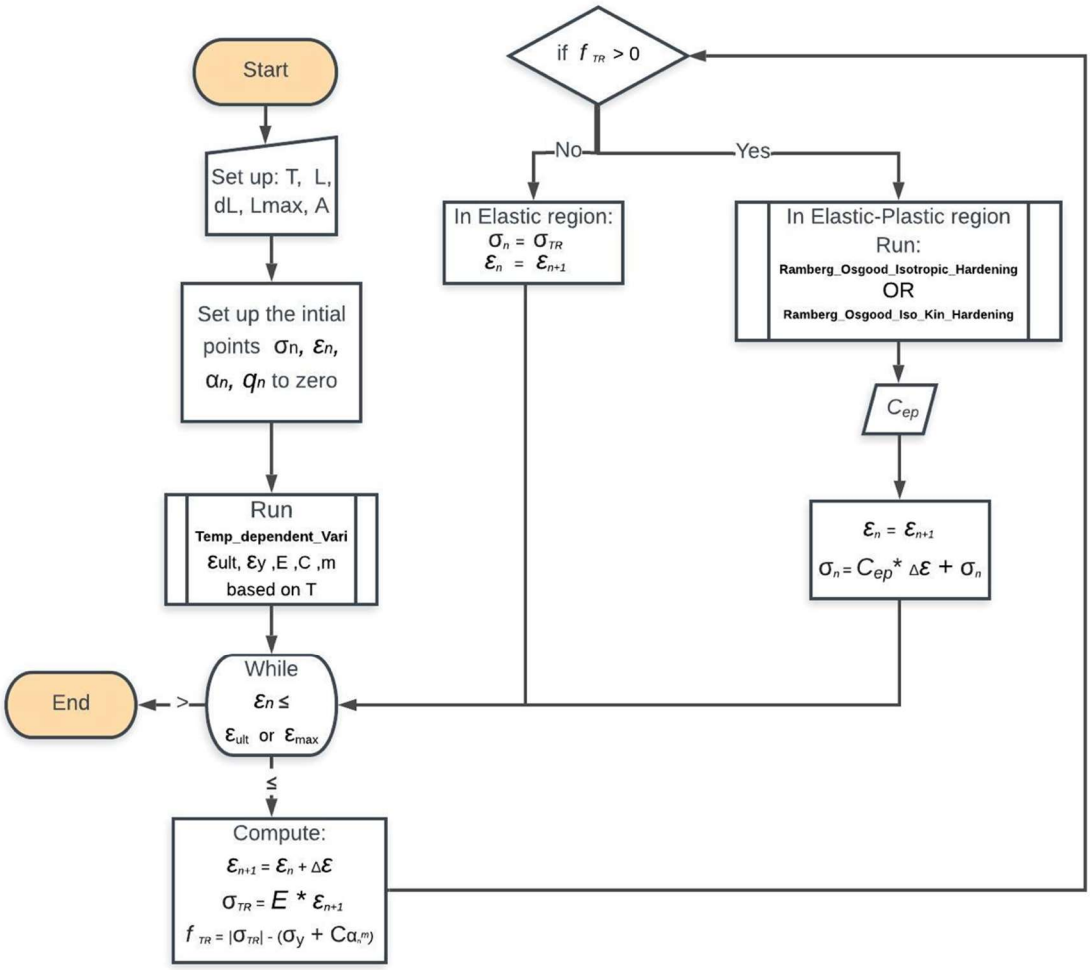

Figure 38: An organizational flow chart of the Single-Wire model base code for the algorithm

An *IF* statement is implemented to the base code so if the user wants to run it using an elastic-perfectly plastic method, the current stress will be held constant at the yield stress until the ultimate strain is reached. Additionally, an optional unload/reload sequence is added to the base code. Therefore, when the current strain has reached a designated percentage of the maximum or ultimate strain the wire will unload and then reload elastically.

Results

At 532°C, yield occurs at 58 ksi, at which point the strain hardening starts. The results for the Elastic-Perfectly Plastic, Isotropic, Isotropic & Kinematic plastic hardening methods is shown in *Figure 39* , *Figure 40,* & *Figure 41.* The Isotropic & Kinematic plastic hardening is shown to have greater stress as it reaches the ultimate strain than the Isotropic plastic hardening method.

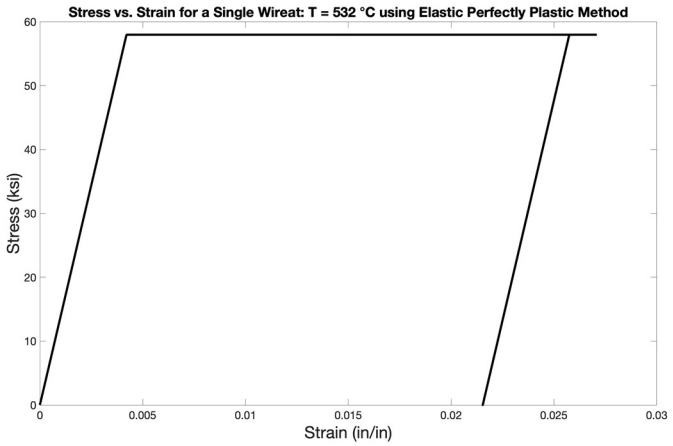

Figure 39: The stress strain curve under elastic-perfectly plastic conditions for a Single-Wire at 532°C

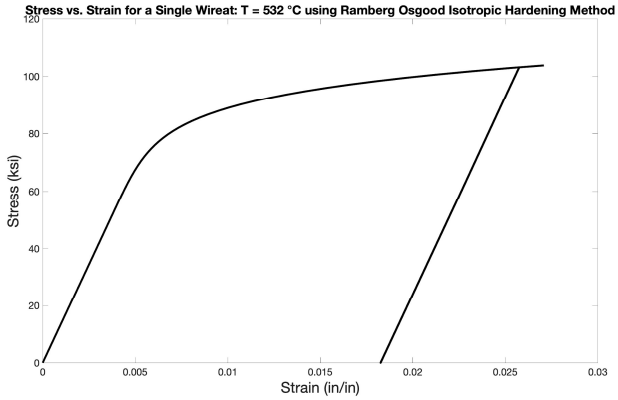

Figure 40: The stress strain curve under Isotropic plastic hardening for a single wire at 532°C

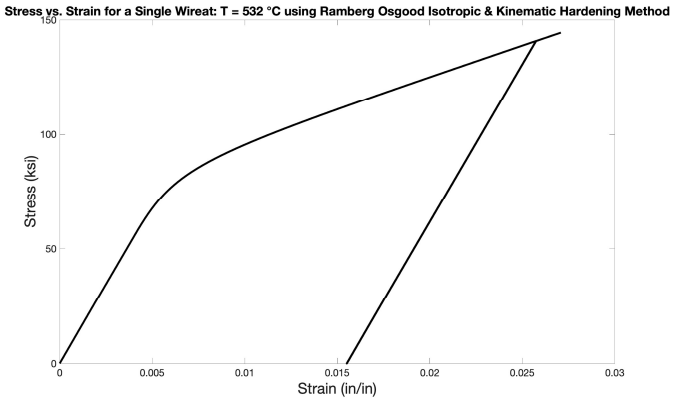

Figure 41: The stress strain curve under Isotropic & Kinematic plastic hardening for a single wire at 532°C

Analysis

A plot of the residuals for the Newton-Raphson iteration method (used to find the consistency parameter) is shown in *Figure 42*. To find the consistency parameter the algorithm iteratively computes

the residuals *R* for a given strain increment. Residuals are comprised of the root sum squared of the current *R* function.

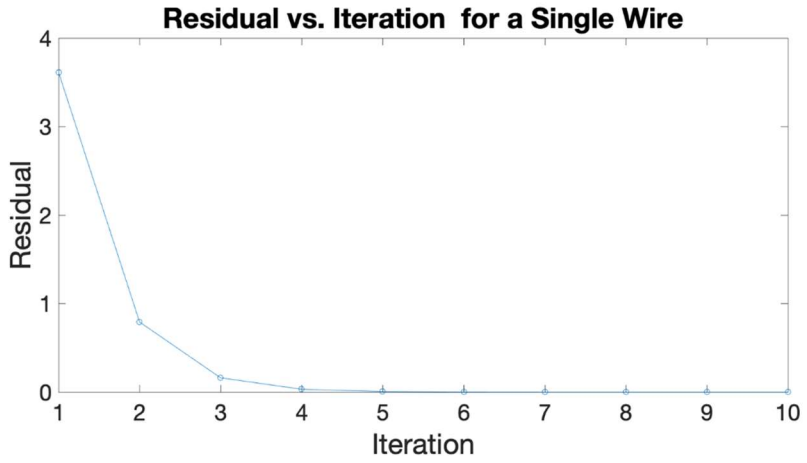

Figure 42: Represents the residuals for a specific strain increment that determines the value of the consistency parameter which the algorithm yields a convergence to a solution approximately at the 5th iteration

The Isotropic hardening model illustrates a wire experiencing plastic deformation regulated by only the Ramberg Osgood power law relationship. The Isotropic & Kinematic hardening model's incorporation of the backstress yields a drastic relationship between an acquisition in strength to a reduction in ductility. The comparison for the deformation models is shown in *Figure 43*.

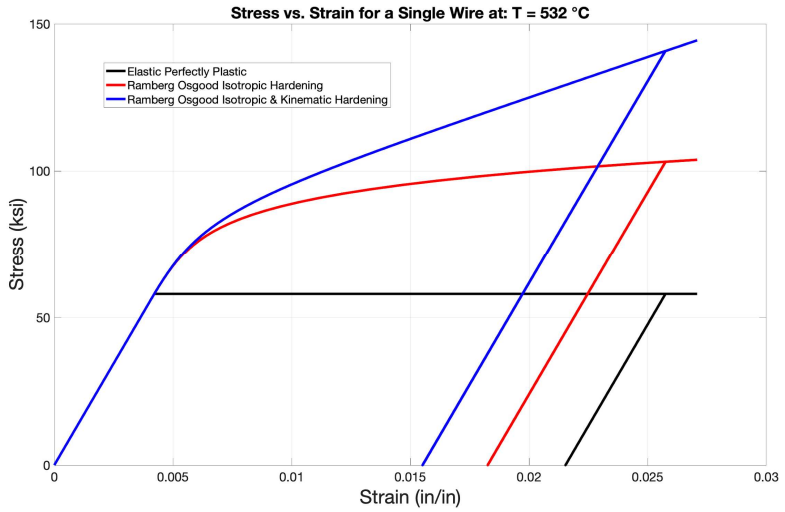

Figure 43: Comparison of the Elastic-Perfectly Plastic, Isotropic, Isotropic & Kinematic hardening models for a Single-Wire at 532°C

61-Wire Cable Deformation

The multi-wire model of the heated section of a cable can be described as parallel springs with temperature-dependent elastoplastic properties as shown in Figure 30. Each wire will have a distinct temperature based on its radial location in the strand, known from previous experimental work. This model is a decoupled system, such that the wires are in parallel and the displacement information is provided. Therefore, a *FOR* Loop can sum the wire's resulting internal forces for a specific strain increment.

Code Structure

The code structure of the multi-wire cable model is shown in *Figure 44*.

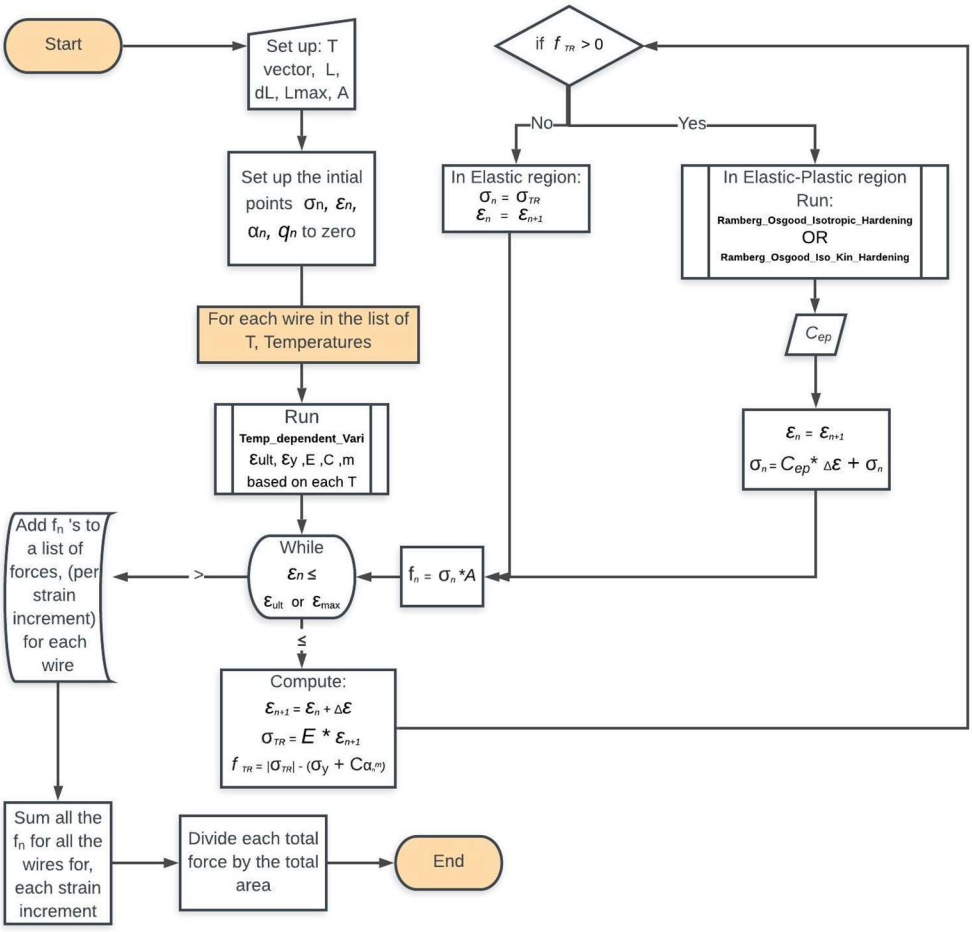

Figure 44: An organizational flow chart of the Multiple-Wire model base code for the algorithm

A model is developed to analyze multiple wires using the base code developed for a single wire. A catalog of temperatures is assigned with the same initial parameters as in

Figure 38. A separate file function Single_Wire is conveyed that includes the base code from Single Wire model (excluding the unloading sequence). Due to the decoupled nature of the system, the internal forces for each wire can be quantified. The total stress in the cable at a given strain increment is obtained by the summation of all the wires' internal forces and the division of the total area.

Results

As each wire reaches its temperature-dependent ultimate strain the global stress trends downward. The catalog of temperatures provided also represents the number of wires given in the system. A user can input any number of temperatures (wires) in the range of 22-724°C. Jumari Robinson's initial elastic-perfectly plastic work had used temperature-dependent properties from experimental data, shown in Figure 31. However, he had not provided the specific temperatures employed. To have analogous results, the temperature-dependent functions are rearranged to obtain a similar temperature index given his specified Young's Modulus range. Thus, the results below are for wires in the temperature range of 550-587°C. The results of the 61-wire cables are shown in *Figure 45, Figure 46,* and *Figure 47*.

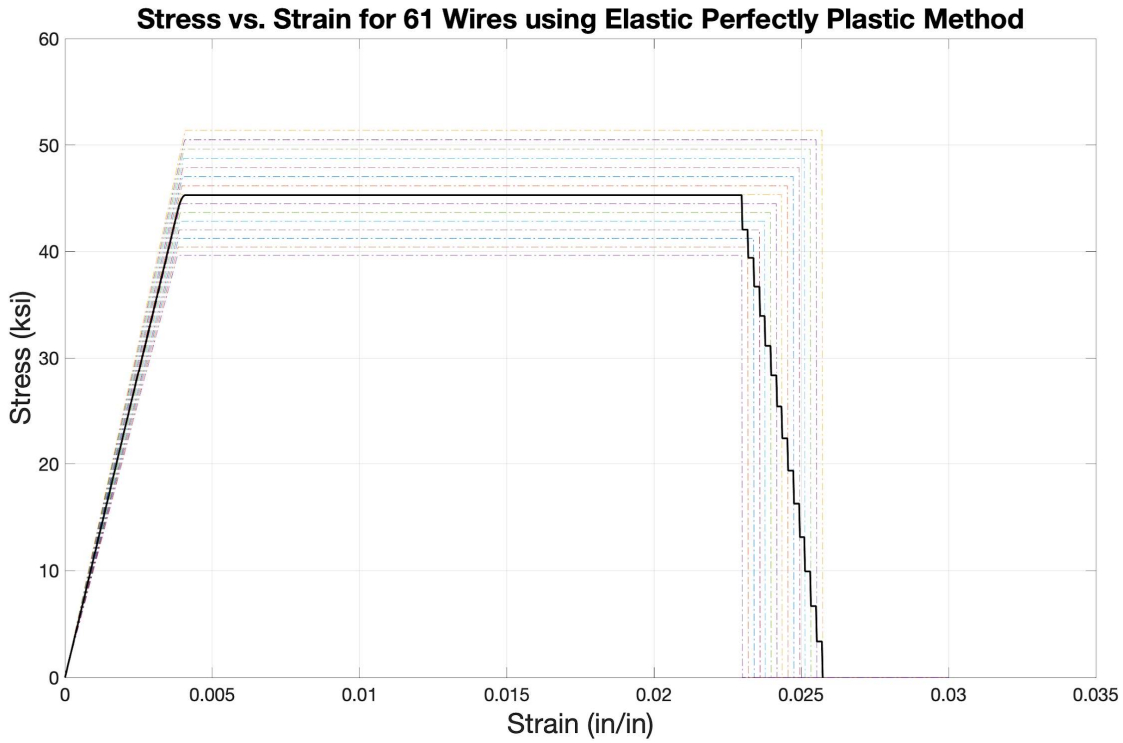

Figure 45: The stress strain curve under elastic-perfectly plastic conditions for 61-wires between 550-587°C

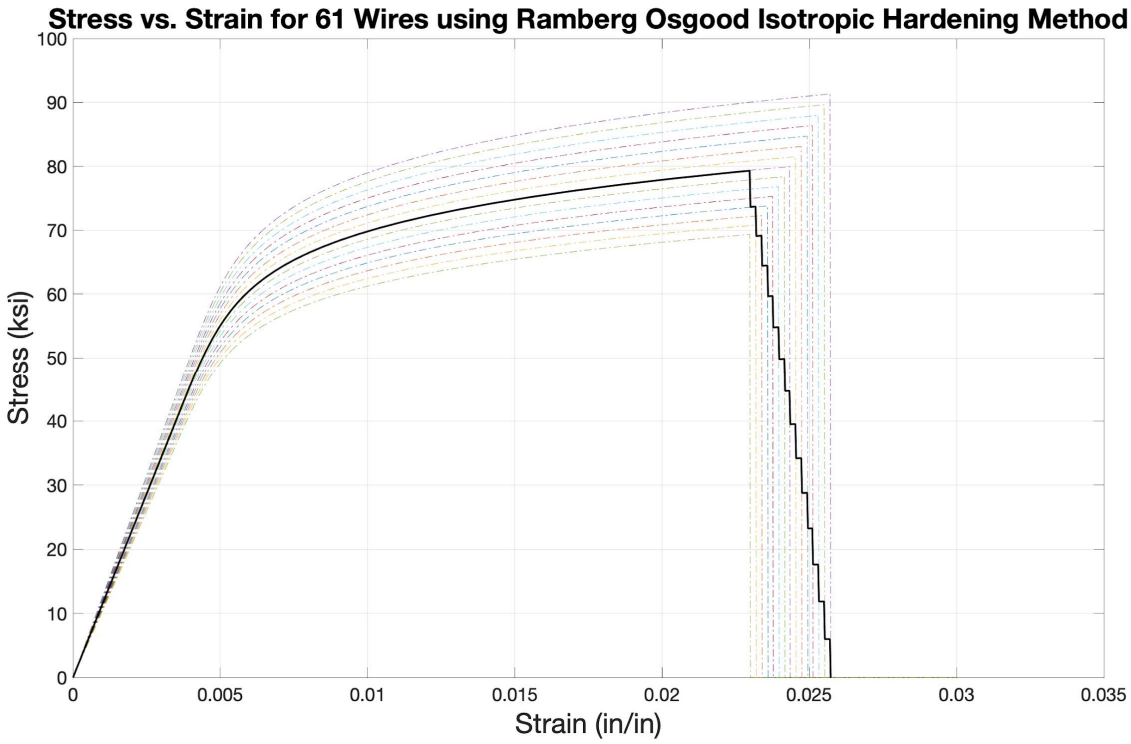

Figure 46: The stress strain curve under Isotropic plastic hardening for 61-wires between 550-587°C

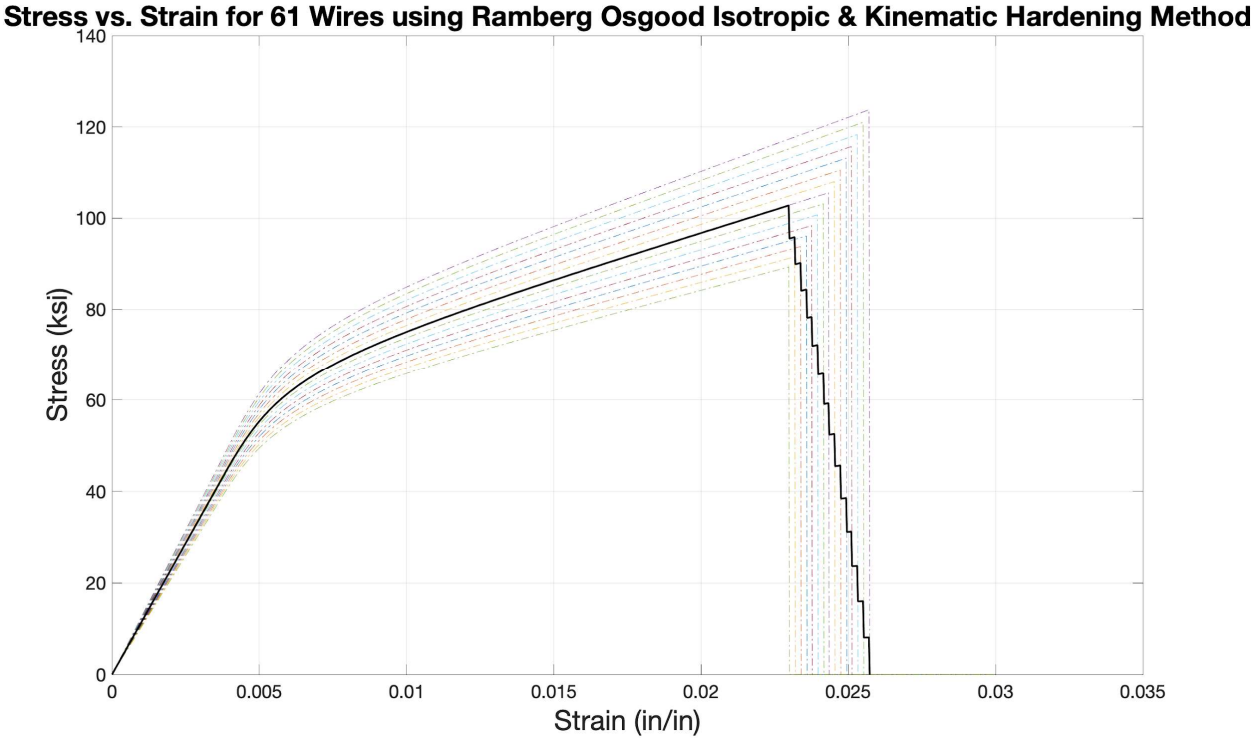

Figure 47: The stress strain curve under Isotropic & Kinematic plastic hardening for 61-wires between 550-587°C

Analysis

The multi-wire models shown in Figure 48, have a downward trend due to the varying ultimate strains. The models represent a 61-wire cable with temperatures ranging between 550-587°C. All the models yield at approximately 45 ksi at which they establish diverging trends.

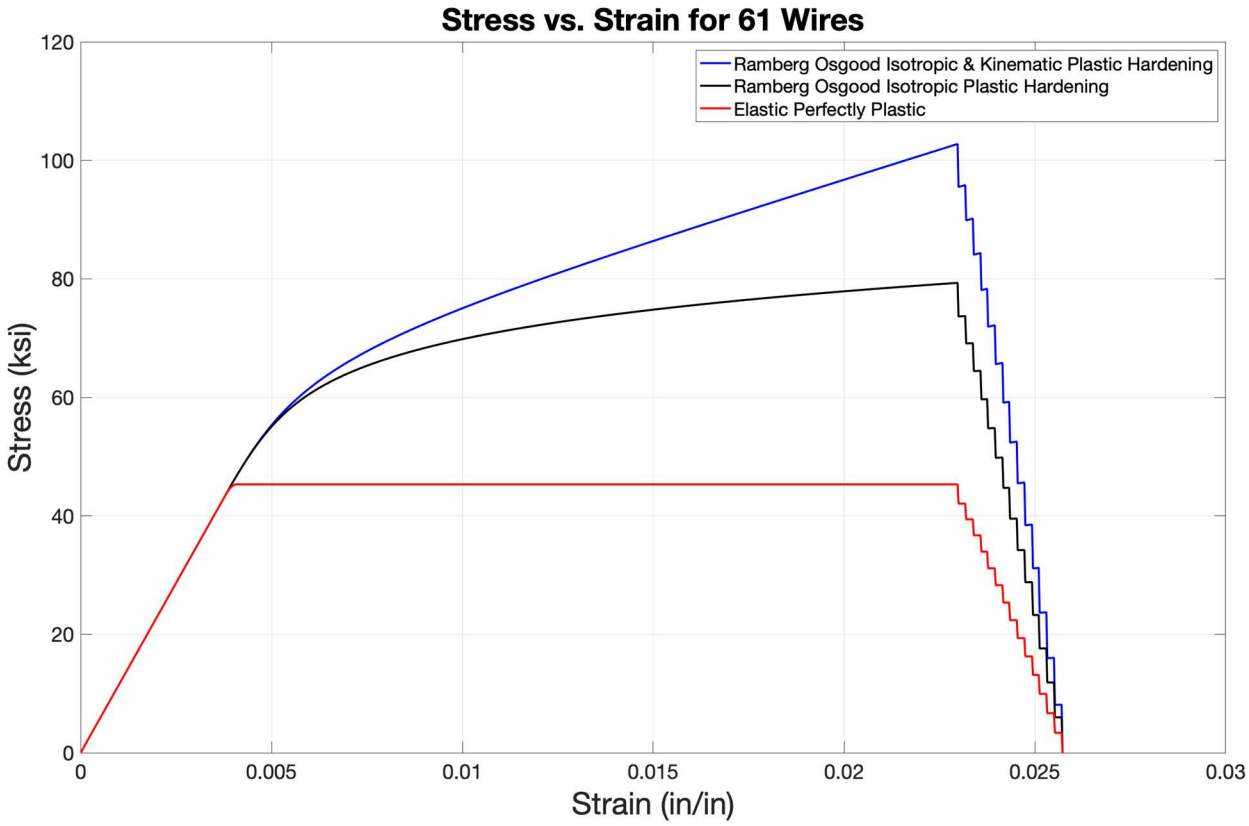

Figure 48: Comparison of the Elastic-Perfectly Plastic, Isotropic, Isotropic & Kinematic hardening models for a 61-Wire model between 550-587°C

61-Wire Cable Deformation in an Axially Expanded Domain

A model is constructed to represent a cable in an expanded axial domain (in the direction of the tensile service stress) of the strand to include load redistribution as a function of the thermomechanical evolution of the wire. This model is a coupled system, such that the wire segments are in parallel and series. The code structure of the multiple-wire expanded domain model is shown in *Figure 49*.

Code Structure

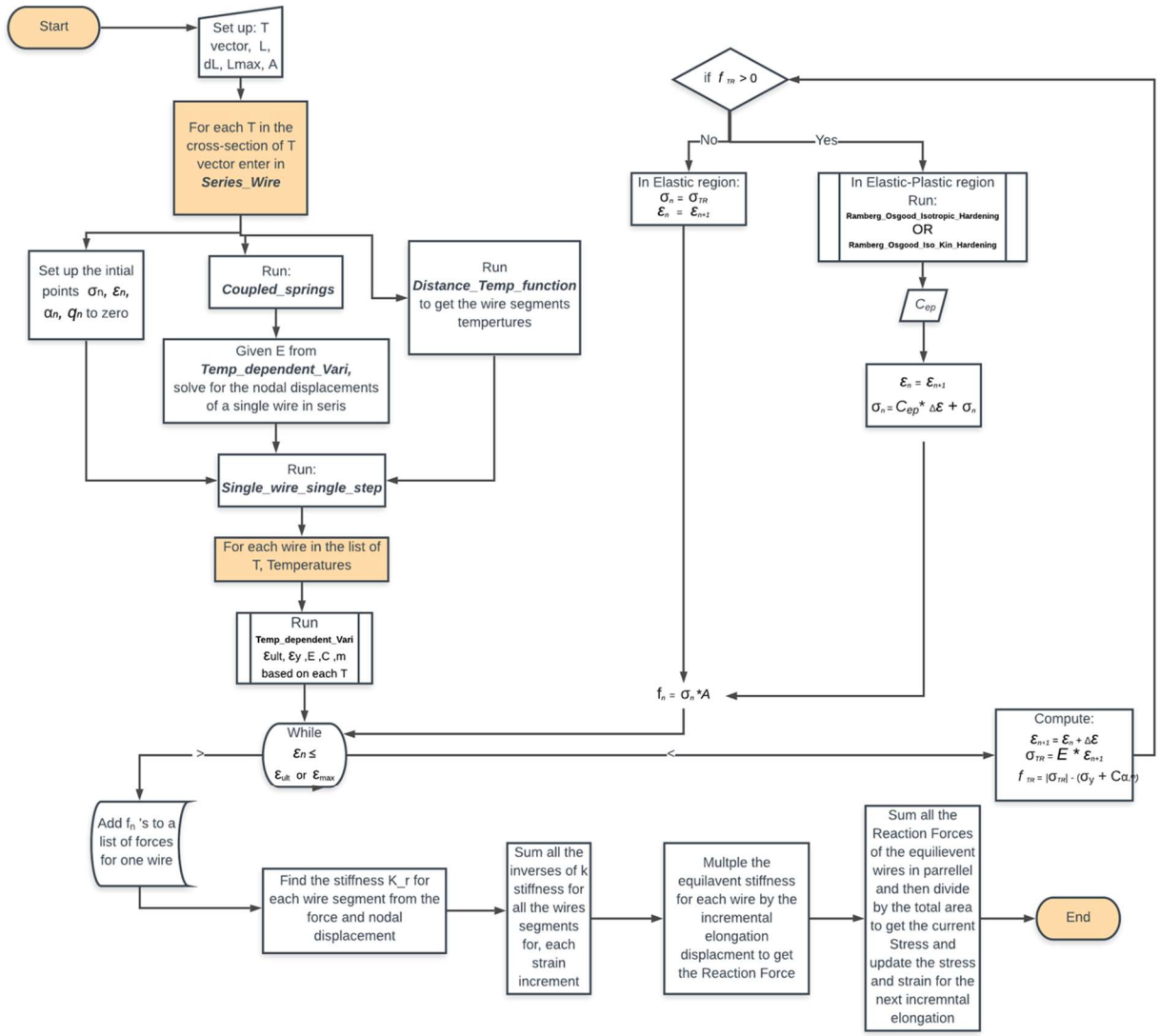

Figure 49: An organizational flow chart of the Multiple-Wire with an axially expanded domain model base code for the algorithm

The initial cross-section temperature vector is inputted, which a *FOR* loop is composed. For each wire, the file Series_Wire is operates to obtain all the wire segments' internal forces.

To obtain the temperatures for each wire segment (spring) a modifiable function is set to run (Distance_Temp_function), given the length of the cable and the initial cross-section temperature. Any function can be inputted to represent the axial temperature domain of a single wire. The model uses a simple curve distribution from a sine wave as an example, however, this does not reflect the cable's actual temperatures as a function of distance. The function can be optimized for any number

of wire segments, however due to the time-consuming complexion of the algorithm only 3 wire segments are implemented for each wire in the cable.

The initial parameter is set up from the base code of the multi-wire model. The algorithm runs a function Coupled springs to obtain the displacements of a single wire segmented in series. To obtain the stiffness of each wire segment the algorithm runs Temp dependent Vari to get each wire segment's Young's Modulus. Once all the stiffnesses are computed for the wire segments in series the global stiffness matrix is assembled. The system is defined with an initial cable elongation (u_4), thus boundary displacements are used with the initial conditions (u_1, u_2, u_3) of the wire subjected to a fixed point at the opposing boundary. A representation is shown in *Figure 50*.

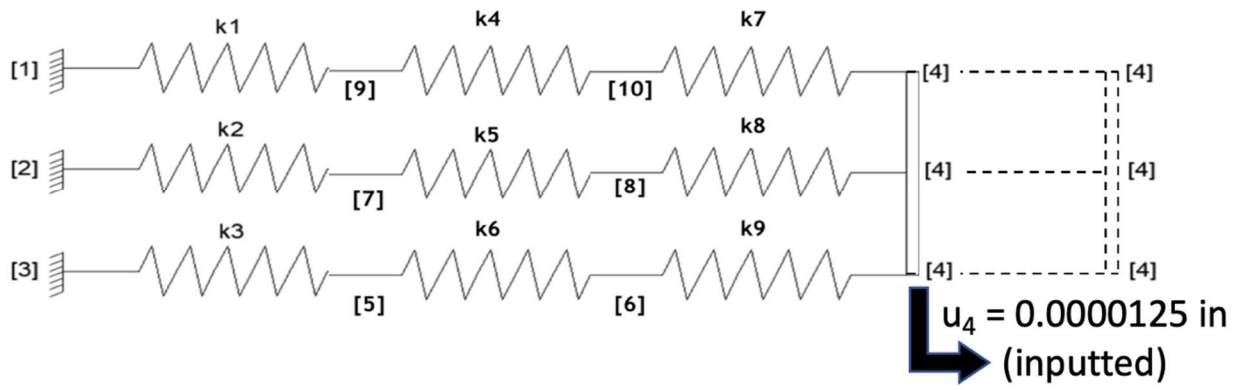

Figure 50: Representation of a cable with 3 wires, segmented into 3 section with separate temperatures and properties. The cable is displaced an incremental amount of 0.0000125in at u_4.

Using linear algebra, the algorithm solves each displacement at each node. *Figure 51* represents one wire isolated within the cable with the unknown and known displacements, as well as the resulting internal forces for each wire segment derived from the elastoplastic algorithm.

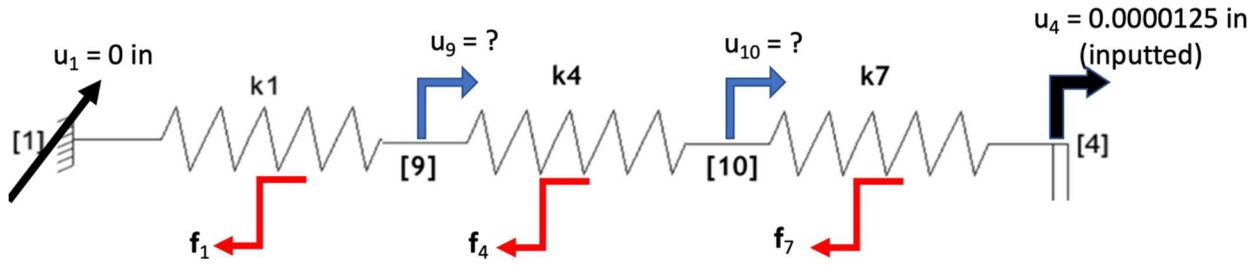

Figure 51: Represents an isolation of one wire from the cable, with a fixed end yielding no displacement, a free end with an inputted incremental displacement, and unknown displacements from each wire segment. And the resulting internal forces calculated from the elastoplastic algorithm.

The function Coupled_springs compiles the stiffness EA/L from each wire segment into a global stiffness matrix, shown in *Figure 52*. With the fixed end and the inputted global displacement, the algorithm solves for the nodal displacements u_9 and u_{10}.

$$\begin{pmatrix} k1 & -k1 & 0 & 0 \\ -k1 & k1+k4 & -k4 & 0 \\ 0 & -k4 & k4+k7 & -k7 \\ 0 & 0 & -k7 & k7 \end{pmatrix} \cdot \begin{pmatrix} u1 \\ u9 \\ u10 \\ u4 \end{pmatrix}$$

Figure 52: A sample of global stiffness matrix used to find the nodal displacements for isolated wire segments in series shown in Figure 51.

A FOR loop is set up to run for each wire in the initial cross-sectional temperature vector. Once all nodal displacements are found it runs a function Single_Wire_single_step that contains the base code from a single-wire(2D) however, for one displacement step. The function outputs the internal force for that wire segment that is added to a list of internal forces for each wire from the nodal displacements established.

A function file find_total_intern_Force is run to obtain the global stiffness of the whole axial domain of a wire. From the nodal displacements from the incremental displacement and the initial resulting elastoplastic forces from each wire segment, the global (series) stiffness is determined. The equivalent stiffness is shown in *Figure 53* as K_{147} from the isolated example of a wire segments stiffness k_1, k_4, k_7 in series from *Figure 51*.

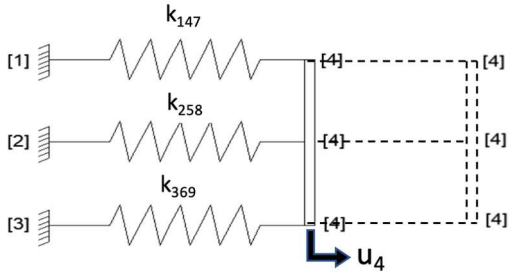

$$K_{147} = \frac{1}{\frac{u_9 - u_1}{f_1} + \frac{u_{10} - u_9}{f_4} + \frac{u_4 - u_{10}}{f_7}}$$

$$F_{\text{total Reaction}} = u_4(k_{147} + k_{258} + k_{369})$$

Figure 53: A representation of the cable with equivalent wire stiffnesses in parallel, the formula used to determine an equivalent stiffness from the isolated wire segments example in Figure 30. And the formulation of the reaction force from the global displacement and the parallel reaction forces.

The stiffness is obtained from the summation of the inverse of the wire segments computed stiffness shown in *Figure 53*. The algorithm then computes the reaction force at the fixed end from the global series stiffness and the global incremental displacement set. The reactions for each wire in the cable are summed due to the parallel presents of the system shown in *Figure 53*. The cable stress is computed from the total cable force and the total area. The global displacement is then incremented using the algorithm until the final desired length is obtained.

Results

The results for a 61-wire model with an expanded axial domain for both the Ramberg Osgood Isotropic and Isotropic & kinematic hardening methods shown in *Figure 54 & Figure 55* yields trends with less curvature compared to their respected 2D models.

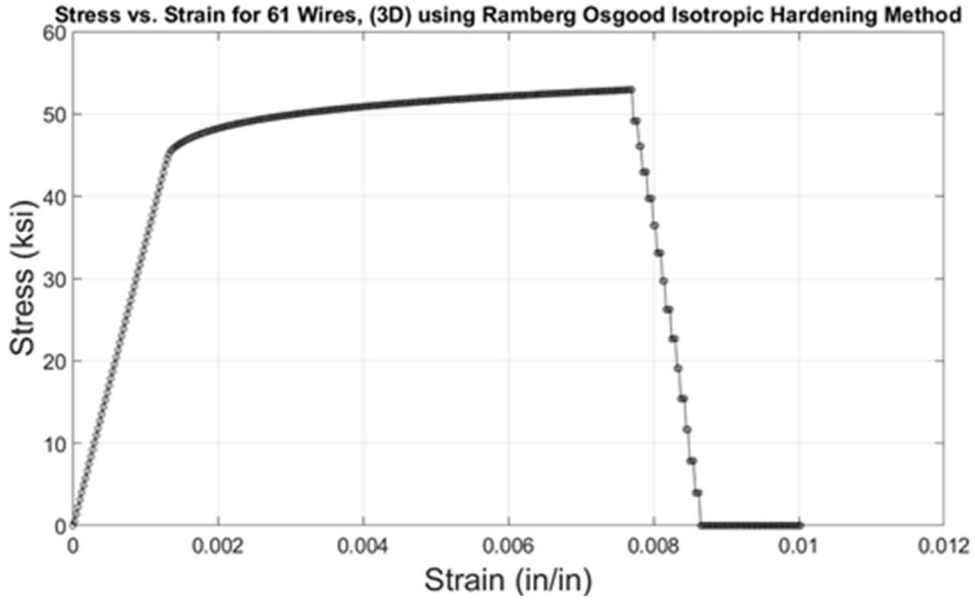

Figure 54: The stress strain curve under Isotropic plastic hardening for 61-wires in an axially expanded domain between 550-587°C

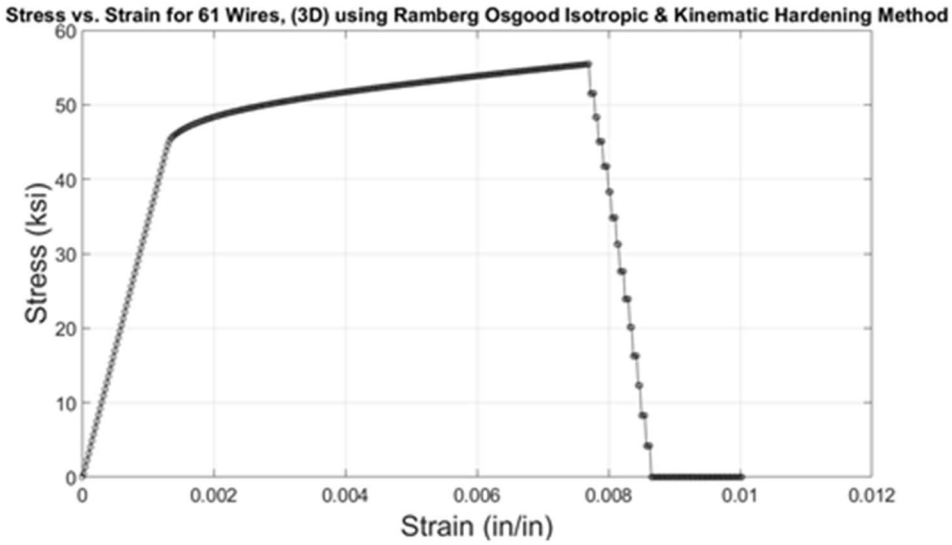

Figure 55 The stress strain curve under Isotropic & Kinematic plastic hardening for 61 wires in an axially expanded domain between 550-587°C

Analysis

The similar trends represented in the single and multi-wire models for a cross section of the cable (2D models) are seen in the axially expanded domain. *Figure 56* shows the trends for multi-wire cables in the expanded domain for 3 wires. All the hardening methods below show lower stress within the cable when the model included multi wire segments in the domain.

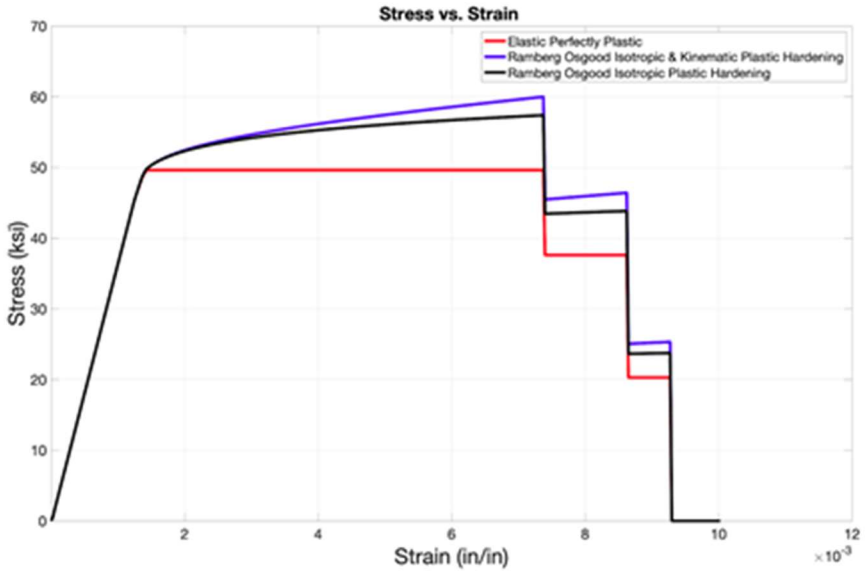

Figure 56: Comparison of the Elastic-Perfectly Plastic, Isotropic, Isotropic & Kinematic hardening models for a 3-Wire model in an axially expanded domain.

Future Work

Currently, efforts are underway to expand the model spatially to consider the coupled mechanics of a cross-section of a 61-wire strand loaded in force control, represented in *Figure 57*. We shall apply a global force to the system, in which the wires will experience local displacements. These displacements will run through the elastic-plastic algorithm (displacement-controlled), resulting in internal forces. Consequently, the forces will be used in the global stiffness matrix to compute the reactions of the system for the expanded domain from an applied force.

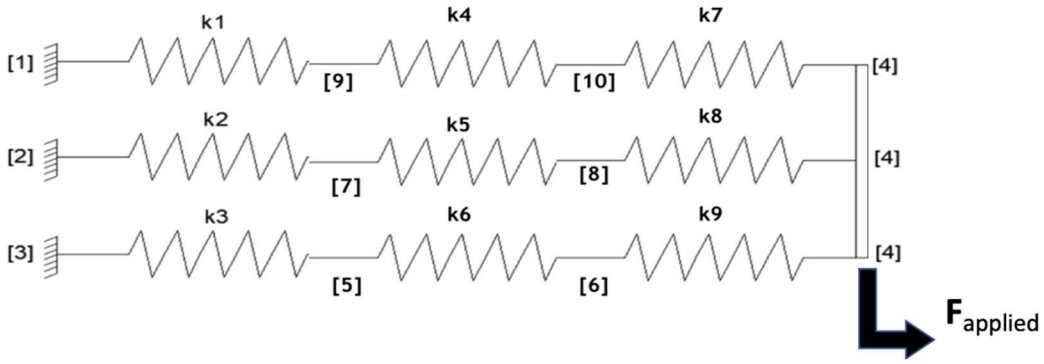

Figure 57 A representation of a multi wire cable under force control such that an applied force is initialized and governs the algorithm

Conclusion

By expanding the elastic-plastic model with the Ramberg-Osgood power relationship the algorithm can reproduce a stress-strain relationship informed and validated by experimental data. The Newton-Raphson iteration method allows for the algorithm to calculate the subsequent stress from the elastic and plastic strains accumulated. Each wire has a different mechanical characteristic derived from the cable's radial temperature distribution. Therefore, the wire's internal forces are used to calculate the cable's total stress for an incremental elongation in the cable cross-section (2D) & axially expanded domain (3D) model.

CHAPTER V: FORENSIC INVESTIGATION OF SUSPENSION BRIDGE FIRES

Julien El Naddaf, Tak Sohn

Introduction

Fire is one of the prevalent hazards to which a bridge is subjected. Based on a study done by the Texas Transportation Institute on 1,502 bridge failures, fire causes almost twice the number of bridge collapses as earthquakes do. Less extreme incidents can also cause severe damage to structural members leading to costly repairs and economical loss.

The main cables on suspension bridges are the primary load-carrying members, and typically there are no redundant systems to serve as a backup. This poses a major concern because of their proximity to the deck at mid-span and near the anchorages. One incident that underlines this point is the 2013 Little Belt Bridge fire. A truck caught fire at mid-span, causing significant damage to the main cable. Another important concern is the fact that the fire reached significant temperatures during these incidents without the presence of hydrocarbons or highly flammable material. Consequently, all types of accidents were considered, such as car collisions, wildfires (reaching bridges) and construction fires, in order to gain a quantitative and qualitative understanding of key incident parameters such as response time, fire burning time and fuel type. A large number of fires is needed to build a reliable population for analysis of the aforementioned parameters.

Methodology

To understand the type and duration of fire that suspension bridge main cables are subject to, the team decided to start with looking at bridge fire incidents happening on any type of bridge. The first database is from G. Peris-Sayol (2017), listing 154 fires that happened between 1997 and 2015, along with the bridge type, ignition source, position of the fire and level of damage.

Another database was obtained from the New York State Division of Homeland Security and Emergency Services (NYDHSES). The following incident types – from the National Fire Incident Reporting System (NFIRS) – were extracted and analyzed:

- Incident Type 112: Fire in structure, other than in a building; total of 69 cases.
- Incident Type 131: Passenger vehicle fire. Includes any motorized passenger vehicle, other than a motor home; total of 393 cases.

Media and news outlets were then scoured to find prominent examples to further explore. News reports often alluded to the possible source of the fire. With photo documentation included, it allowed photogrammetry to be conducted to determine the proximity of the fire to the cable. Additional searches with various agencies were conducted to confirm validity of incidents and diversify data regarding suspension bridges. Participation included the following: San Francisco Fire Department, Rhode Island Turnpike and Bridge Authority, and the NYDHSES.

Data Analysis

Among the 154 fires noted by G. Peris-Sayol (2017), 54 involved hydrocarbons transported by tankers, 43 were car and truck fires, and the rest were started by miscellaneous sources, such as electrical problems and wildfires.

Figure 58 depicts over fifty percent of hydrocarbon fires occurring from gasoline.

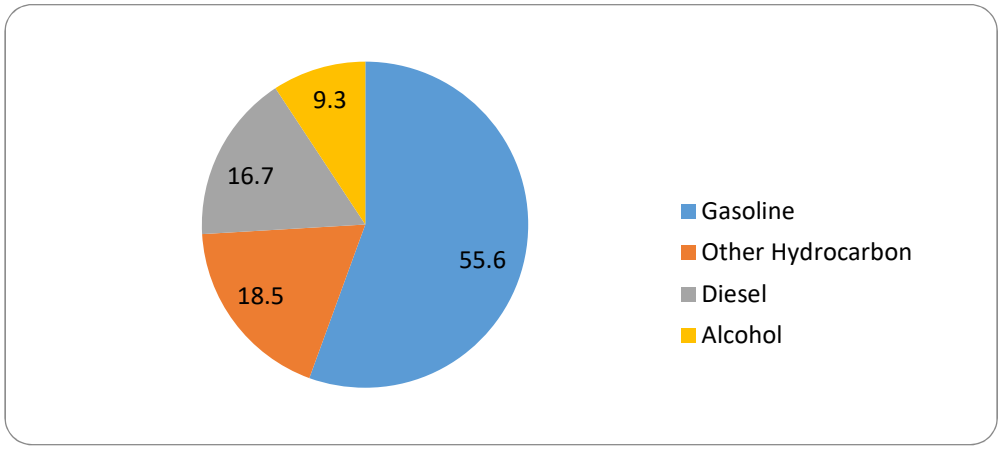

Figure 58 - Percentage of accidents (1997-2015) involving hydrocarbons.

NYDHSES provided their available database from January 2000 to June 2020. The parameters took the format of NFIRS reports, and the alarm, arrival, and site clearing times were used to learn about duration required to reach a fire (Figure 59), and the duration required to reopen the road to normal traffic (Figure 60). Since New York City is a special case in terms of traffic and urban environment, the 355 incidents happening in this area were reviewed separately. The results did not vary considerably, with an average Alarm – Arrival Duration of 5.99 minutes (standard deviation of 2.40 minutes) and average Arrival – Clearance Duration of 32.83 minutes (standard deviation of 30.08 minutes). The Arrival – Clearance duration can be useful to know the closure duration of the bridge, which helps understand the economic loss associated with closing roads. The community that uses

the bridges will also lose potential paid working hours in traffic. In cities like New York, the average hourly wage is $28.33 in 2016 according to New York State Department of Labor. In order to picture the size of the community affected, the peak traffic volumes of some of New York City's suspension bridges are shown below, as reported in the New York City Bridge Traffic Control for 2016.

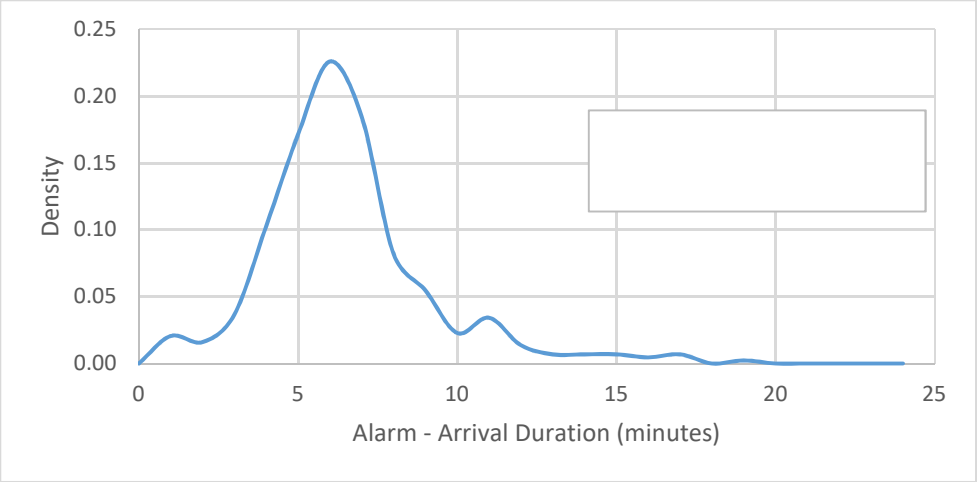

Figure 59 - Distribution of incidents with respect to Alarm – Arrival duration.

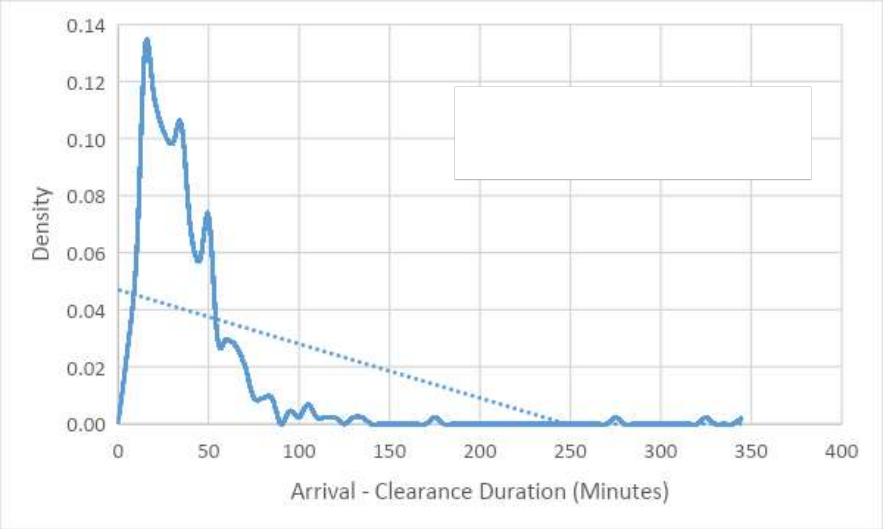

Figure 60 - Distribution of incidents with respect to Arrival – Clearance duration.

Bridge	East Bound Peak Volume	West Bound Peak Volume
Verrazano-Narrows Bridge	10,078 (8-9 AM)	8,175 (4-5 PM)
George Washington Bridge	11,474 (6-7 AM)	10,864 (5-6 PM)
Brooklyn Bridge	2,968 (9-10 PM)	3,439 (8-9 AM)
Manhattan Bridge	2,451 (4-5 PM)	3,011 (8-9 AM)

Table 1 - Peak hour volumes of New York City's suspension bridges (Department of Transportation).

According to the FHWA, the number of passengers per vehicle is 1.7. Using these numbers, we conclude that the user costs in the case the Verrazano is closed exceed $50,000 per hour during peak hours. In the case of certain suspension bridges, toll losses are considerable since a majority of incidents happen during peak hours, implying that thousands of cars use alternative routes. The two toll suspension bridges of interest are the Verrazano-Narrows Bridge, which has a $19 toll (Inbound Staten Island only) and the George Washington Bridge, which has a $16 toll (Eastbound only). Continuing with the Verrazano example at peak hour, the toll losses reach $100,000. According to the NYDHSES data, 203 incidents out of the 355 in New York City were on suspension bridges. Figure 61 distributes incidents from January 2000 to June 2020.

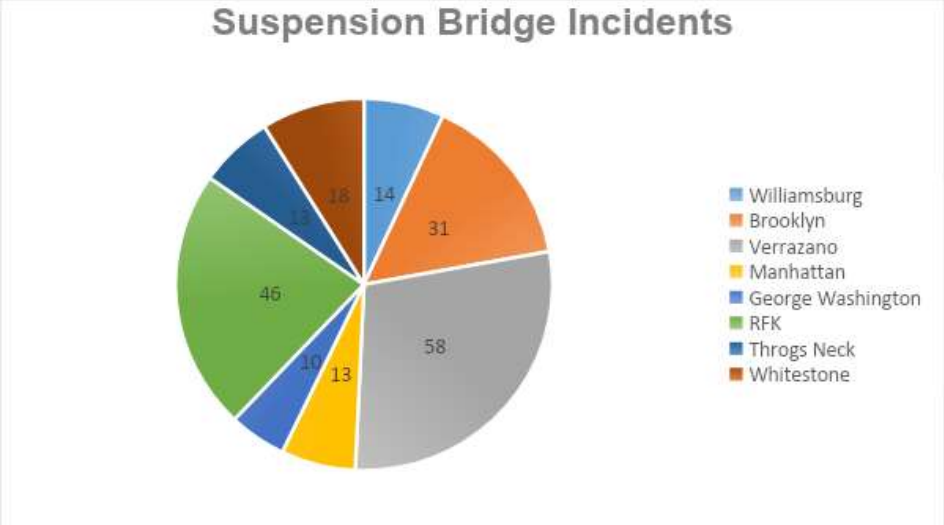

Figure 61 - Distribution of fire incidents on New York's suspension bridges

Case Studies

News outlets add pictures provided by bystanders on scene when available. Below are specific incidents including photogrammetry that have been used to determine approximate distances from the fire to the cable, with the help of known dimensions like lane width and truck height. Note in some cases the main cable is set up for inspection, meaning that the flames were considerably close to the cable and the possibility of the cable being damaged was evident. Moreover, these case studies reveal associated toll revenue losses (for bridges with tolls) with the stop of traffic.

Golden Gate Bridge

The car fire in Figure 62 partially shut down the Golden Gate Bridge from 2:39 PM to 3:15 PM . The innermost lanes of both sides were affected according to authorities, allowing traffic to resume on the outer lanes (CBS San Francisco). The cable height was scaled using the known height of the truck. The fire does not pose immediate danger to the main cable, but the suspenders remain vulnerable.

Figure 62 - Car fire on southbound Golden Gate Bridge, California (CBS San Francisco).

Walt Whitman Bridge

The Delaware River Port Authority closed both lanes of the Walt Whitman Bridge around 5:30 PM and reopened one lane in both directions at 6:20 PM (Cohen). The garbage truck fire (

Figure 63) did not pose great risk to the main cable. The bridge serves about 120,000 customers per day (Eastern Roads). From the evening rush hour delay, toll revenue loss is estimated at $20,000.

Figure 63 - Garbage truck fire on the Walt Whitman Bridge, New Jersey (Cohen).

Verrazano-Narrows Bridge

The truck fire from Figure 64 and Figure 65 was reported around 8:40 AM. Though the main cable is out of the fire's reach, the Verrazano-Narrows Bridge experienced a different situation because the truck was carrying compressed oxygen bottles. Emergency responders shut down traffic on both lanes due to the possibility of explosion by over-pressurization (Staten Island Advance). This led to a loss of approximately $51,000 in toll revenue during the hour the bridge was closed.

Figure 64 - Truck fire on the Verrazano-Narrows Bridge, New York (Berke).

Figure 65 - Truck fire on the Verrazano-Narrows Bridge (deck view), New York (Staten Island Advance).

Claiborne Pell/Newport Bridge

The car fire on the Claiborne Pell/Newport Bridge (Figure 66) occurred near mid-span around 2:59 PM and stopped traffic in both directions for an hour. Due to heavy traffic conditions, the fire department was delayed. Additionally, the response had to report from the east side, going against the flow of traffic (The Newport Daily News). Officials determined no structural damage after an inspection of the bridge (Durgin). Based on daily traffic numbers, the loss in toll revenue amounts to approximately $4,500.

Reports note pieces of the car melted into the pavement (The Newport Daily News), indicating temperatures as high as 660°C to melt the aluminum body. On the center-bottom of Figure 66, cable inspection equipment is visible, indicating possible exposed cable. With a horizontal distance of 5.29m and delayed response of the fire department, had the car and cable inspection equipment been on the same side, the high flames would easily reach the cable.

Figure 66 – Car fire on the Claiborne Pell/Newport Bridge, Rhode Island (The Newport Daily News).

Delaware Memorial Bridge

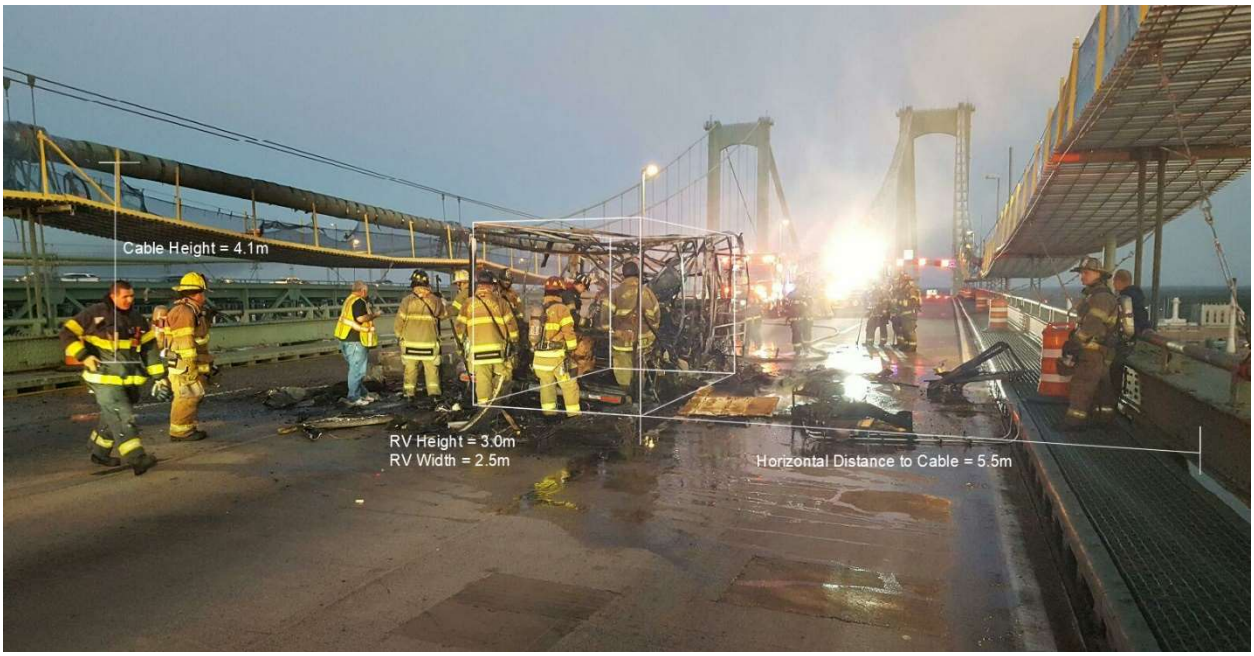

Figure 67 - RV fire on the eastbound Delaware Memorial Bridge, Delaware (WPVI-TV, 2016).

The RV fire on the Delaware Memorial Bridge (Figure 67) occurred at mid-span and burned a considerable amount of candy carried by the vehicle. This is where the cable is lowest – approximately 4.1m above the deck. The closest horizontal distance is at 5.5m. Cable inspection equipment can again be seen, meaning the cable was likely open and exposed at the time of the fire. The fire occurred around 6 PM, with lanes reopening around 9 PM. With one-way tolls at $4.75 US (with E-ZPass), loss in toll revenue averages $23,750.

Manhattan Bridge

The photo from the July 8th, 2009 truck fire (

Figure 68) was used in conjunction with the historical design profile (Figure 69) to find the height of the main cable. The fire did not reach the main cable, and the suspenders adjacent to the truck were only mildly hot (B. S. Yanev). This event showed that the heat from a fire dissipates rapidly when no in an enclosed space, and that the fuel sustaining the fire is not primarily the gas tank or an otherwise comparably powerful source.

On the contrary, the recent incident on the Manhattan Bridge (Figure 70) provides a great example of fires occurring close to a bridge cable. Judging from the color of the smoke, it is possible that the fuel source is mainly hydrocarbons, with some credit to the combustible solids of the car. The news report does not definitively recognize these parameters, but the fire is visibly high enough to make contact with the main cable. The car was reported to be engulfed in flames just after 6:15 PM; firefighters had it under control by 7:30 PM (Keogh). 75 minutes of direct exposure to a hydrocarbon fire presents concerns for the integrity of the main cable.

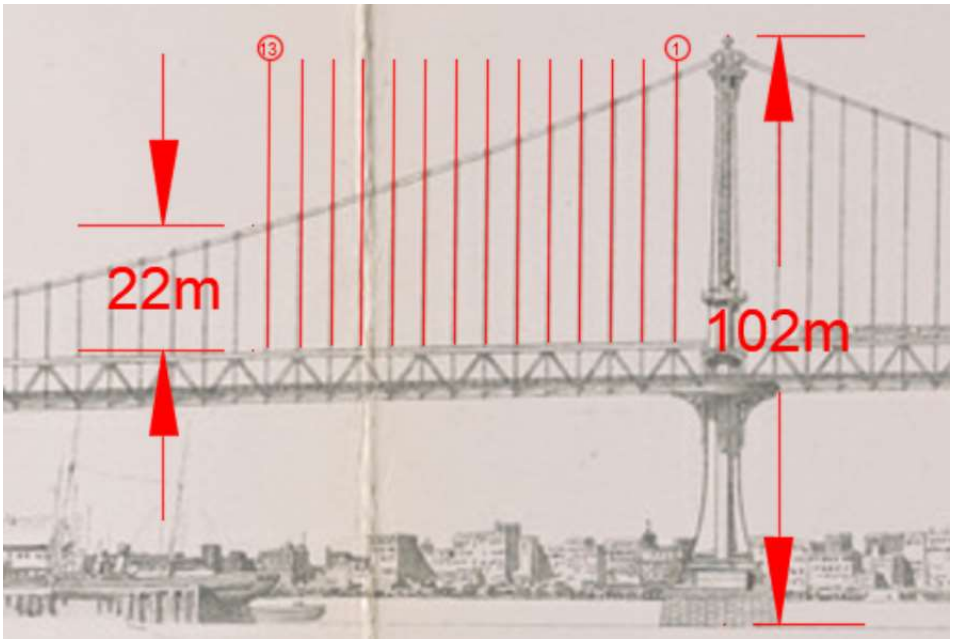

Figure 68 - Truck fire on upper level of the Manhattan Bridge, New York (B. S. Yanev).

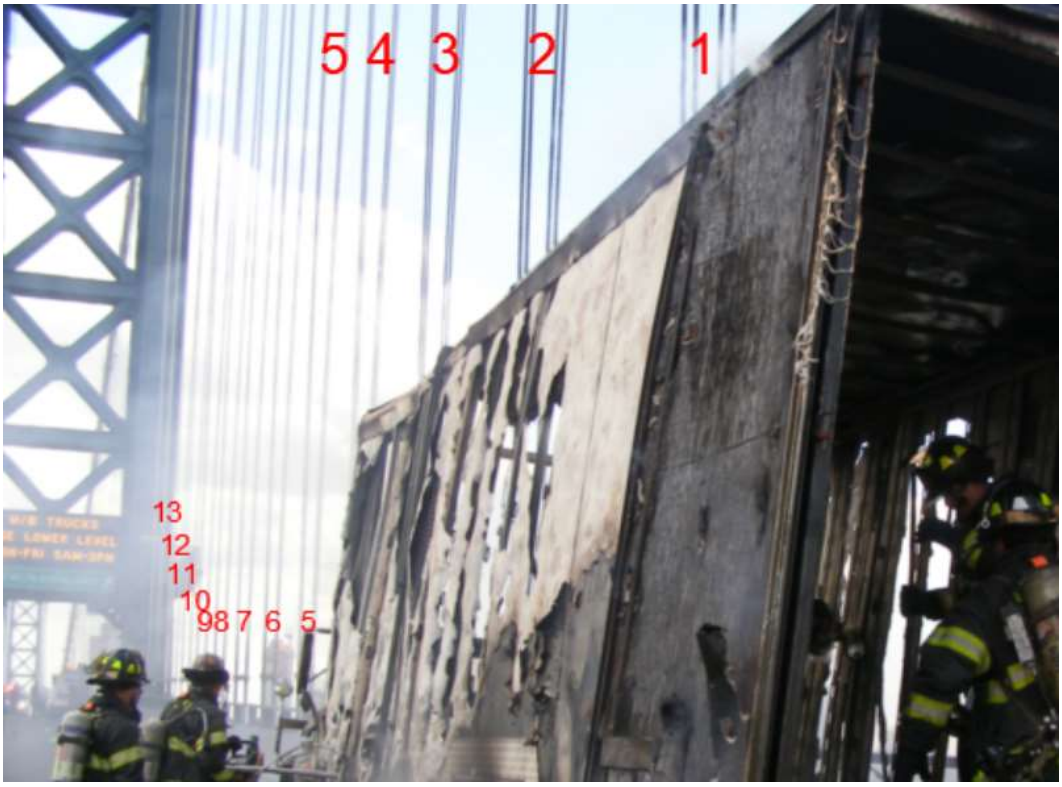

Figure 69 - Manhattan Bridge Profile (Brügger).

Figure 70 - Car fire on the Manhattan Bridge, New York (Keogh).

Conclusion

Fire incidents on suspension bridges have become an increasing risk to safety. The vehicles that catch fire contain flammables having potential to affect a suspension bridge's structural members. In many cases, these are hydrocarbon fires, which are known to burn at higher temperatures. Case studies have shown fires do occur mid-span or near the anchorage. The duration of these fires easily reaches an hour, which can lead to damage in the main cables. When not in close proximity to the main cables, fires can present danger to the suspenders, deck, and other structural components that will require repair or accelerated maintenance. Moreover, the economic impacts of suspension bridge fires must be considered. Not only is productivity of the community hindered, but also the toll revenue loss creates concern for bridge owners.

References

Baker, Al. *Truck Fire Is Put Out on Manhattan Bridge*. 8 July 2009. <https://cityroom.blogs.nytimes.com/2009/07/08/truck-fire-is-put-out-on-manhattan-bridge/?searchResultPosition=1.>.

Berke, Ned. *Photo: Truck Fire On Verrazano Bridge*. 22 September 2011. <https://bklyner.com/photo-truck-fire-on-verrazano-bridge-sheepshead-bay/>.

Brügger, Adrian. *Historical Drawings* Tak Sohn and Julien Naddaf. 17 July 2020.

CBS San Francisco. *CBS San Francisco*. 21 July 2020. <https://sanfrancisco.cbslocal.com/2020/07/21/car-bursts-into-flames-on-southbound-golden-gate-bridge-closing-lanes/>.

Cohen, Noah. *nj*. 24 February 2020. <https://www.nj.com/news/2020/02/truck-fire-forces-closure-of-walt-whitman-bridge.html>.

Delaware River & Bay Authority. *DRBA*. 2020. <http://www.drba.net/DelawareMemorialBridge/AbouttheDelMemorialBridge.aspx>.

Delaware River Port Authority. *DRPA*. 2020. <http://www.drpa.org/travel/toll-schedule.html>.

Department of Transportation, New York City. *2016 New York City Bridge Traffic Volumes*. New York, 2016.

Durgin, Marianne. *NPB 10-08-2018* Tak Sohn. 2 July 2020.

Eastern Roads. *Philly Roads*. n.d. <http://www.phillyroads.com/crossings/walt-whitman/>.

Federal Highway Administration. "Average Vehicle Occupancy Factors for Computing Travel Time Reliability Measures and Total Peak Hour Excessive Delay Metrics." 2018.

Garlock, Maria, et al. "Fire hazard in bridges: Review, assessment and repair strategies." *Engineering Structures* (2012).

Kelly, PA. *Mechanics Lecture Notes: Introduction to Plasticity*. 23 May 2015. University of Auckland. Website. <http://homepages.engineering.auckland.ac.nz/~pkel015/SolidMechanicsBooks/Part_II/08_Plasticity/08_Plasticity_01_Introduction.pdf>.

Keogh, Elizabeth. *NY Daily News*. 4 July 2020. <https://www.nydailynews.com/new-york/manhattan/ny-manhattan-bridge-fire-20200705-lvpeigf7qrfwnmipyrzwatx3gi-story.html>.

Metropolitan Transportation Authority. *Car Toll Rates*. 2020. <https://new.mta.info/fares-and-tolls/bridges-and-tunnels/tolls-by-vehicle/cars>.

New York State Department of Labor. *Department of Labor*. 2020. <https://labor.ny.gov/stats/ceshourearn2.asp>.

Peris-Sayol, Guillem. "Analysis of the fire response of multi-girder steel bridges." 2017.

Rhode Island Turnpike and Bridge Authority. *RITBA*. 2020. <http://www.ritba.org/tolls>.

Robinson, Jumari. *Modelling Elasticity and Plasticity of High-Strength Bridge-Wire at High Temperature*. ENME E6333 Finite Element Analsis II Final Project. Columbia University. New York, 2019.

San Francisco Fire Department. *Apparatus Inventory*. San Francisco: San Francisco Fire Department, 2009.

Staten Island Advance. *silive*. 22 September 2011. <https://www.silive.com/news/2011/09/truck_laden_with_gas_bottles_c.html>.

The Newport Daily News. *Cause of Car Fire on Bridge Uncertain: VIDEO*. 8 October 2018. <https://www.newportri.com/news/20181008/cause-of-car-fire-on-bridge-uncertain--video>.

U.S. Fire Administration; National Fire Data Center. "National Fire Incident Reporting System: Complete Reference Guide." 2015.

WPVI-TV. *6abc*. 25 February 2020. <https://6abc.com/walt-whitman-bridge-fire-on-video/5964372/>.

—. *6abc*. 24 October 2016. <https://6abc.com/delaware-memorial-bridge-bus-fire-pot-marijuana/1569435/>.

Yanev, Bojidar and Earl Dubin. "Managing the East River bridges in New York City." *Health Monitoring and Management of Civil Infrastructure Systems* 4337 (2001): 60-74. Proceedings.

Yanev, Bojidar S. *Fire Project with Rutgers UTC - RFI* Adrian Brügger. 1 July 2020.

Yaw, Louie L. 25 January 2012. *Nonlinear Static - 1D Plasticity - Various Forms of Isotropic Hardening.* Walla Walla University. August 2020. <https://gab.wallawalla.edu/~louie.yaw/plasticitypublications/1Dplasticity.pdf>.

—. "Nonlinear Static - 1D Plasticity - Isotropic and Kinematic Hardening ." 18 January 2017. Walla Walla University. August 2020. <https://gab.wallawalla.edu/~louie.yaw/plasticitypublications/1DplasticityIsoKin.pdf >.

APPENDIX A: DOCUMENTATION FOR 7-WIRE ABAQUS MODEL

Overview

The 7 wire model.cae file contains three model with different setups. All three model have the same wire geometries and material properties. The difference between those models are the clamp geometries and connector behaviors.

Model-1-newclamp: It contains the configuration of the small clamp. The connector behaviors are all set to be nonlinear elastic with undetermined parameters. Equation constrains are imposed on clamps and both ends of the wires to ensure symmetric behavior of the whole structure. This is the most primal version of this 7 – wire model with the most stable convergence behavior. Further changes, like adding more complex connector behaviors is based on this model.

Model-largeclamp-friction: It contains the configuration of the model with the large clamp. Besides the clamp geometry, the connector behaviors are also updated in this model. Failure and friction behaviors are added in U2 and U3 directions and all the parameters for the connector behaviors are tuned according to either analytical solution (Raoof and Huang) or the experimental data (Pull out test all round).

Model-largeclamp-pullout: It is updated from the **Model-largeclamp-friction**. The equation constrains on the wires are removed and new boundary conditions and load are added into the model to better represent the experimental configuration. The connector behaviors remain the same as the large clamp model.

Instructions

All three models have boundary conditions which constrains the rotational degrees of freedom of the start point of each connector. Those boundary conditions are essential because when a connector is set between two nodes, it activates the rotational degrees of freedom at the start point of the connector. If those boundary conditions are removed, those nodes will experience rigid body motion. Those points are in fact the most unstable factor in this analysis. Using boundary conditions to stabilize those points are more like a compromise instead of a solution. Those boundary conditions can later lead to over constraining when imposing new behavior to the connectors. One can try using constrains (rigid body, coupling) to stabilize these points. One way or another these rotational degrees of freedom should be constrained but using boundary conditions is not a perfect solution.

Other than the boundary conditions on start points of connectors, there are no other boundary conditions on **Model-1-newclamp** and **Model-largeclamp-friction**. The systems are stabilized using only equation constrains in those two models. Due to this set up some degrees of freedom of the nodes which have constrains are removed. When someone wants to impose boundary conditions on these nodes, those equation constrains should be removed first.

There are four types of connectors behaviors in **Model-largeclamp-friction** and **Model-largeclamp-pullout**. Two of them, nonlinear elasticity and friction, will most likely cause convergence issue.

For nonlinear elasticity, all parameters are given in a tabular form (the data points on stress strain curve). Abaqus will do a linear interpolation of those data and generate a force-displacement response. One possible reason for a diverging solution is using ill-conditioned data points which will result a fluctuate interpolated response curve.

For friction behavior, if modeling friction in both U1 and U3 directions, the slip direction should be computed using force potential instead of directly set to be the longitudinal direction. The stick stiffness is another important parameter. Using the default value will cause convergence issue in most cases.

APPENDIX B: THERMODYNAMIC MATERIAL PROPERTIES

Material Properties Defined in the Three-Dimensional Experimental Cooling Model

All the material properties applied in the three-dimensional model are listed in Table A1-1. The cross-sectional thermal conductivity is obtained from a combination of recent experimental results [2] and previous work done by M.J.D. Sloane in 2016 [3], and the longitudinal thermal conductivity is determined by the area ratio of all steel wires on the whole cross-section of the cable.

Whole Cable				
Parameter	**Symbol**	**Unit**	**Value**	
Young's Modulus	E	GPa	205	
Poisson's ratio	γ		0.3	
Density	ϱ	kg/m3	7101	
Specific Heat	Cp	J/kg/K	503.2	
Thermal Conductivity	K	W/m/K	Longitudinal	40.05
			Cross-Sectional	1.55
Expansion Coefficient	Ec		1.0654E-05	

Table A1-1: Material properties applied in the three-dimensional experimental cooling model

Calculation Procedure of Natural Convective Heat Transfer Coefficient on the Curved Surface of Bridge Main Cable

To calculate this coefficient, we have to introduce four dimensionless numbers: Nusselt number, Rayleigh number, Prandtl number and Grashof number. As shown in Figure A2-1, these four numbers constitute the empirical correlation along with heat transfer coefficient.

$$Gr = \frac{D^3 \rho^2 g \Delta T}{\mu^2} \qquad Nu = \frac{hD}{k} \qquad Pr = \frac{\mu C_p}{k} \qquad Ra = Gr * Pr$$

Nu – *Nusselt Number* k – *thermal conductivity of fluid*

Ra – *Rayleigh Number* D – *diameter of cylinder*

Pr – *Prandtl Number* β – *thermal expansion coeff.*

Gr – *Grashof Number* ρ – *density of fluid*

C_p – *heat capacity of fluid* μ – *viscosity of fluid*

Figure A2-1: The computational formulas of dimensionless numbers in natural air cooling condition [7]

Obviously, we must firstly define fluid properties. The temperature to be used for fluid properties in natural convection is typically the film temperature, which is defined as the average temperature between the fluid far from the solid surface and that of the solid surface. We assume the temperature of air far from the cable remains constant and is equal to room temperature (20°C). According to the initial condition of the cooling model, the entire fire surface temperature of the cable is 460°C, so the film temperature is 240°C. The thermal properties of air are consequently derived, as shown in Table A2-1.

Air			
Parameter	**Symbol**	**Unit**	**Value**
Temperature	T1	℃	20
Viscosity	μ	Ns/m2	3.763E-05
Density	ϱ	kg/m3	0.4153
Specific Heat	Cp	J/kg/K	1.11
Thermal Conductivity	K	W/m/K	6.03E-05
Thermal Expansion Coefficient	β	1/K	0.0012

Table A2-1: Air parameters used to calculate dimensionless numbers in natural air cooling condition

To calculate Nusselt number, we apply the following formula. By this method, the heat transfer coefficient remains constant on the curved surface of cable.

$$Nu = \left(0.60 + \frac{0.386\,Ra^{1/6}}{(1+(0.559/Pr)^{\frac{9}{16}})^{8/27}}\right)^2 \qquad (6)$$

Ultimately, we get the natural convective heat transfer coefficient on the curved surface as 7.48W/m^2/K. The values of parameters related to this calculation procedure are listed in Table A2-2.

Air Natural Cooling			
Parameter	**Symbol**	**Unit**	**Value**
Prandtl number	Pr		0.7155
Grashof number	Gr		1.97E+08
Rayleigh number	Ra		1.41E+08
Nusselt number	Nu		62.9
Convective Heat Transfer Coefficient	h	W/m2/K	7.36

Table A2-2: The values of dimensionless numbers and heat transfer coefficient in natural air cooling condition

Calculation Procedure of Natural Convective Heat Transfer Coefficient on the Flat Surfaces of Bridge Main Cable

The cooling process on the flat surfaces of the cable is also a natural air-cooling process, but the condition of the object cooled in this case is changed. A method from Churchill and Chu [6] is applied to estimate the heat transfer coefficient on the flat surfaces. This method is applicable for natural convection from a vertical surface.

$$Nu = \left(0.825 + \frac{0.387\, Ra^{1/6}}{(1+(0.492/Pr)^{\frac{9}{16}})^{\frac{8}{27}}}\right)^2 \qquad (7)$$

However, the calculation procedure is still similar, and the coolant properties remain the same as shown in Table A2-1. The only difference lies in the correlation among Nusselt, Grashof and Rayleigh number, which is shown in eq.(7). In the end, a natural convective heat transfer coefficient of 6.14W/m^2/K comes from the calculations.

Expression Fitting of Sensor Temperature on Each Instrumented Cross-Sections

The expression fitting starts with a simple, quadratic radial fit that reflects the temperature distribution along the two, diagonals, which is strongly second order in nature, though asymmetric:

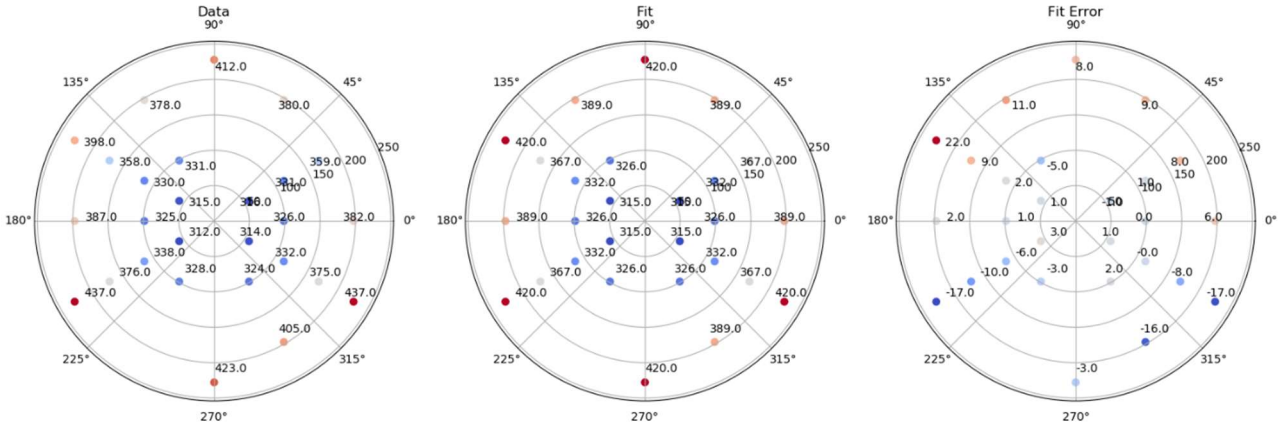

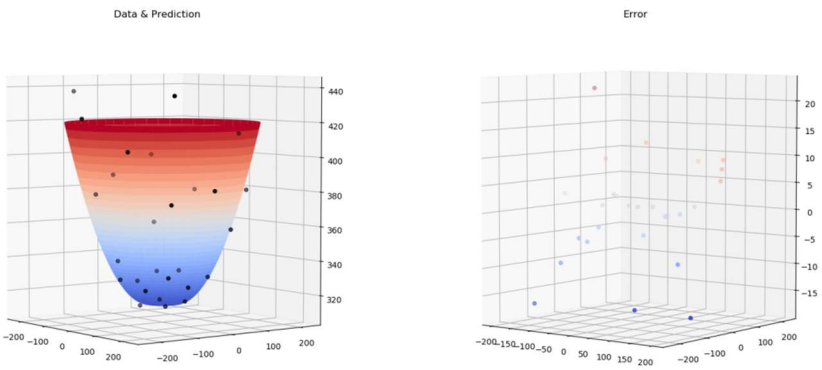

Figure A4-1: Quadratic radial fit for the central cross-section

This prediction fits temperature as a 2nd order function of radius, without angle dependence. Since there are indeed hotter and colder spaces in the furnace, the experimental temperature distribution is not symmetric. Since it is worked in polar coordinates here, the fitting function cannot apply asymmetry to the model without angle dependence. The fitting error (in °C) plotted in the upper-right diagram shows a general bottom-to-top skew in the error. The two lower diagrams simply show the data, prediction, and error (°C) with temperature allocated as a 3rd dimension. From the appearance of the residual, it is apparent that much more the error can be reduced by superimposing a planar temperature function. As such, we arrive at the form:

$$T(r,\theta) = ar^2 + br + c + dr\sin\theta + er\cos\theta \quad (8)$$
$$0\ mm \leq\ r\ \leq\ 254\ mm$$
$$-\pi\ \leq\ \theta\ \leq\ +\pi$$

This produces the result for the central cross-section:

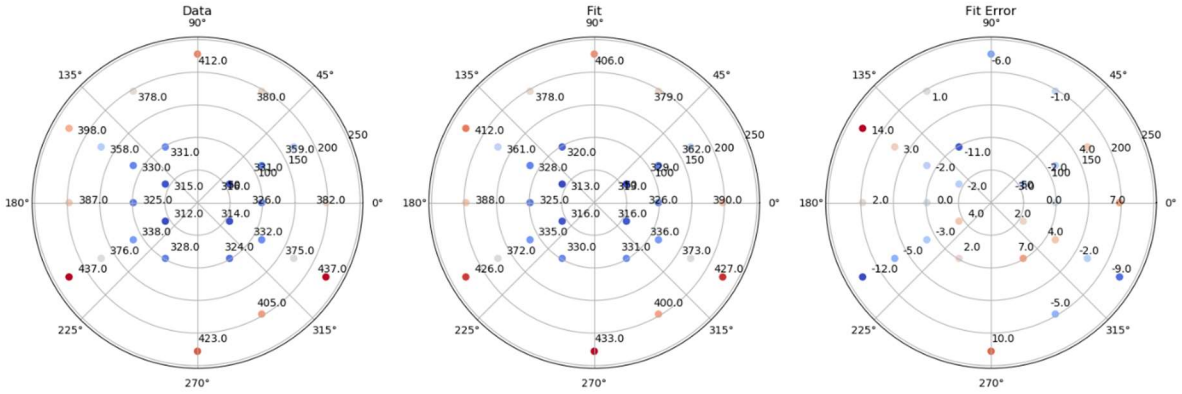

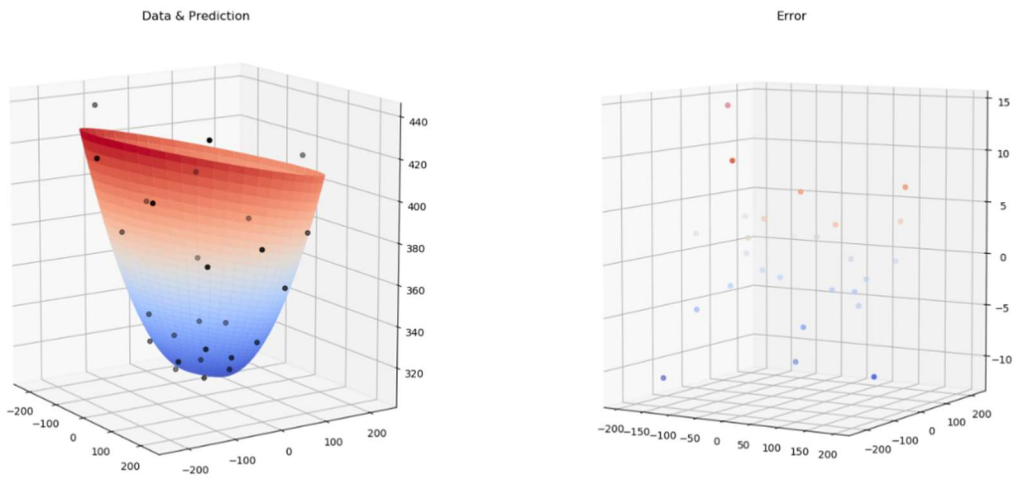

Figure A4-2: Planar temperature function of the central cross-section

This representation does manage to capture the asymmetric heating conditions better. The magnitude of the large error on some edges is due to the two radiators being directly underneath those sensors. Higher order angle dependencies have been tried, but they either do not help, or trade a lot of accuracy in the center for a fraction more accuracy near the edges. We do not think there is a particular smooth function that can approximate the temperature field better, unless we get into Fourier sums, which is probably a bit overkill. The root mean square error of this fit on the central cross-section is 5.7°C, 7.5°C at the cross-section at 20in. away from the center, and less than 3°C at the other two cross-sections (where the bias is very small due to the distance from the furnace.) The results from those fits are presented below:

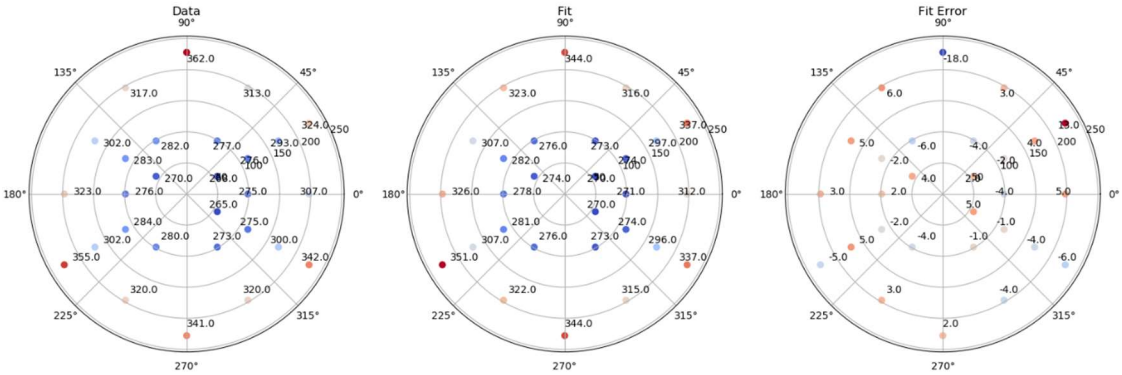

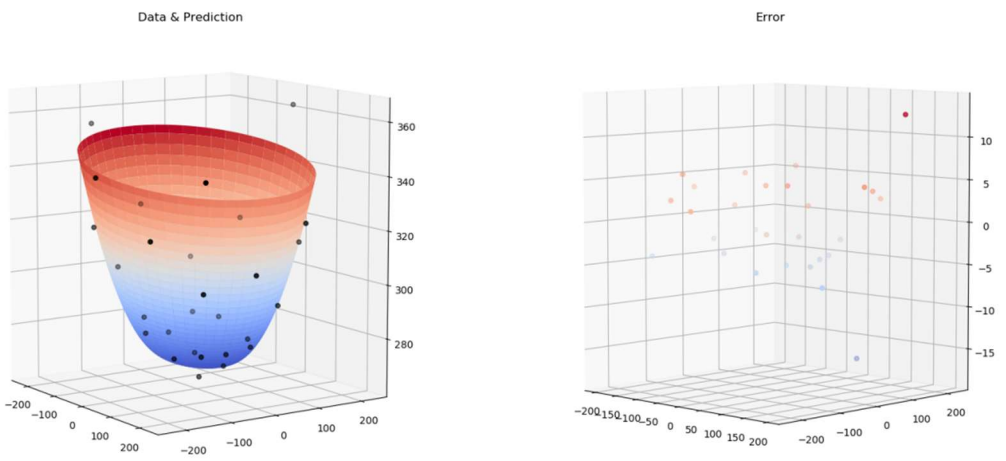

Figure A4-3: Expression fitting of the cross-section at 20in. away from the center

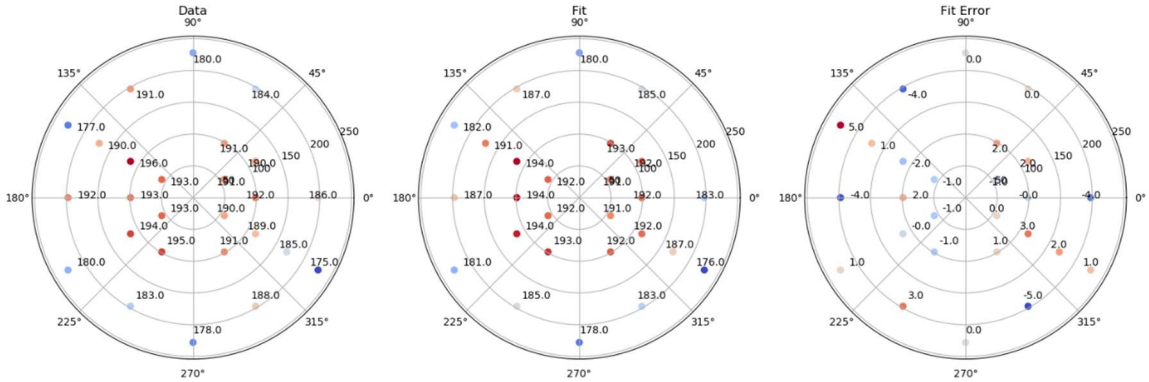

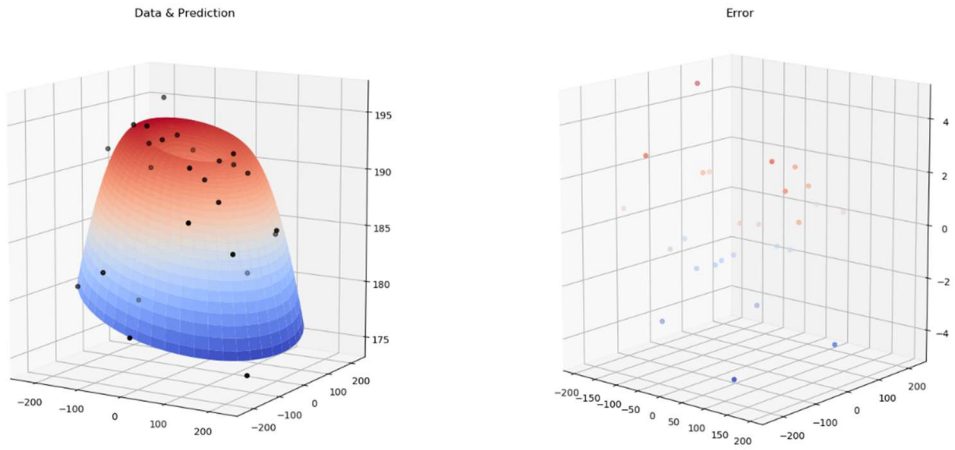

Figure A4-4: Expression fitting of the cross-section at 40in. away from the center

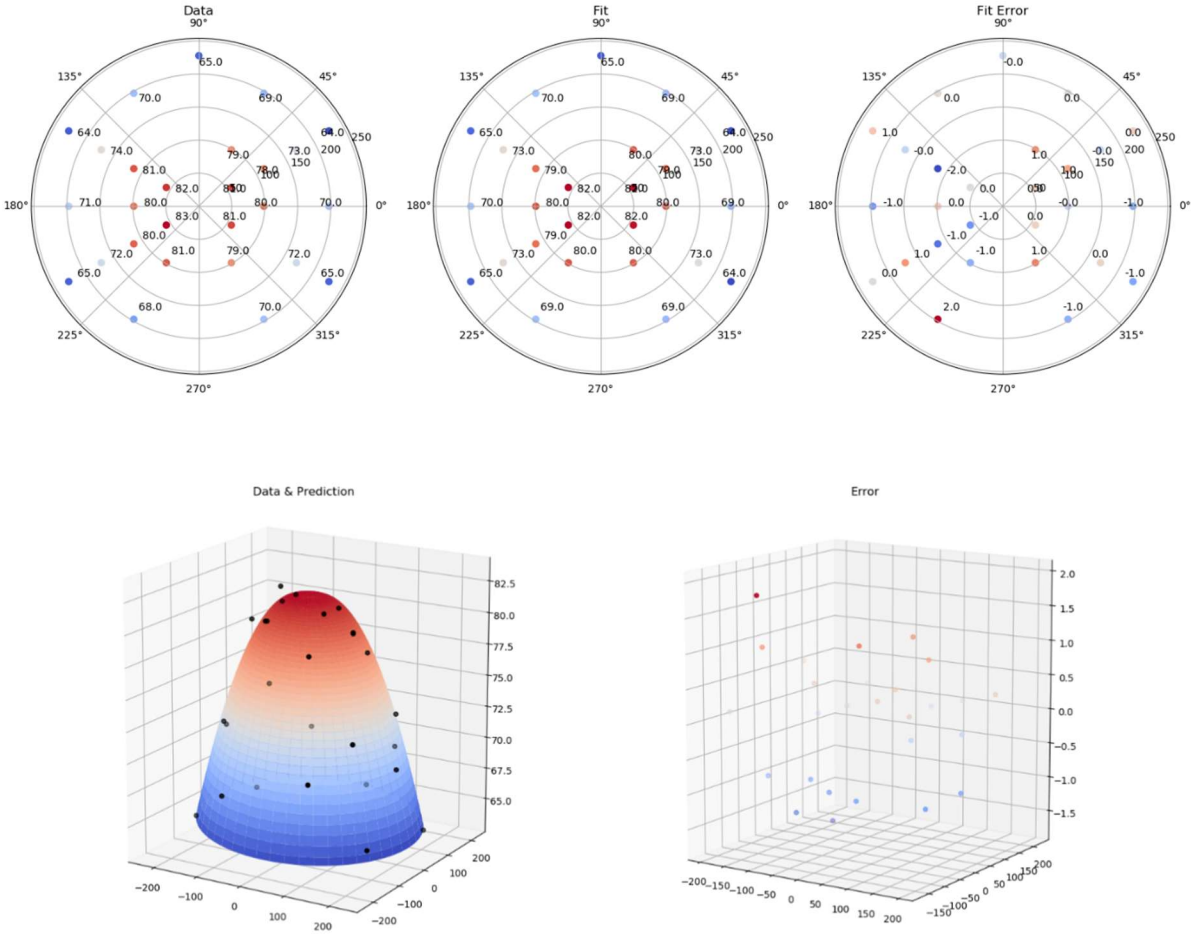

Figure A4-5: Expression fitting of the cross-section at 80in. away from the center

If ABAQUS model is built in Cartesian coordinates, we need to convert *x* and *y* coordinates to *r* and θ via:

$$r = \sqrt{x^2 + y^2} \qquad (9a)$$

$$\theta = \tan^{-1}\frac{y}{x} \qquad (9b)$$

While making sure that the θ domain is between $-\pi$ and $+\pi$. This is very important. The inverse tangent function has a range between $-\pi/2$ and $+\pi/2$. This means that it will spit out a semi-circle, which is not what we want. In Python, the function that handles this correctly is "arctan2". There is a built in MATLAB function that imparts the inverse tangent domain in the same way. Once the coordinates are transformed to polar, we can plug them into this function to get an initial condition for each node.

With regards to the different cross-sections, there is only a clear trend in the "c" coefficient, which corresponds to the general temperature scale of each cross-section. As such, we would just use linear interpolation between the cross-sections to determine each coefficient at the intermediate Z-positions. The coefficients at each section are presented in Table A4-1.

Z-Position (cm from center)	a	b	c	d	e
0	0.00269545	-0.152911	314.387	-0.0604015	0.0040984
51	0.00276549	-0.366365	283.729	0.00122798	-0.0360493
101	-0.000901816	0.184654	183.684	0.00409321	-0.0120391
203	-0.000436626	0.0227784	81.8999	0.000818392	-0.00244621

Table A4-1: Specific values of each parameters in eq.(8) for different cross-sections

Simulation Results and Experimental Data on the Central Cross-Section

According to the distance between sensors and the center of cable, it is easy to find that all sensors are distributed onto six annuli. From surface to center, we number these annuli from I to VI, respectively. Figure A5-1 shows these six annuli on the cross-section of main cable and the sensor distribution.

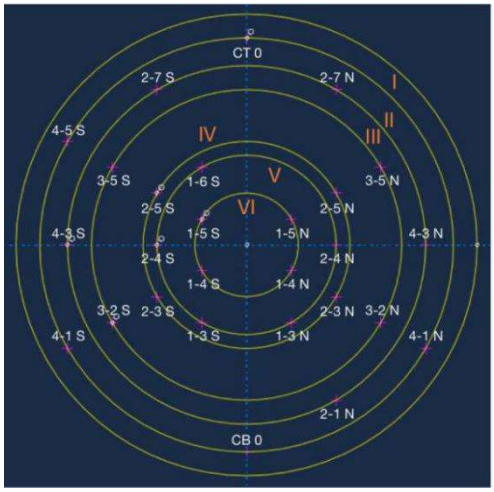

Figure A5-1: Six annuli that sensors are distributed on the cross-section of main cable

The simulation results, experimental data and corresponding errors at each location of sensors are listed in the following six tables. All 27 sensors are located on the central cross-section of the cable. The data includes the specific value comparison of temperature after one-hour, four-hours and five-hours cooling. The error is calculated as the absolute percentage error. Sensors on the same annulus always have similar temperatures on matter in simulation or experiment, which follows the general rule of heat transfer in bridge main cable.

Annulus (I)												
Sensor	**Initial Condition**			**Cooling for 1 Hour**			**Cooling for 4 Hours**			**Cooling for 5 Hours**		
	Temperature (℃)		Error (%)	Temperature (℃)		Error (%)	Temperature (℃)		Error (%)	Temperature (℃)		Error (%)
	Exper.	Sim.		Exper.	Sim.		Exper.	Sim.		Exper.	Sim.	
4-5 S	394.6	411.8	4.4	304.5	341.5	12.2	207.9	243.8	17.3	192.3	224.2	16.6
4-1 S	430.0	425.6	1.0	317.3	349.0	10.0	207.9	247.2	18.9	191.3	226.9	18.6
CT 0	400.6	405.7	1.3	292.0	335.4	14.9	198.6	242.2	21.9	183.2	223.1	21.8
CB 0	417.1	433.2	3.9	317.0	352.1	11.1	208.5	248.7	19.3	191.7	228.3	19.1
4-1 N	429.6	427.2	0.6	318.9	348.1	9.1	211.9	247.7	16.9	195.4	227.6	16.5

Table A5-1: Simulation results and experimental data on annuli I

Annulus (II)												
Sensor	**Initial Condition**			**Cooling for 1 Hour**			**Cooling for 4 Hours**			**Cooling for 5 Hours**		
	Temperature (℃)		Error (%)	Temperature (℃)		Error (%)	Temperature (℃)		Error (%)	Temperature (℃)		Error (%)
	Exper.	Sim.		Exper.	Sim.		Exper.	Sim.		Exper.	Sim.	
4-3 N	383.0	390.0	1.8	350.2	349.2	0.3	253.8	264.9	4.4	235.3	245.3	4.3
2-1 N	404.8	399.9	1.2	353.3	356.7	1.0	244.0	268.3	10.0	225.3	248.0	10.1
4-3 S	387.1	388.4	0.3	338.3	352.5	4.2	236.7	265.6	12.2	218.8	245.6	12.2
2-7 S	378.0	378.4	0.1	336.6	345.1	2.5	238.6	262.5	10.0	220.3	243.1	10.3
2-7 N	380.5	379.3	0.3	339.2	344.9	1.7	241.1	263.0	9.1	222.7	243.7	9.4

Table A5-2: Simulation results and experimental data on annuli II

Annulus (III)												
Sensor	**Initial Condition**			**Cooling for 1 Hour**			**Cooling for 4 Hours**			**Cooling for 5 Hours**		
	Temperature (°C)		Error (%)	Temperature (°C)		Error (%)	Temperature (°C)		Error (%)	Temperature (°C)		Error (%)
	Exper.	Sim.		Exper.	Sim.		Exper.	Sim.		Exper.	Sim.	
3-5 S	358.8	361.2	0.7	337.9	343.1	1.6	256.5	275.3	7.3	238.8	256.8	7.5
3-2 S	377.2	371.5	1.5	353.3	349.7	1.0	260.5	278.6	6.9	241.7	259.5	7.4
3-5 N	359.3	362.4	0.9	342.4	342.1	0.1	265.2	276.2	4.2	247.5	257.9	4.2
3-2 N	375.2	372.7	0.7	353.1	347.9	1.5	265.2	278.5	5.0	246.9	259.7	5.2

Table A5-3: Simulation results and experimental data on annuli III

Annulus (IV)												
Sensor	**Initial Condition**			**Cooling for 1 Hour**			**Cooling for 4 Hours**			**Cooling for 5 Hours**		
	Temperature (°C)		Error (%)	Temperature (°C)		Error (%)	Temperature (°C)		Error (%)	Temperature (°C)		Error (%)
	Exper.	Sim.		Exper.	Sim.		Exper.	Sim.		Exper.	Sim.	
2-5 S	330.7	328.1	0.8	331.1	320.3	3.3	281.5	287.9	2.3	264.7	273.9	3.5
2-3 S	338.0	335.0	0.9	337.8	324.6	3.9	283.9	290.1	2.2	266.5	275.7	3.4
2-5 N	331.6	328.9	0.8	332.6	319.1	4.1	285.3	288.0	1.0	268.7	274.2	2.1
2-3 N	332.6	335.8	0.9	334.2	323.4	3.2	288.5	290.6	0.7	272.1	276.3	1.5

Table A5-4: Simulation results and experimental data on annuli IV

Annulus (V)												
Sensor	**Initial Condition**			**Cooling for 1 Hour**			**Cooling for 4 Hours**			**Cooling for 5 Hours**		
	Temperature (°C)		Error (%)	Temperature (°C)		Error (%)	Temperature (°C)		Error (%)	Temperature (°C)		Error (%)
	Exper.	Sim.		Exper.	Sim.		Exper.	Sim.		Exper.	Sim.	
2-4 S	325.9	325.1	0.2	329.1	317.2	3.6	286.9	289.6	0.9	270.6	276.7	2.3
1-6 S	331.6	320.2	3.5	332.5	313.7	5.7	281.3	288.1	2.4	264.1	275.5	4.3
1-3 S	328.9	330.5	0.5	332.4	319.9	3.8	292.5	291.6	0.3	275.8	278.4	0.9
1-3 N	324.7	330.9	1.9	328.7	319.6	2.8	293.7	291.5	0.7	277.9	278.4	0.2
2-4 N	326.5	325.9	0.2	330.0	315.8	4.3	291.0	289.9	0.4	275.0	277.2	0.8

Table A5-5: Simulation results and experimental data on annuli V

Annulus (VI)												
Sensor	**Initial Condition**			**Cooling for 1 Hour**			**Cooling for 4 Hours**			**Cooling for 5 Hours**		
	Temperature (℃)		Error (%)	Temperature (℃)		Error (%)	Temperature (℃)		Error (%)	Temperature (℃)		Error (%)
	Exper.	Sim.		Exper.	Sim.		Exper.	Sim.		Exper.	Sim.	
1-5 S	315.4	312.5	0.9	319.8	305.0	4.6	291.2	289.4	0.6	275.9	279.6	1.3
1-4 S	313.1	315.9	0.9	318.6	307.3	3.5	293.7	290.6	1.0	278.7	280.6	0.7
1-5 N	316.6	312.9	1.2	320.8	304.5	5.1	293.6	289.5	1.4	278.4	279.8	0.5
1-4 N	314.7	316.4	0.5	319.8	306.4	4.2	296.1	290.7	1.8	281.4	280.8	0.2

Table A5-6: Simulation results and experimental data on annuli VI

APPENDIX C: PERIS-SAYOL DATABASE (2017)

Code	Identificative Name	Date of incident	Location	Structural System	Ignition Source	Type of Combustible
1	Little Black River	2006	Ripley County, MI,USA	I Girders	Unknown	
2	Riderwood	8/19/1997	Baltimore, MD, USA	I Girders	Tanker	Gasoline
3	NYS Thruway	10/9/1997	Yonkers, NY, USA	I Girders	Tanker	Gasoline
4	Dumbarton Rail Bridge	1/7/1998	Palo Alto, CA, USA	Truss	Arson	-
5	Chester Creek	5/23/1998	Chester Creek, PA, USA	I Girders	Tanker	Gasoline
6	Valdese	7/23/1998	Valdese, NC, USA	I Girders	Tanker	Gasoline
7	Benjamin Franklin Brigde	9/30/1998	New York, NY, USA	Suspension	Cigarrete	-
8	Overpass Cypress/Spring	3/16/1999	Spring, TX, USA	I Girders	Tanker	Gasoline
9	RI37 Expressway	7/20/2000	Cranston, RI, USA	I Girders	Tanker	Jet Fuel
10	I-285 over GA400	6/9/2001	Atlanta, GA, USA	I Girders	Tanker	Gasoline
11	Denville	6/22/2001	Denville, NJ, USA	Box Girders	Tanker	Gasoline
12	Independance Parkway	12/28/2001	Tampa, FL, USA	I Girders	Tanker	Gasoline
13	Birmingham 2002	1/5/2002	Birmingham, AL, USA	I Girders	Tanker	Gasoline
14	The Jeffries Ford Covered Bridge	4/2/2002	Bridgeton, IN, USA	Covered / Truss	Arson	-
15	Turkey Creek Bridge	4/12/2002	Sharon Springs, KS, USA	Truss	Train braking	-
16	Puyallup River	12/11/2002	Tacoma, WA, USA	I Girders	Railroad Tanker	Methanol
17	Flint	1/30/2003	Flint, MI, USA	I Girders	Tanker	Propanol
18	Elkridge	1/13/2004	Elkridge, MD, USA	I Girders	Tanker	Gasoline
19	I-75 Big slough Canal	2/2/2004	North Port, FL, USA	I Girders	Tanker	Gasoline
20	Howard Avenue	3/25/2004	Bridgeport, CT, USA	I Girders	Tanker	Fuel Oil
21	Mungo River bridge	7/1/2004	Cameroon	Truss	Tanker	Petroleum
22	Wielhtalbridge	8/26/2004	Gummersbach, Germany	Box Girders	Tanker	Gasoline
23	Birmingham 2004	10/21/2004	Birmingham, AL, USA	I Girders	Tanker	Gasoline
24	Charilaos Trikoupis Bridge	1/28/2005	Greece	Cable-Stayed	Thunderbolt	-
25	Old Bridgeton Covered Bridge	4/29/2005	Bridgeton, IN, USA	Covered / Truss	Arson	-
26	Opatovice	5/7/2005	Opatovice, Republica Checa	Truss	Carbon Fire	
27	Norwalk River Bridge	7/12/2005	Ridgefield, CT, USA	I Girders	Tanker	Gasoline
28	Brucknen Expressway	10/4/2005	New York, NY, USA	I Girders	Tanker	Fuel Home
29	Queensboro Bridge Oct. 2005	10/18/2005	New York, NY, USA	Truss	Wood Scaffolding Fire	-
30	Pico Rivera	11/3/2005	Pico Rivera, CA, USA	Trestle	Arson	
31	Brooklyn-Queens Expressway 06	1/16/2006	New York, NY, USA	I Girders	Tanker	Gasoline
32	Belle Isle	1/28/2006	Oklahoma, OK, USA	I Girders	Truck	-
33	Brookside Train Trestle	5/23/2006	Brookside, AL, USA	Truss	Wildfire	-
34	Bill Williams Bridge	7/28/2006	Parker, AZ, USA	I Girders	Tanker	Diesel

Code	Identificative Name	Date of incident	Location	Structural System	Ignition Source	Type of Combustible
35	Norfolk Southern Train	10/20/2006	New Brighton, PA, USA	Truss	Railroad Tanker	Ethanol
36	Mezcala	3/17/2007	Guerrero, Mexico	Cable-Stayed	Truck	
37	St. Petersburg	3/27/2007	St. Petersburg, FL, USA	I Girders	Tanker	Diesel
38	MacArthur Maze	4/29/2007	Oakland, CA, USA	I Girders	Tanker	Gasoline
39	Ethanol Baltimore	5/14/2007	Baltimore, MD, USA	I Girders	Tanker	Ethanol
40	Stop thirty Road	6/20/2007	Nashville, TN, USA	Box Girders	Tanker	-
41	Tappan Zee Bridge	7/2/2007	New York, NY, USA	Truss	Truck	-
42	Autoroute N05	7/30/2007	France	Box Girders	Car	-
43	Jeffersoncity	11/27/2007	Jeffersoncity, MO, USA	I Girders	Tanker	Gasoline
44	Regensburg	3/13/2008	Regensburg, Alemania	I Girders	Boat Fire	
45	Dewey Bridge Grand County	4/6/2008	Moab, UT, USA	Suspension	Arson	-
46	Big Four	5/7/2008	Louisville, KY, USA	Truss	Electrical Problem	-
47	Manatee	6/4/2008	Tampa, FL, USA	I Girders	Tanker	Gasoline
48	160th Street Bridge	6/18/2008	Page County, IA, USA	Truss	Wildfire	-
49	Eko Bridge	7/11/2008	Nigeria	Box Girders	Truck	-
50	Brooklyn-Queens Expressway 08	10/6/2008	New York, NY, USA	I Girders	Truck	-
51	Dallas	10/13/2008	Dallas, TX, USA	Box Girders	Tanker	Gasoline
52	Gudgeonville Covered Bridge	11/8/2008	Girard, PA, USA	Covered / Truss	Arson	-
53	Viaducto sobre el barranco Cotubro	11/19/2008	Almuñecar, España	I Girders	Truck	-
54	Hedong Cable-Stayed	12/26/2008	China	Cable-Stayed	Other	
55	Patullo Bridge	1/18/2009	Surrey, Brithish Columbia, Canada	Truss	Storage	Homeless
56	Throgs Neck Bridge	7/10/2009	New York, NY, USA	Suspension	Wood Scaffolding Fire	-
57	Hazel Park	7/15/2009	Detroit, MI, USA	I Girders	Tanker	Gasoline
58	Manhattan Bridge	8/7/2009	New York, NY, USA	Suspension	Truck	Garbage
59	Sunnyside	8/21/2009	Yakima County, WA, USA	I Girders	Wildfire	
60	Gaojiahuayuan Bridge	9/3/2009	China	Box Girders	Workers Maintenance	
61	California Avenue Overpass	9/11/2009	Spartanburg, SC, USA	I Girders	Truck	-
62	Indianapolis	9/22/2009	Indianapolis, IN, USA	I Girders	Tanker	GPL
63	Port St. Lucie	1/7/2010	Port St. Lucie, FL, USA	I Girders	Truck	Tyres
64	Atterbury Bridge	3/10/2010	Johannesbourg, South Africa	I Girders	Truck	Iron Rods
65	Brooklyn Bridge Mar. 10	3/14/2010	New York, NY, USA	Suspension	Car	-
66	Jose Urquiza	3/29/2010	Entre Rios, Argentina	Cable-Stayed	Truck	Tyres
67	Ballard bridge	5/5/2010	Seattle, WA, USA	I Girders	Storage	-
68	Frankenlust township bridge	6/21/2010	Frankenlust, MI, USA	Truss	Arson	-
69	Guokeng Town	6/26/2010	China	Box Girders	Tanker	Gasoline

Code	Identificative Name	Date of incident	Location	Structural System	Ignition Source	Type of Combustible
70	Puente de Ventas	8/11/2010	Madrid, España	Box Girders	Storage	-
71	Dismal Bridge	9/10/2010	Alexandria, Tenesee, USA	I Girders	Storage	Debris
72	Eastex Freeway with North Loop	9/12/2010	Houston, TX, USA	I Girders	Tanker	Gasoline
73	Harlem River Bridge	9/20/2010	New York, NY, USA	Truss	Electrical	-
74	Puente del desdoblamiento	3/6/2011	Ceuta, España	I Girders	Storage	-
75	Gilmore Bridge	3/18/2011	Cambridge, MA ,USA	I Girders	Storage	-
76	i-30 in forth worth	3/28/2011	Forth Worth, TX, USA	I Girders	Tanker	Gasoline
77	Highway M1	4/18/2011	Mill Hill, London, UK	I Girders	Storage	-
78	Xupu Bridge	5/3/2011	China	Cable-Stayed	Tanker	
79	Vaughan	5/9/2011	Vaughan, Ontario, Canada	I Girders	Car	
80	Yuqing Bridge	5/28/2011	China	Truss	Arson	
81	Lower Nazareth	5/31/2011	Lower Nazareth, PA, USA	I Girders	Car	
82	Lime Kiln Overpass	6/7/2011	Louisville, KY, USA	I Girders	Tanker	Waste Septic
83	Caogou Bridge	8/2/2011	China	Box Girders	Tanker	Gasoline
84	Auburn	9/9/2011	Auburn, WA, USA	I Girders	Car	
85	Puente sobre el canal de Castilla	9/27/2011	Palencia, España	Arch	Truck	-
86	Rosario	10/15/2011	Rosario, Argentina	I Girders	Tanker	Oil (food)
87	Vladivostok	12/12/2011	Vladivostok,Russia	Cable-Stayed	Wood Scaffolding Fire	
88	Montebello	12/14/2011	Montebello, CA, USA	I Girders	Tanker	Gasoline
89	Dormagen	2/14/2012	Dormagen, Germany	Box Girders	Storage	Plastic
90	Fallriver	2/20/2012	Fallriver, MA, USA	I Girders	Truck	-
91	Burbank	4/8/2012	Burbank, CA, USA	I Girders	Tanker	Gasoline
92	Brooklyn Bridge Jun. 12	6/1/2012	New York, NY, USA	Suspension	Car	-
93	A7 in Elche	6/21/2012	Elche, España	Box Girders	Truck	-
94	Robbinsville	10/3/2012	Robbinsville, NJ, USA	I Girders	Tanker	Diesel
95	Pont du Mathilde	10/29/2012	Rouen, France	Box Girders	Tanker	Diesel
96	Puente de Ventas	11/21/2012	Madrid, España	Box Girders	Storage	-
97	Queensboro Bridge Jan. 2013	1/9/2013	New York, NY, USA	Truss	Car	-
98	Puente Santa Rosa	1/24/2013	Lima, Peru	I Girders	Electrical Problem	-
99	North Little Rock	3/7/2013	North Little, AK, USA	I Girders	Truck	-
100	Queensboro Bridge Apr. 2013	4/8/2013	New York, NY, USA	Truss	Tanker	Oxygen
101	Millersville	4/30/2013	Millersville, TN, USA	I Girders	Truck	Silica Pellets
102	Harrisburg (1)	5/9/2013	Harrisburg, PA, USA	I Girders	Tanker	Diesel
103	Harrisburg (2)	5/9/2013	Harrisburg, PA, USA	I Girders	Tanker	Diesel
104	Viaduct San Saba	5/19/2013	San Saba, TX, USA	Truss	Unknown	-
105	Brooklyn Bridge Jul. 13	7/3/2013	New York, NY, USA	Suspension	Car	-

Code	Identificative Name	Date of incident	Location	Structural System	Ignition Source	Type of Combustible
106	Whites Bridge	7/7/2013	Smyrna, MI, USA	Covered / Truss	Arson	-
107	Elysian Park	7/13/2013	Glendale, CA, USA	Box Girders	Tanker	Gasoline
108	Castellammare di Stabia	7/14/2013	Castellammare di Stabia, Italia	Box Girders	Storage	-
109	Bay Bridge	8/5/2013	San Francisco, CA, USA	Box Girders	Truck	Grocery
110	Puente del Arenal	8/7/2013	Cordoba, España	Box Girders	Storage	Forest Waste
111	Queensboro Bridge Aug. 2013	8/16/2013	New York, NY, USA	Truss	Truck	-
112	Queensboro Bridge Sep. 2013	9/2/2013	New York, NY, USA	Truss	Truck	-
113	Commerce	10/27/2013	Commerce, CA, USA	I Girders	Tanker	Crude Oil
114	James Street Swing Bridge	10/29/2013	Thunder Bay, Canada	Truss	Unknown	
115	Sweetwater	11/1/2013	Sweetwater, TX, USA	I Girders	Truck	
116	Pasarela F1	11/11/2013	Valencia, España	Truss	Storage	
117	Fengyu	11/27/2013	Chongqing, China	Covered / Truss	Unknown	
118	Sanguenay's Dubuc Bridge	12/9/2013	Sanguenay, Montreal, Canada	Box Girders	Pillar Scaffolding	
119	Valdosta	12/29/2013	Valdosta, GA, USA	I Girders	Truck	Grocery
120	Davison Township	1/2/2014	Davison Township, MI, USA	I Girders	Tanker	Crude Oil
121	Spilimbergo	1/14/2014	Córdoba, Argentina	I Girders	Tanker	Diesel
122	El Cairo	2/11/2014	El Cairo, Egipto	I Girders	Cylinder Gas Explode	
123	Belle Vernon Bridge	3/31/2014	Belle Vernon, PA, USA	Arch	Truck	
124	Grand Rapids	4/3/2014	Grand Rapids, MI, USA	I Girders	Car	
125	Zakim Bridge	4/21/2014	Boston, MA, USA	Cable-Stayed	Truck	Grocery
126	Hesperia	5/5/2014	Hesperia, CA , USA	I Girders	Wood Scaffolding Fire	
127	West Werkeley	5/7/2014	West Berkely, CA, USA	Box Girders	Storage	Homeless
128	Chesapeake Bay	5/19/2014	Sandy Point, MD, USA	Truss	Truck	
129	General W.K. Wilson Jr. Bridge	5/22/2014	Baldwin County, Alabama, USA	I Girders	Truck	Petroleum
130	Bartow	7/22/2014	Bartow, West Virginia, USA	I Girders	Tanker	Diesel
131	Bayway ramp	7/31/2014	Mobile, Alabama, USA	I Girders	Tanker	Diesel
132	Franklin (I)	8/15/2014	Franklin, Tenesee, USA	I Girders	Tanker	Gasoline
133	Pulaski Skyway	8/15/2014	Jersey, New Jersey, USA	Truss	Other	
134	Franklin (II)	8/15/2014	Franklin, Tenesee, USA	I Girders	Tanker	Gasoline
135	I-76, Ohio	10/11/2014	Norton, Ohio, USA	I Girders	Truck	
136	Ibadan	10/12/2014	Ibadan, Nigeria	Box Girders	Tanker	
137	Hagerstown	10/17/2014	Hagerstown, Maryland, USA	I Girders	Truck	Paper
138	Delville Covered Bridge	11/3/2014	Wheatfield Township, Pennsylvannia, USA	Truss	Arson	
139	Papamoa Bridge	11/21/2014	Papamoa, New Zealand	Box Girders	Storage	Plastic
140	I-65 Franklin	12/28/2014	Franklin, Tenesee, USA	I Girders	Truck	

Code	Identificative Name	Date of incident	Location	Structural System	Ignition Source	Type of Combustible
141	Route 10, LA	1/13/2015	East Los Angeles, California, USA	Box Girders	Truck	
142	I-30, Macarthur boulevard	2/10/2015	Dallas, TX, USA	I Girders	Truck	Styrofoam, cupboards
143	Lazienkovski Bridge	2/16/2015	Warsaw, Poland	Box Girders	Storage	Wood
144	Walt Whitman	3/7/2015	New Jersey, USA	Suspension	Car	
145	Annapolis	4/1/2015	Annapolis, Baltimore, USA	I Girders	Storage	Homeless
146	Ambassador Bridge	4/15/2015	Detroit, MI, USA	Truss	Truck	
147	Detroit	5/26/2015	Detroit, MI, USA	I Girders	Tanker	Gasoline
148	M4 Sudáfrica	6/5/2015	Kwazulu-Natal, Sudáfrica	I Girders	Storage	Wood
149	Coronado Bridge	6/5/2015	San Diego, California, USA	I Girders	Car	
150	I-270/I-70	7/1/2015	Columbus,Ohio,USA	Box Girders	Tanker	Ethanol
151	East London	7/1/2015	Londres, Gran Bretaña	Box Girders	Storage	Cars and Tyres
152	Meriden	7/13/2015	Meriden, connecticut. USA	I Girders	Tanker	Oil (food)
153	Delta Covered Bridge	xx/08/2003	Delta, IA, USA	Covered / Truss	Arson	-
154	Washington County	xx/11/2004	Whasington County, OR, USA	I Girders	Car	-

APPENDIX D: NEW YORK STATE – DEPARTMENT OF HOMELAND SECURITY & EMERGENCY SERVICES DATABASE (2020)

Case	Date	Bridge	NFIRS Type	Alarm Date	Arrival Date	Last Unit Clear Date
1	12/3/2005	Brooklyn Bridge	131	Dec/03/2005 02:52:23 AM	Dec/03/2005 02:59:13 AM	Dec/03/2005 03:33:56 AM
2	12/21/2007	Brooklyn Bridge	131	Dec/21/2007 05:52:01 PM	Dec/21/2007 05:57:02 PM	Dec/21/2007 06:08:43 PM
3	8/29/2005	Brooklyn Bridge	131	Aug/29/2005 09:08:08 PM	Aug/29/2005 09:14:01 PM	Aug/29/2005 09:20:13 PM
4	12/5/2003	Brooklyn Bridge	131	Dec/05/2003 07:14:00 AM	Dec/05/2003 07:22:13 AM	Dec/05/2003 08:22:46 AM
5	12/23/2004	Brooklyn Bridge	131	Dec/23/2004 07:08:41 PM	Dec/23/2004 07:16:04 PM	Dec/23/2004 07:32:41 PM
6	2/19/2016	George Washington Bridge	131	Feb/19/2016 10:38:01 PM	Feb/19/2016 10:44:00 PM	Feb/19/2016 11:01:37 PM
7	9/1/2015	George Washington Bridge	131	Sep/01/2015 05:00:44 PM	Sep/01/2015 05:08:10 PM	Sep/01/2015 05:30:43 PM
8	6/19/2016	George Washington Bridge	131	Jun/19/2016 12:14:34 PM	Jun/19/2016 12:19:03 PM	Jun/19/2016 01:28:43 PM
9	2/4/2003	Manhattan Bridge	112	Feb/04/2003 04:16:35 AM	Feb/04/2003 04:21:13 AM	Feb/04/2003 04:58:14 AM
10	3/8/2003	Manhattan Bridge	131	Mar/08/2003 04:35:32 PM	Mar/08/2003 04:39:54 PM	Mar/08/2003 04:59:15 PM
11	4/8/2004	Manhattan Bridge	131	Apr/08/2004 01:06:57 PM	Apr/08/2004 01:10:41 PM	Apr/08/2004 01:26:00 PM
12	5/3/2014	RFK Bridge	131	May/03/2014 01:39:31 AM	May/03/2014 01:44:54 AM	May/03/2014 02:31:11 AM
13	3/28/2016	RFK Bridge	131	Mar/28/2016 08:55:44 PM	Mar/28/2016 08:58:52 PM	Mar/28/2016 09:22:22 PM
14	11/21/2015	RFK Bridge	131	Nov/21/2015 07:07:52 AM	Nov/21/2015 07:13:45 AM	Nov/21/2015 07:45:44 AM
15	4/9/2013	RFK Bridge	131	Apr/09/2013 05:43:55 PM	Apr/09/2013 05:49:58 PM	Apr/09/2013 06:07:57 PM
16	10/13/2018	RFK Bridge	131	Oct/13/2018 07:39:41 PM	Oct/13/2018 07:45:59 PM	Oct/13/2018 07:59:16 PM
17	4/29/2010	RFK Bridge	131	Apr/29/2010 12:33:20 AM	Apr/29/2010 12:39:02 AM	Apr/29/2010 12:48:02 AM
18	9/17/2014	RFK Bridge	131	Sep/17/2014 04:57:40 PM	Sep/17/2014 05:05:33 PM	Sep/17/2014 05:20:05 PM
19	2/24/2013	Throgs Neck Bridge	131	Feb/24/2013 01:40:32 AM	Feb/24/2013 01:46:25 AM	Feb/24/2013 01:53:23 AM
20	6/26/2005	Triborough Bridge	131	Jun/26/2005 03:51:30 PM	Jun/26/2005 03:57:48 PM	Jun/26/2005 04:24:41 PM
21	4/23/2004	Triborough Bridge	131	Apr/23/2004 11:35:18 AM	Apr/23/2004 11:48:32 AM	Apr/23/2004 01:13:14 PM
22	9/24/2003	Triborough Bridge	131	Sep/24/2003 08:34:35 AM	Sep/24/2003 08:39:38 AM	Sep/24/2003 09:12:43 AM
23	2/11/2005	Triborough Bridge	131	Feb/11/2005 06:13:24 AM	Feb/11/2005 06:21:49 AM	Feb/11/2005 06:40:43 AM
24	1/25/2004	Triborough Bridge	131	Jan/25/2004 10:10:07 PM	Jan/25/2004 10:19:10 PM	Jan/25/2004 10:30:11 PM
25	3/4/2008	Triborough Bridge	131	Mar/04/2008 08:47:26 PM	Mar/04/2008 08:54:19 PM	Mar/04/2008 09:45:10 PM
26	11/9/2006	Verrazano-Narrows Bridge	131	Nov/09/2006 06:20:46 PM	Nov/09/2006 06:27:37 PM	Nov/09/2006 07:04:55 PM
27	7/24/2019	Verrazano-Narrows Bridge	131	Jul/24/2019 07:08:59 AM	Jul/24/2019 07:15:27 AM	Jul/24/2019 08:16:11 AM
28	3/19/2010	Verrazano-Narrows Bridge	131	Mar/19/2010 03:23:06 PM	Mar/19/2010 03:28:51 PM	Mar/19/2010 03:51:06 PM
29	3/10/2005	Verrazano-Narrows Bridge	131	Mar/10/2005 05:58:38 PM	Mar/10/2005 06:03:06 PM	Mar/10/2005 06:18:31 PM
30	12/28/2002	Verrazano-Narrows Bridge	131	Dec/28/2002 07:24:04 PM	Dec/28/2002 07:28:35 PM	Dec/28/2002 07:57:09 PM
31	10/2/2018	Verrazano-Narrows Bridge	131	Oct/02/2018 06:30:52 AM	Oct/02/2018 06:37:30 AM	Oct/02/2018 07:14:37 AM
32	3/29/2005	Verrazano-Narrows Bridge	131	Mar/29/2005 10:50:52 PM	Mar/29/2005 10:55:45 PM	Mar/29/2005 11:21:22 PM

Case	Date	Bridge	NFIRS Type	Alarm Date	Arrival Date	Last Unit Clear Date
33	3/6/2006	Verrazano-Narrows Bridge	131	Mar/06/2006 05:17:20 PM	Mar/06/2006 05:23:07 PM	Mar/06/2006 05:39:48 PM
34	12/14/2003	Verrazano-Narrows Bridge	131	Dec/14/2003 04:04:10 PM	Dec/14/2003 04:12:00 PM	Dec/14/2003 04:23:26 PM
35	9/26/2004	Verrazano-Narrows Bridge	131	Sep/26/2004 04:17:23 AM	Sep/26/2004 04:22:39 AM	Sep/26/2004 05:03:33 AM
36	3/21/2004	Verrazano-Narrows Bridge	131	Mar/21/2004 07:04:50 PM	Mar/21/2004 07:09:22 PM	Mar/21/2004 07:26:08 PM
37	9/5/2019	Verrazano-Narrows Bridge	131	Sep/05/2019 09:58:06 AM	Sep/05/2019 10:04:54 AM	Sep/05/2019 10:29:25 AM
38	11/13/2009	Verrazano-Narrows Bridge	131	Nov/13/2009 03:55:59 AM	Nov/13/2009 04:00:18 AM	Nov/13/2009 04:31:23 AM
39	7/20/2003	Verrazano-Narrows Bridge	131	Jul/20/2003 07:36:48 AM	Jul/20/2003 07:41:12 AM	Jul/20/2003 07:49:01 AM
40	1/25/2004	Verrazano-Narrows Bridge	131	Jan/25/2004 08:17:34 AM	Jan/25/2004 08:22:15 AM	Jan/25/2004 08:34:15 AM
41	8/30/2003	Verrazano-Narrows Bridge	131	Aug/30/2003 09:46:56 PM	Aug/30/2003 09:52:01 PM	Aug/30/2003 10:20:51 PM
42	6/12/2019	Whitestone Bridge	131	Jun/12/2019 04:41:26 AM	Jun/12/2019 04:47:31 AM	Jun/12/2019 05:22:35 AM
43	6/22/2019	Whitestone Bridge	131	Jun/22/2019 10:16:36 PM	Jun/22/2019 10:22:58 PM	Jun/22/2019 11:14:12 PM
44	12/30/2017	Brooklyn Bridge	131	Dec/30/2017 01:21:40 AM	Dec/30/2017 01:26:36 AM	Dec/30/2017 01:59:28 AM
45	3/14/2010	Brooklyn Bridge	131	Mar/14/2010 03:45:47 PM	Mar/14/2010 03:51:48 PM	Mar/14/2010 04:47:24 PM
46	6/30/2005	Brooklyn Bridge	131	Jun/30/2005 03:36:12 PM	Jun/30/2005 03:42:21 PM	Jun/30/2005 04:19:47 PM
47	8/28/2005	Brooklyn Bridge	131	Aug/28/2005 11:21:42 AM	Aug/28/2005 11:28:15 AM	Aug/28/2005 12:09:05 PM
48	11/21/2018	Brooklyn Bridge	131	Nov/21/2018 07:14:52 AM	Nov/21/2018 07:20:18 AM	Nov/21/2018 01:04:28 PM
49	7/14/2004	Brooklyn Bridge	131	Jul/14/2004 01:34:22 PM	Jul/14/2004 01:40:12 PM	Jul/14/2004 02:01:27 PM
50	3/14/2012	Brooklyn Bridge	131	Mar/14/2012 08:51:06 AM	Mar/14/2012 08:55:47 AM	Mar/14/2012 09:30:47 AM
51	3/2/2003	Brooklyn Bridge	131	Mar/02/2003 11:21:42 PM	Mar/02/2003 11:27:10 PM	Mar/02/2003 11:40:04 PM
52	4/14/2018	Brooklyn Bridge	131	Apr/14/2018 01:48:57 PM	Apr/14/2018 01:54:00 PM	Apr/14/2018 02:15:52 PM
53	1/1/2005	Brooklyn Bridge	131	Jan/01/2005 04:27:32 AM	Jan/01/2005 04:34:04 AM	Jan/01/2005 05:08:25 AM
54	6/8/2005	Brooklyn Bridge	131	Jun/08/2005 03:59:22 PM	Jun/08/2005 04:05:58 PM	Jun/08/2005 04:38:28 PM
55	5/26/2018	Brooklyn Bridge	131	May/26/2018 06:31:12 PM	May/26/2018 06:36:14 PM	May/26/2018 07:41:42 PM
56	9/23/2004	Brooklyn Bridge	131	Sep/23/2004 11:26:34 PM	Sep/23/2004 11:31:28 PM	Sep/23/2004 11:47:27 PM
57	12/11/2006	Brooklyn Bridge	131	Dec/11/2006 09:03:58 PM	Dec/11/2006 09:09:18 PM	Dec/11/2006 09:43:16 PM
58	12/2/2006	Brooklyn Bridge	131	Dec/02/2006 09:05:37 PM	Dec/02/2006 09:10:42 PM	Dec/02/2006 09:52:32 PM
59	7/3/2013	Brooklyn Bridge	131	Jul/03/2013 07:21:51 AM	Jul/03/2013 07:26:51 AM	Jul/03/2013 08:25:13 AM
60	9/28/2012	Brooklyn Bridge	131	Sep/28/2012 08:23:16 AM	Sep/28/2012 08:28:55 AM	Sep/28/2012 09:35:09 AM
61	7/21/2012	Brooklyn Bridge	131	Jul/21/2012 04:22:47 PM	Jul/21/2012 04:27:53 PM	Jul/21/2012 05:25:18 PM
62	12/20/2002	Brooklyn Bridge	131	Dec/20/2002 12:01:57 AM	Dec/20/2002 12:07:30 AM	Dec/20/2002 12:45:34 AM
63	5/25/2013	Brooklyn Bridge	131	May/25/2013 05:06:00 PM	May/25/2013 05:10:22 PM	May/25/2013 05:49:30 PM
64	5/31/2012	Brooklyn Bridge	131	May/31/2012 09:13:14 PM	May/31/2012 09:16:18 PM	May/31/2012 11:15:30 PM
65	12/10/2009	Brooklyn Bridge	131	Dec/10/2009 06:37:08 AM	Dec/10/2009 06:42:55 AM	Dec/10/2009 07:09:00 AM
66	8/17/2005	Brooklyn Bridge	131	Aug/17/2005 04:55:11 PM	Aug/17/2005 05:03:56 PM	Aug/17/2005 05:36:41 PM
67	5/24/2019	Brooklyn Bridge	131	May/24/2019 04:06:43 PM	May/24/2019 04:09:15 PM	May/24/2019 04:57:54 PM
68	2/26/2011	Brooklyn Bridge	131	Feb/26/2011 09:21:37 AM	Feb/26/2011 09:25:58 AM	Feb/26/2011 10:02:50 AM

Case	Date	Bridge	NFIRS Type	Alarm Date	Arrival Date	Last Unit Clear Date
69	7/22/2017	Brooklyn Bridge	131	Jul/22/2017 09:38:14 PM	Jul/22/2017 09:42:22 PM	Jul/22/2017 10:34:04 PM
70	6/18/2010	George Washington Bridge	131	Jun/18/2010 04:25:25 PM	Jun/18/2010 04:35:32 PM	Jun/18/2010 05:01:34 PM
71	11/17/2009	George Washington Bridge	131	Nov/17/2009 06:04:51 PM	Nov/17/2009 06:11:04 PM	Nov/17/2009 06:46:17 PM
72	11/2/2004	George Washington Bridge	131	Nov/02/2004 03:47:31 AM	Nov/02/2004 03:54:31 AM	Nov/02/2004 04:17:32 AM
73	3/8/2012	George Washington Bridge	131	Mar/08/2012 04:23:24 AM	Mar/08/2012 04:29:44 AM	Mar/08/2012 05:07:01 AM
74	9/22/2005	George Washington Bridge	131	Sep/22/2005 06:14:26 PM	Sep/22/2005 06:33:11 PM	Sep/22/2005 08:07:22 PM
75	6/17/2006	George Washington Bridge	131	Jun/17/2006 06:33:22 PM	Jun/17/2006 06:43:48 PM	Jun/17/2006 07:21:02 PM
76	5/1/2004	George Washington Bridge	131	May/01/2004 05:19:58 PM	May/01/2004 05:28:21 PM	May/01/2004 06:06:00 PM
77	6/22/2003	George Washington Bridge	131	Jun/22/2003 01:44:46 AM	Jun/22/2003 01:49:48 AM	Jun/22/2003 02:15:33 AM
78	1/14/2011	George Washington Bridge	131	Jan/14/2011 06:02:40 PM	Jan/14/2011 06:17:22 PM	Jan/14/2011 07:02:46 PM
79	3/7/2008	Manhattan Bridge	131	Mar/07/2008 01:17:31 AM	Mar/07/2008 01:23:13 AM	Mar/07/2008 02:10:05 AM
80	12/9/2012	Manhattan Bridge	131	Dec/09/2012 09:33:02 PM	Dec/09/2012 09:36:06 PM	Dec/09/2012 09:50:28 PM
81	1/31/2018	Manhattan Bridge	131	Jan/31/2018 06:18:31 AM	Jan/31/2018 06:24:24 AM	Jan/31/2018 07:29:46 AM
82	2/7/2019	Manhattan Bridge	131	Feb/07/2019 02:14:03 AM	Feb/07/2019 02:20:36 AM	Feb/07/2019 03:20:37 AM
83	10/20/2013	Manhattan Bridge	131	Oct/20/2013 04:23:17 AM	Oct/20/2013 04:28:27 AM	Oct/20/2013 05:31:31 AM
84	1/24/2017	Manhattan Bridge	131	Jan/24/2017 01:16:24 PM	Jan/24/2017 01:23:05 PM	Jan/24/2017 03:08:24 PM
85	9/29/2015	Manhattan Bridge	131	Sep/29/2015 04:00:12 PM	Sep/29/2015 04:04:16 PM	Sep/29/2015 04:15:47 PM
86	9/26/2004	Manhattan Bridge	131	Sep/26/2004 08:25:35 PM	Sep/26/2004 08:32:13 PM	Sep/26/2004 08:47:17 PM
87	10/25/2009	Manhattan Bridge	131	Oct/25/2009 11:38:39 PM	Oct/25/2009 11:43:17 PM	Oct/25/2009 11:55:37 PM
88	10/21/2004	Manhattan Bridge	131	Oct/21/2004 03:07:32 PM	Oct/21/2004 03:11:06 PM	Oct/21/2004 03:34:02 PM
89	8/31/2003	Manhattan Bridge	131	Aug/31/2003 03:40:10 PM	Aug/31/2003 03:44:49 PM	Aug/31/2003 04:20:14 PM
90	2/11/2011	RFK Bridge	131	Feb/11/2011 06:03:14 AM	Feb/11/2011 06:10:48 AM	Feb/11/2011 06:24:11 AM
91	6/30/2010	RFK Bridge	131	Jun/30/2010 11:13:40 AM	Jun/30/2010 11:19:44 AM	Jun/30/2010 12:25:20 PM
92	5/5/2016	RFK Bridge	131	May/05/2016 07:21:24 AM	May/05/2016 07:29:11 AM	May/05/2016 07:41:21 AM
93	1/16/2014	RFK Bridge	131	Jan/16/2014 01:02:02 AM	Jan/16/2014 01:08:30 AM	Jan/16/2014 01:27:41 AM
94	8/24/2010	RFK Bridge	131	Aug/24/2010 06:36:12 AM	Aug/24/2010 06:43:18 AM	Aug/24/2010 06:47:49 AM
95	5/24/2013	RFK Bridge	131	May/24/2013 06:02:05 PM	May/24/2013 06:10:14 PM	May/24/2013 06:17:21 PM
96	8/29/2018	RFK Bridge	131	Aug/29/2018 05:33:12 PM	Aug/29/2018 05:38:16 PM	Aug/29/2018 06:53:45 PM
97	4/22/2013	RFK Bridge	131	Apr/22/2013 03:34:56 PM	Apr/22/2013 03:40:35 PM	Apr/22/2013 04:18:34 PM
98	9/28/2019	RFK Bridge	131	Sep/28/2019 07:10:03 AM	Sep/28/2019 07:15:54 AM	Sep/28/2019 07:53:17 AM
99	5/29/2018	RFK Bridge	131	May/29/2018 09:19:42 PM	May/29/2018 09:24:28 PM	May/29/2018 09:43:04 PM
100	4/23/2011	RFK Bridge	131	Apr/23/2011 12:51:26 PM	Apr/23/2011 12:58:08 PM	Apr/23/2011 01:08:40 PM
101	3/23/2015	RFK Bridge	131	Mar/23/2015 01:41:33 PM	Mar/23/2015 01:47:39 PM	Mar/23/2015 02:38:40 PM
102	2/29/2016	RFK Bridge	131	Feb/29/2016 10:08:48 AM	Feb/29/2016 10:08:48 AM	Feb/29/2016 10:28:33 AM
103	5/12/2012	RFK Bridge	131	May/12/2012 12:18:44 PM	May/12/2012 12:23:21 PM	May/12/2012 12:51:14 PM
104	7/24/2015	RFKBridge	131	Jul/24/2015 09:39:32 PM	Jul/24/2015 09:42:06 PM	Jul/24/2015 10:05:19 PM

Case	Date	Bridge	NFIRS Type	Alarm Date	Arrival Date	Last Unit Clear Date
105	7/21/2013	Throgs Neck Bridge	131	Jul/21/2013 10:10:12 PM	Jul/21/2013 10:14:49 PM	Jul/21/2013 10:24:59 PM
106	4/5/2004	Throgs Neck Bridge	131	Apr/05/2004 12:11:21 PM	Apr/05/2004 12:17:13 PM	Apr/05/2004 12:51:38 PM
107	5/22/2004	Throgs Neck Bridge	131	May/22/2004 07:22:05 AM	May/22/2004 07:28:48 AM	May/22/2004 07:42:35 AM
108	12/18/2005	Throgs Neck Bridge	131	Dec/18/2005 12:14:28 PM	Dec/18/2005 12:21:13 PM	Dec/18/2005 12:32:14 PM
109	2/1/2004	Throgs Neck Bridge	131	Feb/01/2004 06:05:58 PM	Feb/01/2004 06:12:27 PM	Feb/01/2004 06:58:27 PM
110	5/15/2010	Throgs Neck Bridge	131	May/15/2010 11:18:21 AM	May/15/2010 11:30:54 AM	May/15/2010 12:14:46 PM
111	12/6/2008	Throgs Neck Bridge	131	Dec/06/2008 06:40:36 PM	Dec/06/2008 06:47:44 PM	Dec/06/2008 07:32:58 PM
112	3/14/2019	Throgs Neck Bridge	131	Mar/14/2019 07:27:45 PM	Mar/14/2019 07:37:17 PM	Mar/14/2019 09:00:06 PM
113	10/30/2003	Throgs Neck Bridge	131	Oct/30/2003 02:38:08 AM	Oct/30/2003 02:46:54 AM	Oct/30/2003 03:16:06 AM
114	6/16/2019	Throgs Neck Bridge	131	Jun/16/2019 10:07:10 PM	Jun/16/2019 10:13:29 PM	Jun/16/2019 10:38:51 PM
115	4/23/2018	Throgs Neck Bridge	131	Apr/23/2018 01:57:10 PM	Apr/23/2018 02:07:31 PM	Apr/23/2018 02:47:42 PM
116	6/19/2005	Throgs Neck Bridge	131	Jun/19/2005 10:13:24 PM	Jun/19/2005 10:22:35 PM	Jun/19/2005 10:56:47 PM
117	5/16/2004	Throgs Neck Bridge	131	May/16/2004 01:15:28 PM	May/16/2004 01:22:12 PM	May/16/2004 02:06:12 PM
118	11/13/2012	Throgs Neck Bridge	131	Nov/13/2012 12:35:27 PM	Nov/13/2012 12:45:40 PM	Nov/13/2012 12:53:50 PM
119	5/3/2015	Throgs Neck Bridge	131	May/03/2015 08:13:29 AM	May/03/2015 08:19:38 AM	May/03/2015 08:38:12 AM
120	8/1/2011	Throgs Neck Bridge	131	Aug/01/2011 04:56:48 PM	Aug/01/2011 05:12:59 PM	Aug/01/2011 06:31:26 PM
121	1/13/2010	Throgs Neck Bridge	131	Jan/13/2010 02:45:59 PM	Jan/13/2010 02:50:47 PM	Jan/13/2010 03:54:02 PM
122	9/3/2005	Triborough Bridge	131	Sep/03/2005 12:46:53 PM	Sep/03/2005 12:54:55 PM	Sep/03/2005 01:07:35 PM
123	6/1/2005	Triborough Bridge	131	Jun/01/2005 09:29:52 PM	Jun/01/2005 09:37:02 PM	Jun/01/2005 09:56:20 PM
124	1/23/2006	Triborough Bridge	131	Jan/23/2006 08:03:59 AM	Jan/23/2006 08:11:17 AM	Jan/23/2006 08:50:17 AM
125	11/30/2002	Triborough Bridge	131	Nov/30/2002 08:23:24 AM	Nov/30/2002 08:29:12 AM	Nov/30/2002 08:39:09 AM
126	2/20/2006	Triborough Bridge	131	Feb/20/2006 07:06:23 AM	Feb/20/2006 07:13:45 AM	Feb/20/2006 07:25:30 AM
127	2/12/2004	Triborough Bridge	131	Feb/12/2004 11:21:44 AM	Feb/12/2004 11:26:01 AM	Feb/12/2004 11:42:34 AM
128	2/9/2005	Triborough Bridge	131	Feb/09/2005 08:33:11 AM	Feb/09/2005 08:39:28 AM	Feb/09/2005 09:05:52 AM
129	5/30/2005	Triborough Bridge	131	May/30/2005 08:45:04 AM	May/30/2005 08:52:25 AM	May/30/2005 09:19:38 AM
130	7/4/2005	Triborough Bridge	131	Jul/04/2005 10:55:04 PM	Jul/04/2005 10:55:04 PM	Jul/04/2005 11:21:09 PM
131	8/19/2005	Triborough Bridge	131	Aug/19/2005 05:51:10 PM	Aug/19/2005 05:57:34 PM	Aug/19/2005 06:08:57 PM
132	5/11/2005	Triborough Bridge	131	May/11/2005 06:51:15 PM	May/11/2005 06:57:04 PM	May/11/2005 07:45:23 PM
133	10/26/2008	Triborough Bridge	131	Oct/26/2008 09:04:38 PM	Oct/26/2008 09:10:07 PM	Oct/26/2008 09:36:41 PM
134	1/22/2006	Triborough Bridge	131	Jan/22/2006 04:53:32 AM	Jan/22/2006 05:10:21 AM	Jan/22/2006 05:13:26 AM
135	10/9/2006	Triborough Bridge	131	Oct/09/2006 12:09:20 PM	Oct/09/2006 12:15:29 PM	Oct/09/2006 12:34:43 PM
136	11/6/2006	Triborough Bridge	131	Nov/06/2006 11:30:59 PM	Nov/06/2006 11:37:23 PM	Nov/06/2006 11:44:00 PM
137	5/11/2005	Triborough Bridge	131	May/11/2005 07:46:48 PM	May/11/2005 07:53:34 PM	May/11/2005 08:12:59 PM
138	1/21/2003	Triborough Bridge	131	Jan/21/2003 08:58:06 AM	Jan/21/2003 09:04:12 AM	Jan/21/2003 09:19:05 AM
139	4/14/2004	Triborough Bridge	131	Apr/14/2004 12:51:14 PM	Apr/14/2004 12:58:47 PM	Apr/14/2004 01:20:21 PM
140	5/31/2003	Triborough Bridge	131	May/31/2003 02:42:01 AM	May/31/2003 02:46:44 AM	May/31/2003 03:02:52 AM

Case	Date	Bridge	NFIRS Type	Alarm Date	Arrival Date	Last Unit Clear Date
141	3/7/2005	Triborough Bridge	131	Mar/07/2005 09:54:26 PM	Mar/07/2005 10:01:46 PM	Mar/07/2005 10:26:28 PM
142	2/25/2011	Verrazano-Narrows Bridge	131	Feb/25/2011 07:57:43 AM	Feb/25/2011 08:03:04 AM	Feb/25/2011 08:11:59 AM
143	11/20/2009	Verrazano-Narrows Bridge	131	Nov/20/2009 10:35:46 AM	Nov/20/2009 10:38:54 AM	Nov/20/2009 11:11:46 AM
144	1/8/2015	Verrazano-Narrows Bridge	131	Jan/08/2015 01:25:07 PM	Jan/08/2015 01:28:48 PM	Jan/08/2015 02:00:34 PM
145	12/26/2002	Verrazano-Narrows Bridge	131	Dec/26/2002 07:14:45 AM	Dec/26/2002 07:20:27 AM	Dec/26/2002 07:32:02 AM
146	10/17/2006	Verrazano-Narrows Bridge	131	Oct/17/2006 04:24:51 AM	Oct/17/2006 04:30:34 AM	Oct/17/2006 04:43:00 AM
147	5/26/2014	Verrazano-Narrows Bridge	131	May/26/2014 02:50:06 PM	May/26/2014 02:54:46 PM	May/26/2014 03:51:54 PM
148	6/1/2004	Verrazano-Narrows Bridge	131	Jun/01/2004 08:33:18 PM	Jun/01/2004 08:38:30 PM	Jun/01/2004 08:57:59 PM
149	11/1/2003	Verrazano-Narrows Bridge	131	Nov/01/2003 03:17:41 PM	Nov/01/2003 03:21:40 PM	Nov/01/2003 03:29:53 PM
150	9/18/2005	Verrazano-Narrows Bridge	131	Sep/18/2005 06:55:55 AM	Sep/18/2005 06:58:20 AM	Sep/18/2005 07:22:26 AM
151	6/17/2015	Verrazano-Narrows Bridge	131	Jun/17/2015 10:57:22 PM	Jun/17/2015 11:01:40 PM	Jun/17/2015 11:33:25 PM
152	12/22/2015	Verrazano-Narrows Bridge	131	Dec/22/2015 05:45:40 PM	Dec/22/2015 05:50:20 PM	Dec/22/2015 06:38:26 PM
153	9/10/2016	Verrazano-Narrows Bridge	131	Sep/10/2016 12:17:58 PM	Sep/10/2016 12:23:07 PM	Sep/10/2016 01:28:51 PM
154	7/7/2019	Verrazano-Narrows Bridge	131	Jul/07/2019 07:12:45 PM	Jul/07/2019 07:17:46 PM	Jul/07/2019 07:44:12 PM
155	8/28/2017	Verrazano-Narrows Bridge	131	Aug/28/2017 09:24:05 AM	Aug/28/2017 09:29:24 AM	Aug/28/2017 10:09:13 AM
156	7/24/2019	Verrazano-Narrows Bridge	131	Jul/24/2019 08:13:54 AM	Jul/24/2019 08:17:46 AM	Jul/24/2019 09:21:42 AM
157	10/29/2006	Verrazano-Narrows Bridge	131	Oct/29/2006 05:13:32 PM	Oct/29/2006 05:20:01 PM	Oct/29/2006 06:08:35 PM
158	10/6/2003	Verrazano-Narrows Bridge	131	Oct/06/2003 12:54:48 AM	Oct/06/2003 12:58:56 AM	Oct/06/2003 01:30:03 AM
159	6/20/2003	Verrazano-Narrows Bridge	131	Jun/20/2003 03:28:40 PM	Jun/20/2003 03:34:43 PM	Jun/20/2003 03:47:40 PM
160	11/26/2015	Verrazano-Narrows Bridge	131	Nov/26/2015 11:56:57 AM	Nov/26/2015 12:00:39 PM	Nov/26/2015 12:31:02 PM
161	12/8/2002	Verrazano-Narrows Bridge	131	Dec/08/2002 03:09:49 PM	Dec/08/2002 03:14:08 PM	Dec/08/2002 03:28:09 PM
162	8/8/2003	Verrazano-Narrows Bridge	131	Aug/08/2003 06:35:04 PM	Aug/08/2003 06:41:33 PM	Aug/08/2003 07:17:58 PM
163	2/12/2012	Verrazano-Narrows Bridge	131	Feb/12/2012 07:20:37 PM	Feb/12/2012 07:24:54 PM	Feb/12/2012 07:39:02 PM
164	10/27/2008	Verrazano-Narrows Bridge	131	Oct/27/2008 07:17:03 AM	Oct/27/2008 07:25:48 AM	Oct/27/2008 08:07:50 AM
165	12/4/2019	Verrazano-Narrows Bridge	131	Dec/04/2019 09:41:55 PM	Dec/04/2019 09:46:54 PM	Dec/04/2019 10:37:38 PM
166	2/29/2004	Verrazano-Narrows Bridge	131	Feb/29/2004 03:45:39 AM	Feb/29/2004 03:51:55 AM	Feb/29/2004 04:16:03 AM
167	11/9/2006	Verrazano-Narrows Bridge	131	Nov/09/2006 06:21:58 PM	Nov/09/2006 06:21:58 PM	Nov/09/2006 06:24:25 PM
168	10/8/2008	Verrazano-Narrows Bridge	131	Oct/08/2008 07:08:23 AM	Oct/08/2008 07:13:26 AM	Oct/08/2008 07:27:43 AM
169	5/9/2011	Verrazano-Narrows Bridge	131	May/09/2011 06:50:47 PM	May/09/2011 06:55:03 PM	May/09/2011 07:12:50 PM
170	11/25/2018	Verrazano-Narrows Bridge	131	Nov/25/2018 12:17:19 PM	Nov/25/2018 12:17:19 PM	Nov/25/2018 12:21:08 PM
171	9/10/2015	Verrazano-Narrows Bridge	131	Sep/10/2015 06:54:23 AM	Sep/10/2015 07:01:57 AM	Sep/10/2015 07:19:45 AM
172	7/14/2005	Verrazano-Narrows Bridge	131	Jul/14/2005 12:58:59 PM	Jul/14/2005 01:05:58 PM	Jul/14/2005 02:15:34 PM
173	11/19/2009	Verrazano-Narrows Bridge	131	Nov/19/2009 06:54:37 PM	Nov/19/2009 07:00:12 PM	Nov/19/2009 07:16:20 PM
174	10/29/2006	Verrazano-Narrows Bridge	131	Oct/29/2006 05:13:32 PM	Oct/29/2006 05:20:01 PM	Oct/29/2006 06:08:35 PM
175	7/25/2002	Verrazano-Narrows Bridge	131	Jul/25/2002 06:33:56 PM	Jul/25/2002 06:39:53 PM	Jul/25/2002 07:21:47 PM
176	9/22/2011	Verrazano-Narrows Bridge	131	Sep/22/2011 04:23:16 AM	Sep/22/2011 04:28:38 AM	Sep/22/2011 04:47:33 AM

Case	Date	Bridge	NFIRS Type	Alarm Date	Arrival Date	Last Unit Clear Date
177	9/24/2002	Verrazano-Narrows Bridge	131	Sep/24/2002 07:38:48 PM	Sep/24/2002 07:43:55 PM	Sep/24/2002 08:10:38 PM
178	4/13/2012	Verrazano-Narrows Bridge	131	Apr/13/2012 06:22:37 AM	Apr/13/2012 06:29:33 AM	Apr/13/2012 06:36:08 AM
179	6/1/2013	Verrazano-Narrows Bridge	131	Jun/01/2013 01:13:52 PM	Jun/01/2013 01:19:33 PM	Jun/01/2013 01:34:19 PM
180	6/19/2012	Verrazano-Narrows Bridge	131	Jun/19/2012 06:05:08 PM	Jun/19/2012 06:10:09 PM	Jun/19/2012 06:21:17 PM
181	5/2/2011	Verrazano-Narrows Bridge	131	May/02/2011 06:00:27 AM	May/02/2011 06:07:09 AM	May/02/2011 06:22:03 AM
182	4/14/2012	Verrazano-Narrows Bridge	131	Apr/14/2012 06:17:57 PM	Apr/14/2012 06:20:31 PM	Apr/14/2012 06:47:51 PM
183	3/15/2012	Verrazano-Narrows Bridge	131	Mar/15/2012 05:47:42 PM	Mar/15/2012 05:53:16 PM	Mar/15/2012 06:23:30 PM
184	7/4/2009	Verrazano-Narrows Bridge	131	Jul/04/2009 03:03:14 PM	Jul/04/2009 03:07:28 PM	Jul/04/2009 03:20:49 PM
185	6/2/2005	Whitestone Bridge	131	Jun/02/2005 04:25:56 PM	Jun/02/2005 04:32:33 PM	Jun/02/2005 04:41:16 PM
186	10/22/2004	Whitestone Bridge	131	Oct/22/2004 10:16:00 PM	Oct/22/2004 10:21:23 PM	Oct/22/2004 10:42:54 PM
187	5/8/2004	Whitestone Bridge	131	May/08/2004 03:48:53 PM	May/08/2004 04:00:16 PM	May/08/2004 04:29:02 PM
188	11/15/2006	Whitestone Bridge	131	Nov/15/2006 12:30:33 PM	Nov/15/2006 12:37:59 PM	Nov/15/2006 01:00:00 PM
189	5/22/2017	Whitestone Bridge	131	May/22/2017 09:34:39 AM	May/22/2017 09:38:48 AM	May/22/2017 09:50:31 AM
190	11/28/2010	Whitestone Bridge	131	Nov/28/2010 09:20:31 PM	Nov/28/2010 09:28:44 PM	Nov/28/2010 09:40:37 PM
191	8/24/2003	Whitestone Bridge	131	Aug/24/2003 04:42:18 PM	Aug/24/2003 04:49:25 PM	Aug/24/2003 05:25:41 PM
192	1/24/2005	Whitestone Bridge	131	Jan/24/2005 03:58:35 PM	Jan/24/2005 04:06:15 PM	Jan/24/2005 04:25:05 PM
193	9/11/2003	Whitestone Bridge	131	Sep/11/2003 02:45:44 PM	Sep/11/2003 02:52:26 PM	Sep/11/2003 03:08:43 PM
194	10/7/2009	Whitestone Bridge	131	Oct/07/2009 10:16:30 AM	Oct/07/2009 10:22:23 AM	Oct/07/2009 10:39:21 AM
195	6/13/2017	Whitestone Bridge	131	Jun/13/2017 08:44:55 AM	Jun/13/2017 08:51:56 AM	Jun/13/2017 09:16:59 AM
196	9/11/2004	Whitestone Bridge	131	Sep/11/2004 03:04:50 AM	Sep/11/2004 03:15:02 AM	Sep/11/2004 04:05:11 AM
197	7/5/2009	Whitestone Bridge	131	Jul/05/2009 08:28:03 PM	Jul/05/2009 08:32:36 PM	Jul/05/2009 08:56:51 PM
198	8/6/2006	Whitestone Bridge	131	Aug/06/2006 12:26:02 PM	Aug/06/2006 12:33:25 PM	Aug/06/2006 12:45:27 PM
199	11/30/2012	Whitestone Bridge	131	Nov/30/2012 05:44:40 PM	Nov/30/2012 05:56:37 PM	Nov/30/2012 06:59:49 PM
200	7/14/2003	Whitestone Bridge	131	Jul/14/2003 01:50:00 AM	Jul/14/2003 01:56:56 AM	Jul/14/2003 02:30:28 AM
201	8/5/2013	Williamsburg Bridge	131	Aug/05/2013 01:47:55 PM	Aug/05/2013 01:53:23 PM	Aug/05/2013 02:39:03 PM
202	3/14/2005	Williamsburg Bridge	112	Mar/14/2005 04:31:16 PM	Mar/14/2005 04:36:22 PM	Mar/14/2005 05:17:21 PM
203	12/3/2002	Williamsburg Bridge	131	Dec/03/2002 09:53:31 AM	Dec/03/2002 10:00:19 AM	Dec/03/2002 10:30:28 AM
204	8/30/2009	Williamsburg Bridge	131	Aug/30/2009 03:59:46 PM	Aug/30/2009 04:05:20 PM	Aug/30/2009 04:35:52 PM
205	11/21/2005	Williamsburg Bridge	131	Nov/21/2005 08:15:16 AM	Nov/21/2005 08:20:08 AM	Nov/21/2005 08:44:03 AM
206	1/14/2006	Williamsburg Bridge	131	Jan/14/2006 12:21:46 PM	Jan/14/2006 12:28:22 PM	Jan/14/2006 01:05:50 PM
207	12/13/2004	Williamsburg Bridge	131	Dec/13/2004 08:18:48 AM	Dec/13/2004 08:26:02 AM	Dec/13/2004 09:10:51 AM
208	10/16/2014	Williamsburg Bridge	131	Oct/16/2014 02:19:22 PM	Oct/16/2014 02:22:04 PM	Oct/16/2014 03:01:39 PM
209	3/4/2004	Williamsburg Bridge	131	Mar/04/2004 05:31:23 PM	Mar/04/2004 05:35:52 PM	Mar/04/2004 06:04:04 PM
210	4/16/2003	Williamsburg Bridge	131	Apr/16/2003 09:25:03 AM	Apr/16/2003 09:34:29 AM	Apr/16/2003 10:17:45 AM
211	6/25/2006	Williamsburg Bridge	131	Jun/25/2006 02:15:50 AM	Jun/25/2006 02:21:12 AM	Jun/25/2006 02:48:11 AM
212	12/3/2018	Williamsburg Bridge	131	Dec/03/2018 07:31:55 PM	Dec/03/2018 07:36:50 PM	Dec/03/2018 08:03:02 PM

Case	Date	Bridge	NFIRS Type	Alarm Date	Arrival Date	Last Unit Clear Date
213	10/11/2003	Williamsburg Bridge	131	Oct/11/2003 06:32:28 PM	Oct/11/2003 06:39:14 PM	Oct/11/2003 07:13:06 PM
214	10/25/2014	Williamsburg Bridge	131	Oct/25/2014 11:42:46 AM	Oct/25/2014 11:48:43 AM	Oct/25/2014 12:21:21 PM
215	12/22/2006	Williamsburg Bridge	131	Dec/22/2006 11:45:29 PM	Dec/22/2006 11:50:38 PM	Dec/23/2006 12:20:09 AM

[END OF REPORT]